



2011-08-10

Flow-induced Responses of Normal, Bowed, and Augmented Synthetic Vocal Fold Models

Preston Roylance Murray
Brigham Young University - Provo

Follow this and additional works at: <https://scholarsarchive.byu.edu/etd>

 Part of the [Mechanical Engineering Commons](#)

BYU ScholarsArchive Citation

Murray, Preston Roylance, "Flow-induced Responses of Normal, Bowed, and Augmented Synthetic Vocal Fold Models" (2011). *All Theses and Dissertations*. 2873.

<https://scholarsarchive.byu.edu/etd/2873>

This Thesis is brought to you for free and open access by BYU ScholarsArchive. It has been accepted for inclusion in All Theses and Dissertations by an authorized administrator of BYU ScholarsArchive. For more information, please contact scholarsarchive@byu.edu, ellen_amatangelo@byu.edu.

Flow-Induced Responses of Normal, Bowed, and
Augmented Synthetic Vocal Fold Models

Preston R. Murray

A thesis submitted to the faculty of
Brigham Young University
in partial fulfillment of the requirements for the degree of
Master of Science

Scott L. Thomson, Chair
Anton E. Bowden
Steven E. Gorrell

Department of Mechanical Engineering

Brigham Young University

December 2011

Copyright © 2011 Preston R. Murray

All Rights Reserved

ABSTRACT

Flow-Induced Responses of Normal, Bowed, and Augmented Synthetic Vocal Fold Models

Preston R. Murray
Department of Mechanical Engineering, BYU
Master of Science

The voice is the primary mode of communication for humans. Because the voice is so important, voice disorders tend to severely diminish quality of life. A better understanding of the physics of voice production can help to improve treatment of voice disorders. For this thesis research a self-oscillating synthetic vocal fold model was developed, compared with previous synthetic vocal fold models, and used to explore the physical effects of augmentation injections on vibration dynamics. The research was conducted in two stages. First, four vocal fold models were evaluated by quantifying onset pressure, frequency, maximum glottal gap, flow rate, and medial surface motion. The newly developed model, differentiated from the other models by the inclusion of more layers, adjusted geometry, and an extremely soft superficial lamina propria layer, was included in this study. One of the models, created using MRI-derived geometry, had the most defined mucosal wave. The newly-developed model had the lowest onset pressure, flow rate, and smallest maximum glottal width, and the model motion compared very well with published excised human larynx data. Second, the new model was altered to simulate bowing by decreasing the volume of the body layer relative to that of a normal, unbowed model. Two models with varying degrees of bowing were created and tested while paired with normal models. Pre- and post-injection data (onset pressure, vibration frequency, glottal flow rate, open quotient, and high-speed image sequences) were recorded and compared. General pre- to post-injection trends included decreased onset pressure, glottal flow rate, and open quotient, and increased vibration frequency. Additionally, there was a decrease in mucosal wave velocity and an increase in phase angle. The thesis results are anticipated to aid in better understanding the physical effects of augmentation injections, with the ultimate goal of obtaining more consistent surgical outcomes, and also to contribute to the advancement of voice research through the development of the new synthetic model.

Keywords: vocal folds, vocal fold modeling, mucosal wave, high-speed imaging, injection laryngoplasty, larynx, medial surface, augmentation, Preston R. Murray

ACKNOWLEDGMENTS

I chose to pursue a degree in Mechanical Engineering at BYU-Idaho based on the suggestions of a good family friend. Although I was tentative about this decision at first, in short time I fell in love with the discipline and I have never looked back. Two years later, my wife and I felt we should transfer to BYU. The decision we made to follow the prompting has been the best decision in my life, second only to my decision to marry my wife. I will be forever grateful for the guidance I received and my irreplaceable experiences completing my undergraduate and graduate degrees at BYU.

I do not believe it is possible to have a more helpful or encouraging advisor. For the two years under his tutelage I have not only learned valuable lessons about the voice and the amazing gift that it is, but also about patience, having confidence that I can solve the problem at hand, and listening to promptings from the spirit. I regard my association with Dr. Thomson to be one of the richest blessings I have received during my time at BYU.

The Department of Mechanical Engineering and the National Institute on Deafness and Other Disorders deserve special thanks because without them none of this work could have been accomplished. They have provided the facilities, advisors, and monetary assistance necessary for me to do this work.

To my committee members, Dr. Anton Bowden and Dr. Steven Gorrell, I express my appreciation for reading through this thesis and providing valuable suggestions for improvement.

I would like to thank the members of the Vocal Fold Research Lab for their insightful suggestions and assistance in teaching me how to create synthetic vocal fold models and take meaningful data.

Finally, I would like to thank my beautiful wife Hillary and my son Jordan for their encouragement and patience as I have worked to overcome stumbling blocks in my research. Without their encouragement and support this thesis would not have been possible.

TABLE OF CONTENTS

LIST OF TABLES v

LIST OF FIGURES vii

1 Introduction..... 1

1.1 Anatomy of the Larynx..... 1

1.2 Vocal Fold Research..... 4

1.2.1 In Vivo and Excised Vocal Folds 5

1.2.2 Computational Vocal Fold Models..... 5

1.2.3 Synthetic Vocal Fold Models..... 6

1.3 Thesis Overview 8

1.4 Thesis Outline..... 9

1.4.1 Medial Surface Tracking and Dynamic Characteristic of Synthetic, Self-Oscillating Vocal Fold Models (Chapter 2)..... 9

1.4.2 Effect of Augmentation Injection on Bowed Self-Oscillating Synthetic Vocal Fold Models (Chapter 3)..... 10

2 Medial Surface Tracking and Dynamic Characteristics of Synthetic, Self-Oscillating Vocal Fold Models..... 11

2.1 Introduction..... 11

2.2 Methods 17

2.2.1 Self-Oscillating Synthetic Models 17

2.3 Experimental Setup and Procedure..... 22

2.3.1 Cross Correlation 25

2.3.2 Cross Correlation Algorithm..... 27

2.3.3 Phase Delay and Wave Velocity..... 29

2.3.4 Experimental Procedure..... 29

2.4 Results and Discussion 30

2.4.1	Onset Pressure.....	30
2.4.2	Vibration Frequency	30
2.4.3	Maximum Glottal Gap	31
2.4.4	Glottal Flow Rate	32
2.4.5	Superior Surface Imaging	33
2.4.6	Medial Surface Tracking.....	36
2.5	Conclusion	40
3	Effect of Augmentation Injection on Bowed Self-Oscillating Synthetic Vocal Fold Models	41
3.1	Introduction.....	41
3.2	Methods	44
3.2.1	Synthetic Model	44
3.2.1.1	Material Properties	46
3.2.1.2	Injections.....	48
3.2.2	Experimental Setup.....	49
3.2.2.1	Full Larynx Configuration	49
3.2.2.2	Hemilarynx Configuration	51
3.2.3	Experimental Procedure.....	52
3.3	Results and Discussion	55
3.3.1	Vibration Frequency	56
3.3.2	Glottal Flow Rate	57
3.3.3	Open Quotient.....	58
3.3.4	Superior Surface Imaging	59
3.3.5	Medial Surface Tracking.....	60
3.4	Conclusions.....	62
4	Conclusion	65

4.1	Medial Surface Tracking and Dynamic Characteristic of Synthetic, Self-Oscillating Vocal Fold Models (Chapter 2)	65
4.1.1	Conclusions	65
4.1.2	Future Work	66
4.2	Effect of Augmentation Injection on Bowed Self-Oscillating Synthetic Vocal Fold Models (Chapter 3)	66
4.2.1	Conclusions	66
4.2.2	Future Work	67
Appendix A. Model Fabrication		73
A.1)	Mold Fabrication and Preparation	75
A.2)	Casting of Each Layer	76
A.3)	Final Model Preparation for Testing	78
A.4)	Representative Results	79
A.5)	Discussion	81
A.6)	References	82
Appendix B. Image Calibration		85
Appendix C Uncertainty Analysis		89
C.1	Open Quotient	89
C.2	Subglottal Pressure	90
C.3	Onset Pressure	91
C.4	Glottal Flow Rate	92
C.5	Acoustic Frequency	92
C.6	Glottal Area	92
C.7	Trajectories	94
Appendix D. Matlab		97
D.1	Position Tracking of Points in 3D Space Over Time	98

D.2 Code to Extract Maximum Glottal Width.....	112
Appendix E. Drawings.....	115

LIST OF TABLES

Table 1-1: Human vocal fold geometry	4
Table 2-1: Values for the geometric parameters used in the M5-UNI, M5-CONV	14
Table 2-2: Young's modulus values measured for various silicone mixture ratios; EF = Ecoflex®, DS = Dragon Skin®. For example, 1:1:4 denotes a mixture of one part	20
Table 2-3: Uncertainty estimate in each measurement.	30
Table 2-4: Mean and standard deviation (in parentheses) of onset pressures for the	30
Table 2-5: The computed maximum values of point displacement and velocity.	39
Table 2-6: Mucosal wave velocities for all models. All models were vibrated at 120% of Pon..	39
Table 3-1: Geometric parameters and description used to define model.....	45
Table 3-2: Young's modulus for each layer of the synthetic model.	47
Table 3-3: Uncertainty estimate in each measurement.	53
Table 3-4: Average injection amounts for both symmetric and hemilarynx experiments.....	54
Table A-1: Geometric parameters and description used to define model.....	74
Table A-2: Mixture ratios by weight and resulting Young's modulus of the individual sections of the vocal fold model. EF and DS designate silicone made from Ecoflex®	74
Table A-3: Comparison between human and synthetic vocal fold vibratory responses.	79
Table A-4: Specific reagents and equipment	82
Table C-1: Maximum average error from mis-selecting pixels locations in hemilarynx images.	95

LIST OF FIGURES

Figure 1-1: Sagittal cross section of the vocal tract and larynx (adapted from Gray's Anatomy of the Human Body, images public domain, www.bartelby.com).....	2
Figure 1-2: Coronal cross section of the human larynx. Glottis, supraglottis, and subglottis (right) areas are denoted (adapted from Gray's Anatomy of the Human Body, images public domain, www.bartelby.com).....	3
Figure 1-3: Coronal cross section illustrating the various layers of human vocal folds.....	4
Figure 1-4: Four layer synthetic vocal fold model.....	9
Figure 2-1: Cross section of four self-oscillating synthetic vocal fold models. Clockwise from the upper left: M5-UNI, M5-CONV, EPI, MRI.	13
Figure 2-2: Geometric parameters for the models used in this study.	14
Figure 2-3: Schematic of four-layer model fabrication process, including cross sections of CAD models used for rapid prototyping, mold-making, and creation of the various layers. Shown at bottom is a finished model with all layers.....	19
Figure 2-4: Placement of the thread in the mold. (a) The mold for the ligament being cut by the razor. (b) Thread placed in the mold for model fabrication.....	20
Figure 2-5: Elastic (G') and viscous (G'') shear moduli.....	22
Figure 2-6: Full larynx experimental setup (not to scale).....	23
Figure 2-7: Hemilarynx experimental setup (not to scale).	24
Figure 2-8: Stereo image pair of the M5-CONV model used for medial surface tracking. Direction of air flow is from bottom to top of the images.	25
Figure 2-9: Dot selected for input into the cross correlation algorithm. Air flow is from low to high.	26
Figure 2-10: Subwindow of the point at time i and time $i + 1$	26
Figure 2-11: Correlation peak (left) and surface map (right) of the cross correlation.....	27
Figure 2-12: Stereo images of the selected dot on the medial surface of the synthetic vocal fold model.	28
Figure 2-13: Frequency response for the various models at 110%, 120% and 130% of their respective onset pressures. M5-UNI (\bullet), M5-CONV (\circ), MRI (\times), EPI without tension ($+$), and EPI with tension (\square).	31

Figure 2-14: Maximum glottal width of the models at 110%, 120% and 130% of their respective onset pressures. Symbols are the same as listed in Figure 2-13.	32
Figure 2-15: Flow rate of the models at 110%, 120% and 130% of their respective onset pressures. Symbols are the same as listed in Figure 2-13.	33
Figure 2-16: Superior view showing high-speed images from the five models. All images were obtained with the models vibrating at 120% of their respective onset pressures.	34
Figure 2-17: Process of extracting kymograms from high-speed images of the superior surface.	35
Figure 2-18: High-speed kymograms of one period for the four models. Estimated locations of the superior (green) and inferior (blue) margins shown by dotted lines.	36
Figure 2-19: Vocal fold model motion at six phases of oscillation. Axes denote position in mm. Flow is in the inferior (bottom) to superior (top) direction. The dashed line denotes the glottis midline (position of the clear acrylic plate). The elliptical lines show the position of the dots through one period of oscillation. The solid blue line is a spline interpolation between dots, illustrating the position of the medial surface at the given phase.	37
Figure 2-20: Velocity of each applied dot for all models. M5-UNI (•), M5-CONV (◦), MRI (×), EPI without tension (+), and EPI with tension (◻).	38
Figure 3-1: Parameters defining vocal fold geometry (left) and cross section of normal model developed in Chapter 2 (right).	43
Figure 3-2: Normal model compared with the 10% (middle) and 20% (right) bowed models, respectively. Flow is from bottom to top. (Epithelium and fiber not shown).....	45
Figure 3-3: Superior view of normal (left) and bowed (right) vocal fold models showing bowing definition. Flow direction is out of the page. Epithelium and fiber are not shown.	46
Figure 3-4: Elastic shear modulus (G' , left) and viscous shear modulus (G'' , right) for the four layers used in the models. Error bars show one standard deviation.	48
Figure 3-5: Mounting plate with holes for injecting material laterally in the bowed models. Flow direction is from inferior to superior.	48
Figure 3-6: Rheological comparison of the elastic (left) and viscous (right) shear moduli of the injected material with two common bio injections. ●, ■, and ◆ are the injected material, Cymetra, and Radiesse materials (the latter from Caton et al., 2007).	49
Figure 3-7: Full larynx experimental configuration (not to scale).	50
Figure 3-8: Hemilarynx experimental configuration (not to scale).	51

Figure 3-9: Right view of the medial and inferior surfaces of the synthetic vocal fold model. Applied dots were for point tracking purposes. Columns are labeled from left to right as C1-C5; rows are labeled from top to bottom as R1-R5.	52
Figure 3-10: Superior view of normal (left) and bowed (right) paired models pre-injection (left image) and post-injection (right image). Dark circles are injections.	54
Figure 3-11: Pre- and post-injection onset pressures for the 10% (left section, ◆ markers) and 20% (right section, ■ markers) bowing cases. Solid, dashed, and dotted lines are experiments one, two, and three respectively. Left and right markers in each column are pre- and post-injection data, respectively. Error bars designate one standard deviation.	56
Figure 3-12: Pre- and post-injection vibration frequencies for the 10% (left section, ◆ markers) and 20% (right section, ■ markers) bowing cases. Solid, dashed, and dotted lines are experiments one, two, and three respectively. Left and right markers in each column are pre- and post-injection data, respectively.....	57
Figure 3-13: Pre- and post-injection flow rates for the 10% (left section, ◆ markers) and 20% (right section, ■ markers) bowing cases. Solid, dashed, and dotted lines are experiments one, two, and three respectively. Left and right markers in each column are pre- and post-injection data, respectively.....	58
Figure 3-14: Pre- and post-injection open quotients for the 10% (left section, ◆ markers) and 20% (right section, ■ markers) bowing cases. Solid, dashed, and dotted lines are experiments one, two, and three respectively. Left and right markers in each column are pre- and post-injection data, respectively.	59
Figure 3-15: Timeline of one cycle of oscillation pre- and post-injection. Model is the 20% bowed, excess injection case.....	60
Figure 3-16: Pre- (top) and post- (bottom) injection trajectories of the points in column C3 through one period of vibration. The dotted line represents the location of the clear acrylic plate. Flow is from bottom to top. The sub-figure shows the uncertainty associated with point selection determination. Units are mm.....	61
Figure 3-17: Pre- and post-injection wave velocities (solid lines) and phase delay per mm (dashed lines) of column three (C3) for the 10% (left section, ◆ markers) and 20% (right right, ■ markers) bowing cases. Left and right markers in each column are pre- and post-injection data, respectively.....	62
Figure A-1: Synthetic vocal fold model fabrication process. CAD-derived solid models (left panel) are used to create molds (center panel) for each layer. Each layer is then cast, beginning with the body layer and ending with the epithelium layer (right panel, with each layer “peeled back” for visibility). After fabrication, models are mounted to acrylic plates for testing.....	73
Figure A-2: Synthetic vocal fold model cross section. Distinct body, superficial lamina propria, ligament, and epithelium layers are shown. Parameters define vocal fold model	

geometry. This figure is scaled for clear representation of geometric definitions. Application of the parameter values given in Table A-1 will result in a slightly different shape than what is shown here.	74
Figure A-3: High-speed kymogram of model vibration. Estimates for the location of the superior and inferior margins are shown in colored dotted lines. Phase differences between the inferior and superior margins are evident.	80
Figure A-4: Medial surface profile of synthetic vocal fold model in a hemilarynx arrangement, captured at two different instances of time while vibrating. Ink markers were placed on the medial surface (as shown in the right image), imaged using two synchronized high-speed cameras, and tracked over the vibratory cycle. The left plot shows a convergent glottis during the opening phase and the right plot shows a divergent glottis during the closing phase.	80
Figure B-1: Pair of typical stereo images of the medial and inferior surfaces of a synthetic vocal fold model.	85
Figure B-2: Planar calibration plates placed at the surface of the clear acrylic plate for calibrating the images.	86
Figure B-3: Planar calibration plates with unnecessary pixels set to zero.	86
Figure B-4: Thresholded images after they were converted to binary.	87
Figure B-5: Final image showing the found dot locations plotted over the original image.	87
Figure C-1: Uncertainty analysis locations in the left and right hemilarynx images. The upper and lower left, middle, and right locations of the analysis are shown as white dots.	95
Figure E-1: Isometric view of acrylic plate with injection holes.	116
Figure E-2: Acrylic vocal fold model holder with holes for injecting bowed model.	117
Figure E-3: Hemilarynx assembly during the calibration process.	118
Figure E-4: Hemilarynx setup for mounting of vocal fold model acrylic holder.	119
Figure E-5: Acrylic vocal fold support.	120
Figure E-6: Calibration plate mount.	121
Figure E-7: Transparent plate.	122
Figure E-8: Base plate for hemilarynx setup.	123
Figure E-9: Transparent plate support.	124

1 INTRODUCTION

The voice is the primary mode of communication for humans. Because the voice is so important, voice disorders tend to severely diminish quality of life. The National Institute on Deafness and Communication Disorders (NIDCD) reports that approximately 7.5 million people are affected by voice disorders in the United States alone (NIDCD, 2010). Clinical treatment of many voice disorders is relatively effective, but is limited by the understanding of the physics that govern the voice and voice production. A better understanding of voice production mechanisms has the potential to benefit the clinical prevention, diagnosis, and treatment of voice disorders. The purpose of this thesis research is to contribute to an increased understanding of the voice by (1) developing a synthetic vocal fold model that exhibits a flow-induced vibratory response that is similar to that of the human vocal folds, and (2) using the model to explore the effect of lateral augmentation (a surgical procedure used to alleviate vocal fold bowing) on vocal fold vibration.

1.1 Anatomy of the Larynx

Sound for voiced speech originates in the larynx. The larynx is found in the front of the neck as illustrated in Figure 1-1. The vocal folds are located around the center of the larynx, are approximately horizontal, and run in the anterior-posterior direction. The area between the vocal

folds is called the glottis, the region above is called the supraglottis, and the region below is the subglottis (see Figure 1-2).

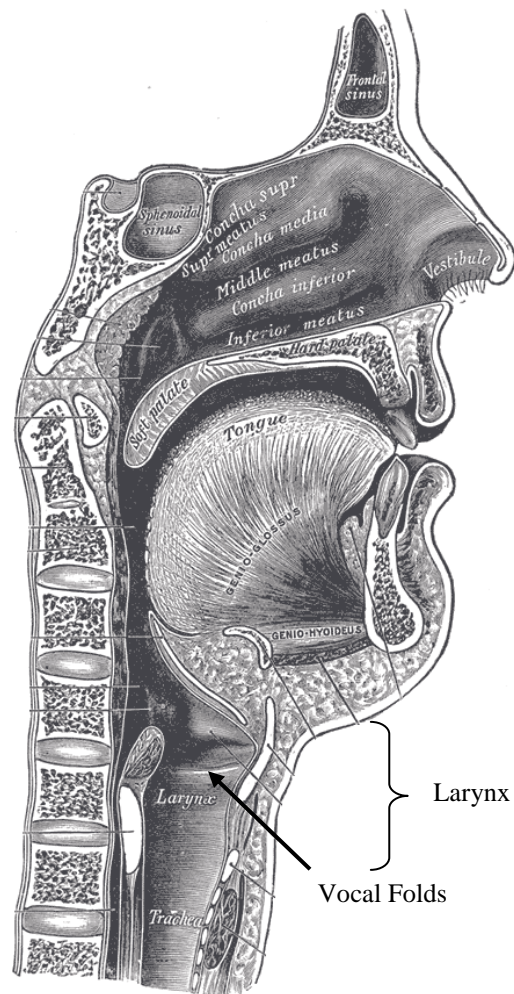


Figure 1-1: Sagittal cross section of the vocal tract and larynx (adapted from Gray's *Anatomy of the Human Body*, images public domain, www.bartelby.com)

The vocal folds play a central role in producing sound for voicing (phonation). During phonation, the vocal folds are brought together by laryngeal muscles. The diaphragm compresses the lungs to induce laryngeal airflow; this creates a transglottal pressure gradient. The high pressure in the lungs forces the vocal folds apart, and the air flow velocity within the vocal folds increases. The vocal folds are then brought back together due to elastic restoring forces within

the vocal folds as well as lower glottal pressure that accompanies the increased velocity (the Bernoulli effect). This process repeats on the order of hundreds of times per second.

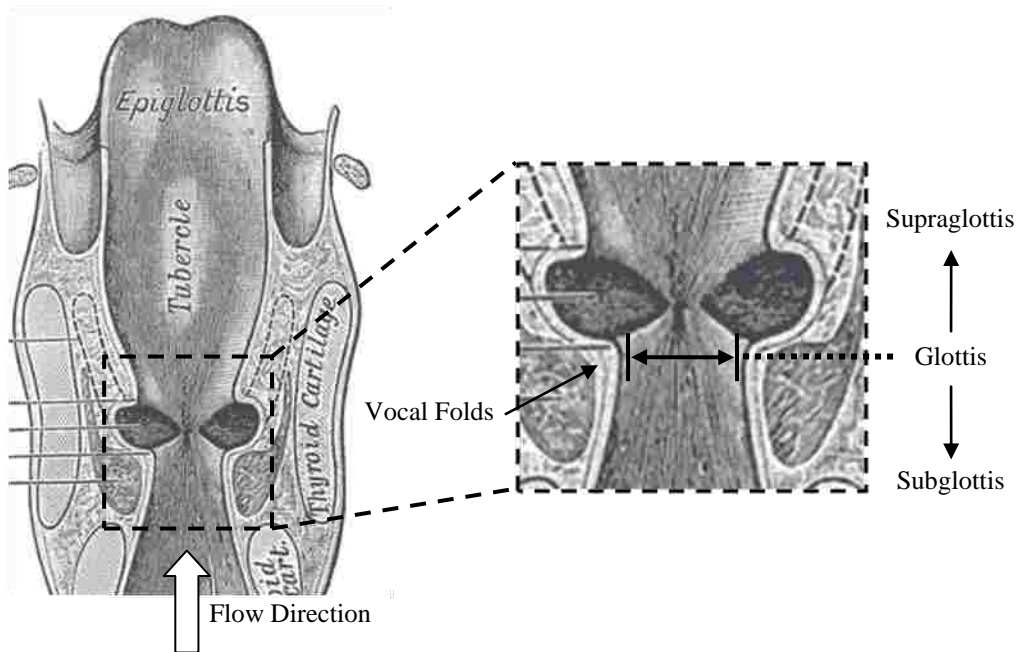


Figure 1-2: Coronal cross section of the human larynx. Glottis, supraglottis, and subglottis (right) areas are denoted (adapted from Gray's *Anatomy of the Human Body*, images public domain, www.bartelby.com)

The vocal folds are comprised of multiple layers of tissue, each having different mechanical properties, and consist of epithelium, lamina propria (with separate superficial, intermediate, and deep layers), and muscle layers (Hirano and Kakita, 1985) (see Figure 1-3). These layers are generally grouped into cover (epithelium and superficial lamina propria), ligament (intermediate and deep lamina propria), and body (muscle) layers (Hirano and Kakita, 1985).

Each layer is here briefly described and summarized in Table 1-1 (also see Figure 1-3). The epithelium is the outermost layer of the vocal fold and is made of stratified squamous cells. It is extremely thin and is thought to have a high modulus of elasticity. It acts as a “capsule” (Hirano and Kakita, 1985) for the vibrating vocal fold. The superficial lamina propria is very soft

with the approximate consistency of gelatin. The intermediate and deep layers are composed of differing amounts of elastin and collagen fibers: moving from the outer part of the intermediate layer to the inner part of the deep layer generally coincides with a transition from more elastin to more collagen fibers. This gives the tissue the elastic and viscous properties necessary for tissue oscillation (Gray et al., 1999).

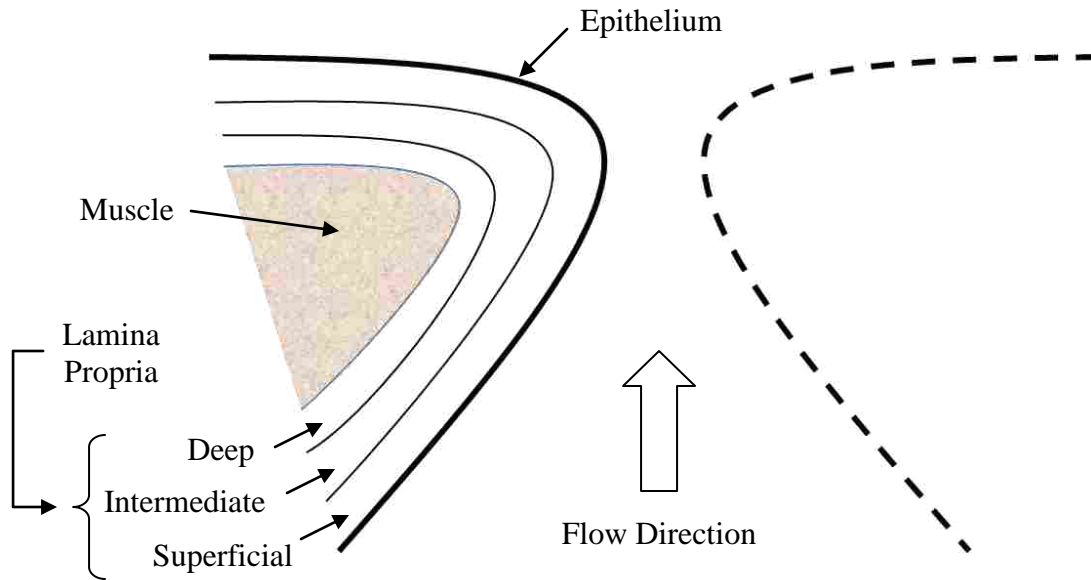


Figure 1-3: Coronal cross section illustrating the various layers of human vocal folds

Table 1-1: Human vocal fold geometry

Layer	Typical Thickness	Tissue Type	
Epithelium	50 μm	Stratified squamous cell	
Lamina propria	Superficial	250 μm	Thin, loose, collagen fibrils
	Intermediate	400 μm	Non-straight, bundles of elastic fibers
	Deep	400 μm	Densely crowded, spiraling collagen fibers
Muscle	7.3 mm	Muscle fibers	

1.2 Vocal Fold Research

Characterization of voice production has been the topic of numerous research studies. Parameters that have been studied include pressure-flow relationships, vocal fold tissue dynamics, airway surface liquid behavior, glottal jet dynamics, radiated sound production, and

rheological properties. In these types of studies, researchers have used vocal folds and/or vocal fold models that fall into one of three categories, 1) real (in vivo or excised), 2) computational, and 3) synthetic. In order to provide background and context for the present research, advantages and disadvantages of these three methods are briefly discussed below. More in-depth literature surveys are given in Chapters 2 and 3.

1.2.1 In Vivo and Excised Vocal Folds

Experiments with in vivo human vocal folds are the most physiologically realistic, but observations of vocal fold vibration can typically only be made from a superior view of the vocal folds (e.g., using a laryngoscope). Because of limited access and potential hazards, these studies are limited in scope. Excised larynx studies have the advantage of being relatively representative physiologically, but living conditions cannot be completely simulated (e.g., no vascular or neurological influences are present). In addition, even with careful treatment (such as using humidified air), the useable time frame of excised larynges is limited to around a few minutes of vibration because of tissue degradation. Animal (e.g., canine, porcine) larynges are often used because of their similarities to human vocal folds. In general, excised larynx studies are very useful for studying voice production and mechanics, but cannot be used for extended periods of time and are limited in being able to perform parametric studies involving tissue and geometric properties.

1.2.2 Computational Vocal Fold Models

Computational vocal fold models have also been used to study voice production. With this approach many factors can be parameterized and important features (e.g. pressure distributions, flow rates) that are difficult to measure experimentally can be easily obtained.

Geometric and material properties of these models have typically been idealized. Major limitations of these models include long computation time as well as both difficulty and uncertainty in incorporating complex physical phenomena such as acoustic effects, turbulence, flow separation, and accurately resolving the associated time-varying, large-scale, three-dimensional flow patterns (Decker and Thomson, 2005).

1.2.3 Synthetic Vocal Fold Models

Synthetic models have been increasingly used in recent years to study vocal fold vibration. They can be divided into three main categories: static, driven, and self-oscillating. The method used primarily depends on what information is desired

Static Models

Static vocal fold models incorporate similar geometry to that of true vocal folds (but usually idealized), but there is no motion. This method allows for investigation of correlations between variables such as flow rates, transglottal pressures, and glottal geometry. Symmetric, asymmetric, and hemilarynx (single vocal fold) models have been used. For example, Fulcher et al. (2006) used static models to determine flow rate as a function of symmetric glottal geometry and transglottal pressure. They later performed a similar experiment using a hemilarynx configuration (Fulcher et al., 2010). One advantage of static models is that they can be easily scaled up to enable more convenient measurements. Erath and Plesniak (2006a, 2006b) used this advantage to study the bimodal jet trajectory of the air passing through symmetric and asymmetric static vocal fold models. In another study, vortical structures were investigated as the induced air passed through a static model of the vocal folds and false vocal folds (Chisari et al.,

2010). Inherent to static model investigations is the limitation that fluid-structure interactions associated with structural motion are not able to be investigated.

Driven Models

Driven synthetic vocal fold models are those in which an externally-applied, usually periodic, movement of the vocal fold model is prescribed. The motion can be of the form of a linear, uniform oscillation (such as that which is obtained using an electrodynamic linear actuator) (e.g., Deverge et al., 2003) or a motion with more complex waveform generated by a rotating cam as demonstrated by Triep et al. (2005). These models are sometimes life-sized and tested in air (e.g., Mongeau et al., 1997) or scaled up and tested in water (e.g., Krane et al., 2007). The advantage of driven models is that periodic motion is obtained; however, the motion is not in response to the airflow (as is the case with human vocal folds).

Self-Oscillating Models

In order to simulate the fully-coupled fluid-structure-acoustic interactions that are present in human phonation, a model must self-oscillate in a manner similar to the human vocal folds. To this end, self-oscillating synthetic models have been created which approximate the vibration characteristics of true vocal folds. Membranous models which approximated the cover and superficial layer of the lamina propria were developed by Titze et al. (1995) and Chan et al. (1997, 2006) and used to study the effects of viscosity, epithelium thickness, and intraglottal angle on vocal fold vibration. The major limitations of these models were that only two layers were approximated and that the geometry was highly idealized.

Thomson et al. (2005) created a homogeneous, life-size, self-oscillating model. This model's geometry was based on simplified human subject-derived geometric definitions given by Scherer et al. (2001). In later work this model was extended to include two separate body and

cover layers, each with unique material properties (Riede et al., 2008). This two-layer model concept has since been used to study supraglottal vortices (Neubauer et al., 2007), quantify the impact stresses as vocal folds collide (Spencer et al., 2008), develop in vivo measurement devices (Popolo and Titze, 2008), investigate flow structure interactions (Becker et al., 2009), and evaluate the effect of material asymmetries (Pickup and Thomson, 2009). Advantages of this model include relative ease of fabrication, repeatability, and ability for parametric studies involving material and geometric properties. Disadvantages include idealized geometry, isotropic material properties, high onset pressure (the pressure required to initiate vibration), and some less-than-life-like motion (these disadvantages are discussed further in Chapter 2).

1.3 Thesis Overview

The purpose of this work was two-fold: (1) to create and characterize an improved synthetic vocal fold model that more closely approximates human vocal fold motion, and (2) to characterize the effect of augmentation injections on the vibratory response of the new synthetic model. The model included four layers to approximate the epithelium, lamina propria, ligament, and body layers of human vocal fold, as well as an acrylic fiber in the center of the ligament layer to introduce anisotropy (see Figure 1-4).

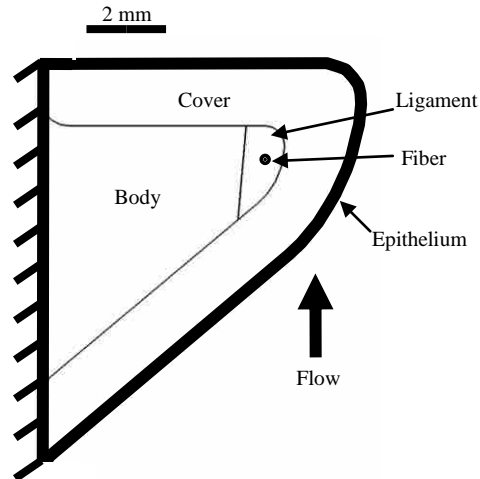


Figure 1-4: Four layer synthetic vocal fold model

1.4 Thesis Outline

This thesis is divided into two parts:

- 1) Characterization and comparison of self-oscillating synthetic models, including the new model developed as a part of this thesis research.
- 2) Quantification of augmentation injections on synthetic model vibration.

1.4.1 Medial Surface Tracking and Dynamic Characteristic of Synthetic, Self-Oscillating Vocal Fold Models (Chapter 2)

Four self-oscillating vocal fold models were evaluated by quantifying onset pressure (a measure of vocal effort), vibration frequency, maximum glottal gap experienced during vibration, flow rate, and medial surface motion. A new model was included in the study that incorporated more layers, altered geometry, and an extremely soft superficial lamina propria layer. The data show that the model exhibits significant improvements over previous synthetic models. Limitations of the new model are discussed and suggestions for future related studies are presented.

1.4.2 Effect of Augmentation Injection on Bowed Self-Oscillating Synthetic Vocal Fold Models (Chapter 3)

The new vocal fold model was modified to simulate bowing by decreasing the volume of the body layer relative to that of a normal, unbowed model. Material properties and relative geometries of the other layers were unchanged. Two models with varying degrees of bowing were created and tested while paired with normal models. Following initial acquisition of data (onset pressure, vibration frequency, glottal flow rate, sound intensity, and high-speed image sequences), the bowed models were augmented with silicone possessing similar material properties to those used in augmentation procedures. Three different silicone injection quantities were tested: sufficient to close the glottal gap, insufficient to close the glottal gap, and excess silicone to create convex bowing of the bowed model. The above-mentioned metrics were again taken and compared. Pre- and post-injection high-speed imaging data were also acquired using a hemilarynx setup, from which medial surface dynamics were quantified. The pre- and post-injection data were used to assess the influence of the augmentation injections on the model's vibratory response.

2 MEDIAL SURFACE TRACKING AND DYNAMIC CHARACTERISTICS OF SYNTHETIC, SELF-OSCILLATING VOCAL FOLD MODELS

Four vocal fold models were evaluated by quantifying onset pressure (a measure of vocal effort), frequency, maximum glottal gap, flow rate and medial surface motion. A new model was included in the study that incorporated more layers, different geometry, and an extremely soft superficial lamina propria layer. All models were fabricated from a flexible silicone compound with Young's modulus values similar to those found in human vocal folds. Each model was mounted in a full larynx configuration and onset pressure (pressure at which vibration begins), vibration frequency, glottal width (distance from one edge of a vocal fold to the other), and glottal flow rate. A hemilarynx configuration was also used to compare medial surface dynamics. Limitations of the new model are discussed and suggestions for future related studies are presented.

2.1 Introduction

Synthetic, self-oscillating vocal fold models have been useful subjects in various aspects of voice research, including measuring vocal fold collision forces (Spencer et al., 2008), characterizing supraglottal vortices (Neubauer et al., 2007), and developing in vivo measurement devices (Popolo and Titze, 2008). Synthetic vocal fold models are beneficial because their geometries and material properties can be parametrically varied using a repeatable fabrication process and they are usable for longer durations than excised larynges.

A comprehensive summary of synthetic vocal fold models can be found in Kniesburges et al. (2011), but two self-oscillating types are discussed here. The first is the “membranous-type” of Titze et al. (1995), in which a thin layer of silicone was placed over a hexagonal rod and fluids of varying viscosity were injected between the silicone membrane and the rod surface. This model thus approximated the epithelium and superficial lamina propria (SLP) layer. This model was used, in part, to validate the theory (Titze, 1988) that the SLP fluid viscosity had a large effect on onset pressure. Chan et al. (1997) and Chan and Titze (2006) extended the use of this model by varying the silicone thickness, changing the glottal convergence angle, and using injected viscoelastic biomaterials. The models were used to examine changes in onset pressure due to changes in epithelial membrane thickness, pre-vibratory glottal half-width, mucosa viscosity, and glottal divergence angle.

The other type of self-oscillating vocal fold model is that which is created by casting flexible rubber models in molds of the desired geometry. Both single-layer (homogeneous) and two-layer models have been developed and used. Thomson et al. (2005) created a single-layer model of this type with a modulus of elasticity of 13.7 kPa (which is comparable to that of vocal fold tissue) and a shape based on the “M5” geometry of Scherer et al. (2001). This model was of the same size scale as the human vocal folds (anterior-posterior dimension of 17 mm), had an onset pressure of 1.2 kPa (compared to around 0.29 to 0.49 kPa for human phonation, Baken and Orlikoff, 2000), and vibrated at a frequency of 120 Hz (close to that of an adult human male, Baken and Orlikoff, 2000). This same type of model was subsequently used in other studies (Spencer et al., 2008; Neubauer et al., 2007; Popolo and Titze, 2008). Motivated by the cover-body theory of vocal fold vibration (e.g., Hirano and Kakita, 1985), similar two-layer models have been fabricated (Drechsel and Thomson, 2008; Riede et al., 2008; Pickup and Thomson,

2009). Advantages of this model concept include ease of geometric and material property parameterization, durability, and relatively good agreement with human vocal fold vibration in terms of frequency and vibration amplitude. Disadvantages have included high onset pressure and less-than-lifelike motion, the latter including prominent inferior-superior displacement, minimal alternating convergent/divergent profile, and limited or no mucosal wave. These disadvantages have generally been attributed to geometric and material simplifications (i.e., idealized geometry, isotropic materials, and only two layers). A cross section of the two-layer model concept is shown in Figure 2-1, in which one MRI-derived model (discussed below) and three M5-derived models are shown. M5-related geometric parameter definitions are listed in Table 2-1 as per the key in Figure 2-2. The acronyms in the caption of Figure 2-1 are described below.

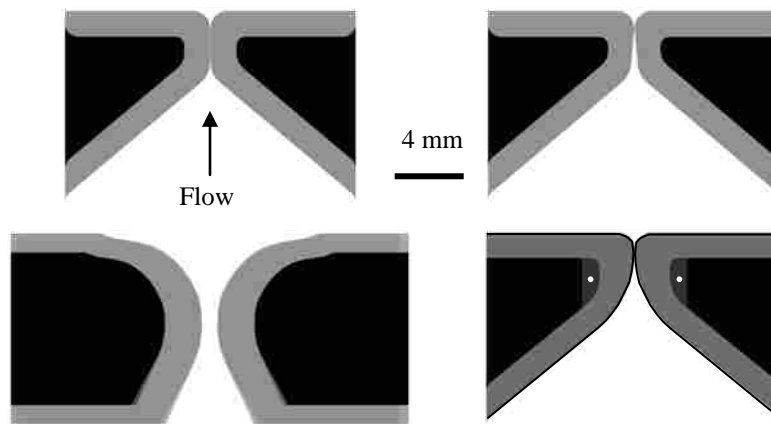


Figure 2-1: Cross section of four self-oscillating synthetic vocal fold models. Clockwise from the upper left: M5-UNI, M5-CONV, EPI, MRI.

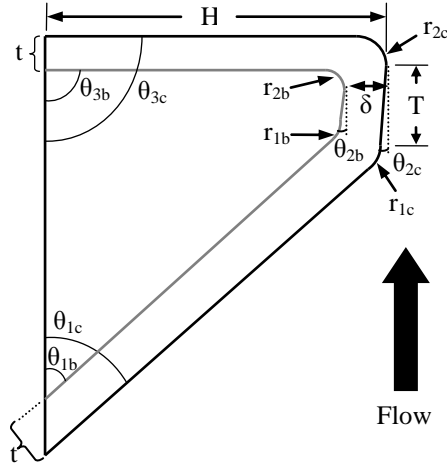


Figure 2-2: Geometric parameters for the models used in this study.

Table 2-1: Values for the geometric parameters used in the M5-UNI, M5-CONV and EPI models based on the parameters defined in Figure 2-2

Parameter	M5-UNI	M5-CONV	EPI
$\theta_{1b,c}$	50°	50°	50°
$\theta_{2b,c}$	0°	5°	5°
$\theta_{3b,c}$	90°	90°	90°
r_{1c}	1.5 mm	1.5 mm	6.0 mm
r_{2c}	0.987 mm	0.987 mm	0.987 mm
r_{1b}	1.12 mm	1.12 mm	2.0 mm
r_{2b}	0.513 mm	0.513 mm	0.513 mm
T	2 mm	2 mm	0.1 mm
t	1.15 mm	1.5 mm	1.5 mm
δ	1.15 mm	1.5 mm	2.0 mm
D	8.4 mm	8.4 mm	8.4 mm

Pickup and Thomson (2010) tested a two-layer synthetic model using geometry from magnetic resonance imaging (MRI) data of the larynx, a cross section of which is shown in Figure 2-1. Compared to a two-layer M5 model that had the same material properties as the MRI model, it was reported that the MRI model appeared to vibrate with less vertical displacement and showed evidence of a convergent/divergent profile and a mucosal wave, although no data was provided to quantify these observations. However, the model's onset pressure was

significantly higher (1.86 kPa) than that of the two-layer M5 model (0.91 kPa) and also displayed some anterior-posterior asymmetric motion.

Motivated by the improved motion of the MRI model, which had the same material properties as M5 model but vibrated quite differently, Pickup and Thomson (2011) used finite element analysis to determine which geometric features played a significant role in governing the M5 model motion. The geometric features shown in Figure 2-2 were varied. The primary geometries that most affected parameters such as maximum glottal width, alternating convergent/divergent motion, and mucosal-wave-like motion, were identified. It was suggested that improved model motion could be achieved by adopting a convergent pre-phonatory profile (θ_{2c}) and enlarging the entrance radius (r_{1c}).

To summarize, the membranous-model concept of Titze et al. (1995) has a flexible cover (as is the case with the human vocal folds), but precise control over initial geometry is not feasible. The one- and two-layer models have more control over initial geometry, thereby potentially allowing for a wider range of parametric studies. They represent some aspects of human phonation well, but limitations include lack of mucosal-wave-like motion (as in the M5 models), high onset pressure and anterior-posterior asymmetric motion (as in the MRI model), and the use of isotropic materials (both M5 and MRI models).

Multiple studies to quantify medial surface dynamics of canine and human excised larynges have been helpful in developing an understanding of the important role of the medial surface motion in vocal fold vibration (e.g., Berry et al., 2001; Doellinger et al., 2005, 2006a, 2006b; Boessenecker et al., 2007). These studies incorporated a hemilarynx setup that enabled the imaging of micro-sutures sewn into the medial surface. The micro-sutures were tracked and

their three dimensional trajectories calculated. These studies have provided important information regarding the building blocks of self-sustained vocal fold vibration.

Because of the known significance of the role of medial surface dynamics on vocal fold vibration and the growing use of synthetic models mimicking human vocal fold motion, it is important that synthetic vocal fold model medial surface motion be compared with that of excised vocal folds. Some other aspects of model motion have been reported; for example, Berry et al. (2006) used a single-layer M5 model in a hemilarynx experiment and the method of empirical eigenfunctions to study mechanisms of irregular vibration in sub-harmonic phonation and bi-phonation. Spencer et al. (2008), also using a single-layer M5 model, measured strains and stresses on the superior surface using stereo high-speed imaging to predict contact stresses. High-speed superior surface imaging and videokymographic approaches have also been used with synthetic models (Drechsel and Thomson, 2008; Pickup and Thomson, 2009, 2010). However, lacking are direct measurements of synthetic model medial surface motion (e.g., trajectories of points on the medial surface). The acquisition of this data will allow for quantitative comparison of synthetic model medial surface vibratory motion with the above-mentioned excised larynx medial surface studies.

The purposes of this chapter are twofold. The first is to introduce a synthetic model that includes the advantages of previous synthetic models (repeatability, control over geometry) but that also overcomes previous limitations; i.e., it has low onset pressure, reduced inferior-superior vertical motion, and a mucosal wave. The model includes a cover that is composed of a thin epithelial layer on top of a very flexible material, a ligament layer that includes an anteriorly-posteriorly-oriented fiber that restricts vertical motion, and a body layer. The second purpose is to quantify medial surface motion of several synthetic, self-oscillating vocal fold models. Models

studied include those shown in Figure 2-1; a two-layer model of the original M5 geometry, a modified M5 model based on the computational results of Pickup and Thomson (2011), the MRI model of Pickup and Thomson (2010), and the new model described herein. Other measures such as onset pressure, frequency, and maximum glottal gap are also reported. The results are compared with previous experiments on excised human vocal folds.

2.2 Methods

2.2.1 Self-Oscillating Synthetic Models

Four different synthetic models were used in this study (see Figure 2-1): a two-layer model with M5 geometry and uniform glottal profile (i.e., no convergent or divergent angle; here denoted as the “M5-UNI” model), a two-layer model with M5 geometry and a 5° convergent glottal profile (“M5-CONV”), a two-layer model with geometry derived from MRI data (“MRI”), and the new multi-layer model (“EPI”). The EPI model was based on the M5 geometry but used some substantially different values of some dimensions (see Table 2-1). It also included a very flexible superficial lamina propria layer that was covered by a thin epithelial layer, and an anterior-posterior running thread through the ligament layer. The location of the thread is due to the importance of the large longitudinal tensions of the collagen fibers in the ligament layer important to sustained phonation of human vocal folds (Titze, 2000). Material properties of each layer of each model were tested. Design, fabrication, and tested material properties for each of these models are described below.

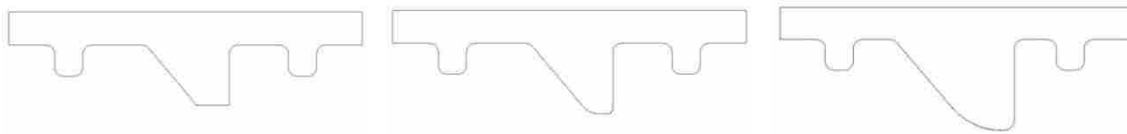
Two-layer vocal fold models have cover layers that are more flexible than body layers. However, the cover layer stiffness is limited by the need for the cover to withstand the periodic impact and large-amplitude motion that occurs during vibration. The EPI model was designed to

overcome this limitation by creating an extremely soft superficial lamina propria layer and covering this layer with a thin epithelium layer (similar to the membrane-superficial lamina propria concept of Titze et al., 1995). A ligament section acted as a gradient (in terms of stiffness) between the soft cover and a stiff body. An acrylic fiber was placed through the center of the ligament which could be tensioned. This introduced anisotropy and helped reduce inferior-superior model motion. The model geometric parameters generally followed the suggestions of Pickup et al. (2011) to incorporate a pre-phonatory convergent profile ($\theta_{1b,c}$) and large entrance radius ($r_{1b,c}$).

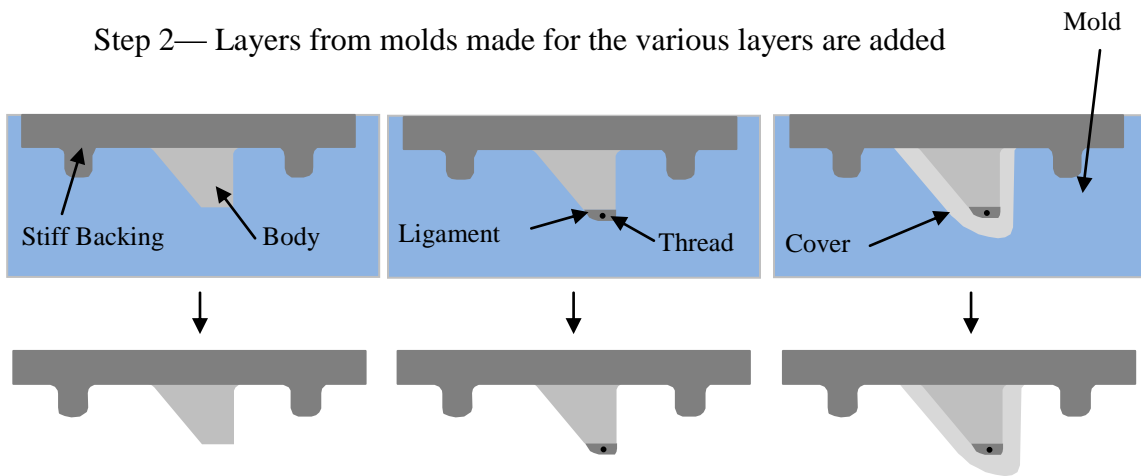
The models were made using addition-cure silicone rubber. The basic steps for fabricating the models are given here; note that details of the two-layer fabrication process can be found by referring to previous studies (e.g., Thomson, 2004; Thomson et al., 2005; Reide et al., 2008; Pickup and Thomson, 2010), and the new EPI model fabrication process is detailed in Appendix A and in Murray and Thomson (in press). Computer solid models of each layer were made using Pro/Engineer, from which rapid prototype models were created (illustrated in Figure 2-3 for the EPI model). Molds were created with these rapid-prototyped models using Smooth-Sil 950 mold-making compound (this and all other materials listed here are manufactured by Smooth-On, Inc.) Liquid two-part silicone (EcoFlex[®]) and Silicone Thinner were mixed according to the desired ratio, degassed, poured into the mold cavity, and cured in an oven at 250 °F for one hour. The process was repeated for each additional layer. For fiber placement in the ligament layer of the EPI model, the mold was cut in the anterior-posterior direction in the center of the medial surface with a straight razor (Figure 2-4). Before the silicone was poured into this section, the acrylic fiber was inserted into the cut with approximately 10 cm of excess fiber on either side of the mold for tensioning. After the models were made and the support material

removed, another type of three-part silicone mixture (Dragon Skin[®]) was poured over the model and allowed to cure. The last step was repeated to give two layers of durable silicone on the exterior of the model.

Step 1— Rapid-prototype models of each layer made from CAD models



Step 2— Layers from molds made for the various layers are added



Step 3—Excess backing removed and added epithelium

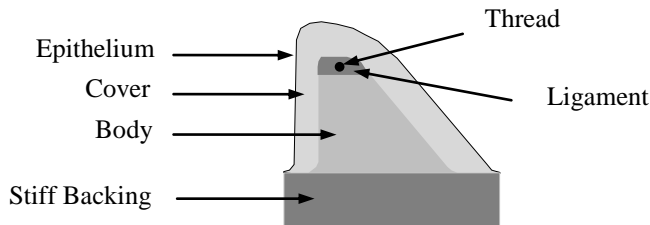


Figure 2-3: Schematic of four-layer model fabrication process, including cross sections of CAD models used for rapid prototyping, mold-making, and creation of the various layers. Shown at bottom is a finished model with all layers.

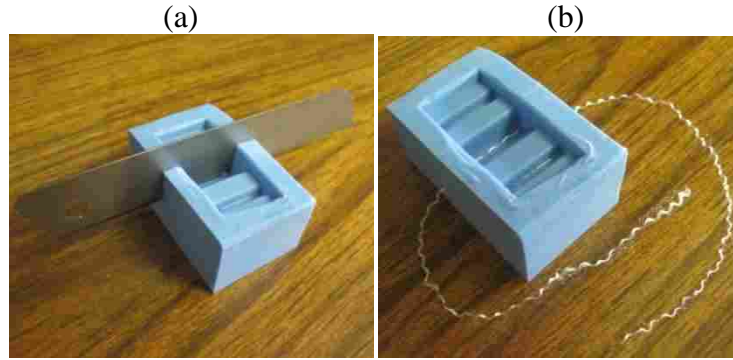


Figure 2-4: Placement of the thread in the mold. (a) The mold for the ligament being cut by the razor. (b) Thread placed in the mold for model fabrication.

Concurrent with the fabrication of each vocal fold model was the simultaneous fabrication of tensile and/or rheological test specimens. Because it was not possible to make all models at the same time, the mean and standard deviation of each test are shown below. The tensile specimens were cylinders 8 mm in diameter and 50 mm long and were tested in an Instron 3342 tensile test apparatus. The testing procedure included a pre-stressing cycle at a rate of 1,000 mm/min, followed by the testing cycle at a rate of 10 mm/min. In each case, the specimen was elongated to 40% strain and the Young's modulus was determined by fitting a linear curve through the data at 20% strain. Typical values for various mixing ratios are given in Table 2-2.

Table 2-2: Young's modulus values measured for various silicone mixture ratios; EF = Ecoflex[®], DS = Dragon Skin[®]. For example, 1:1:4 denotes a mixture of one part EF Part A, one part EF Part B, and four parts Silicone Thinner. Standard deviation shown in parenthesis.

Silicone Mixture	Young's Modulus (kPa)
EF 1:1:4	2.08 (0.573)
EF 1:1:2	3.83 (0.014)
EF 1:1:1	13.6 (0.127)
DS 1:1:1	45.7 (1.70)

The bodies and covers of the M5-UNI, M5-CONV, and MRI models were made using Ecoflex[®] (EF) 1:1:2 and EF 1:1:4 ratios, respectively. The ratios of the EPI model layers were EF 1:1:1, EF 1:1:4, EF 1:1:9, and Dragon Skin[®] (DS) 1:1:1 for the body, ligament, cover and epithelium, respectively. The tensile modulus for the 1:1:9 ratio was not measured because the silicone was so soft that a tensile specimen could not be made; however, its rheological properties were determined as described below. The modulus of the acrylic fiber was estimated to be approximately 2.8 GPa (Norton, 2006).

Rheology is the study of materials with both solid and fluid characteristics (Munson et al., 2006). In this thesis research the rheological properties of the silicone were found by subjecting the material to a controlled strain oscillatory shear test over a range of frequencies. This type of test gives elastic and viscous shear moduli as well as dynamic viscosity. The rheological specimens were disks measuring 40 mm in diameter and 2 mm thick, and were tested using a AR 2000EX Rheometer (TA Instruments, Inc.) The specimens were subject to an oscillation cycle ranging from 1 to 100 Hz with the controlled variable being 4% strain in order to determine the elastic (G') and the viscous (G'') shear moduli (Figure 2-5). The elastic shear moduli of the stiffer silicones were relatively flat, while those of the thinner mixtures were approximately linear at lower frequencies but increased sharply at higher frequencies. For all samples the viscous shear modulus increased as angular frequency increased, with the largest change being observed in the thinnest mixtures. These results showed that the materials were viscoelastic.

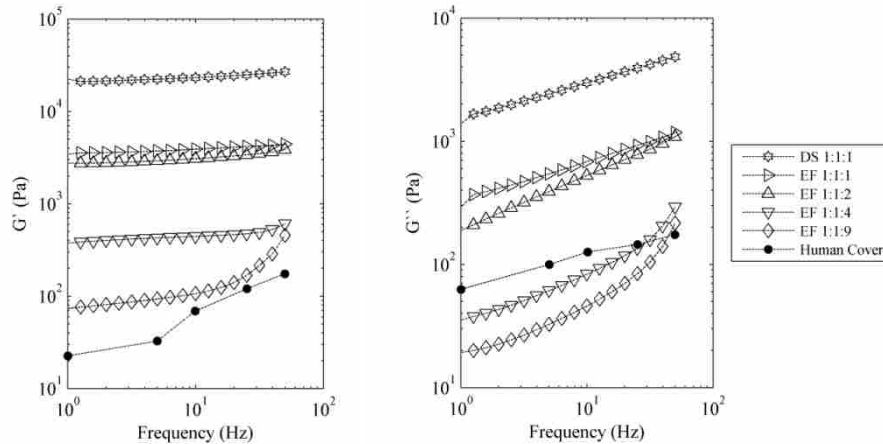


Figure 2-5: Elastic (G') and viscous (G'') shear moduli.

Tensile properties for the various layers of the vocal fold models were similar to those of human vocal fold tissues in the small-strain regime (Titze, 2006; Chan et al., 2007). The rheological properties showed similar trends in G' vs. frequency compared with those reported for human vocal fold tissue. G' of the superficial lamina propria layer (1:1:9 material) and G'' of the ligament layer (1:1:4 material) best matched the magnitude of that of the human vocal fold mucosa (Chan and Titze, 1999; Titze, 2006; Chan and Rodriguez, 2008).

2.3 Experimental Setup and Procedure

Two experimental configurations were used: one to observe the superior surface of the vocal folds (full larynx configuration), and another to observe the medial surface of a single vocal fold (hemilarynx configuration). Data acquired included frequency, onset pressure (the pressure at which vibration begins), maximum glottal gap during vibration (distance from the medial surface of one vocal fold to the other), glottal flow rate, and medial surface motion.

Figure 2-6 shows the full larynx setup. Air flow was supplied by pressurized air connected to a rigid plenum. Air flow was measured by a rotameter-type flow meter (Key Instruments, FR4A37BVBN). A differential pressure transducer (Omega PX 138-001D5V),

mounted approximately 3 cm upstream of the model, measured the subglottal pressure. A high-speed digital camera (Photron APS-RX) with a 105 mm lens (AF Micro Nikkor) acquired images of the model motion at a rate of 3,000 frames per second (fps) and with a 1/6,000 second shutter speed. Four high-intensity LED lights were used for illumination (Visual Instrumentation Corporation 900415).

Onset pressure was determined by increasing pressure until vibration commenced; this was measured five times for each model. High-speed imaging data was acquired at pressures corresponding to 110%, 120%, and 130% of the respective model's measured onset pressure. Images were calibrated using a ruler in the image. The high speed images of the superior surface were processed using a custom MATLAB code that identified the edge of the vocal fold models using grayscale intensity thresholding. This code also calculated the maximum glottal gap. Frequency was found from the subglottal pressure using a data acquisition system (PXI-1042Q) and custom LabVIEW programming.

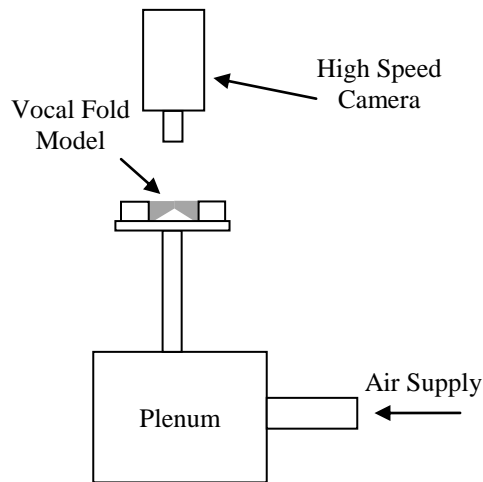


Figure 2-6: Full larynx experimental setup (not to scale).

Tension was applied to the thread in the EPI model by creating a loop with the anterior threads from each vocal fold and hanging a weight (31 g) on the loop. The process was repeated for the posterior threads which enabled the application of 31 g total to the thread of each vocal

fold model. The 31 g weight was selected because it applied sufficient tension to the fiber to restrict the inferior-superior motion without making the thread rigid. The threads were oriented so tension was only applied in the anterior-posterior direction.

In order to view the medial surface of the vocal fold models during vibration, a hemilarynx setup was used (Berry et al., 2001; Boessenecker et al., 2007). This is illustrated in Figure 2-7. The medial surface motion was recorded using two synchronized high-speed digital cameras (Photron SA3) using 50 mm lenses (AF Nikkor) and 12 mm extension rings (AF Zeikos Macro) at 3,000 fps and 1/6,000 shutter speed to capture stereo images of the same event. The same methods as mentioned previously were used to acquire frequency, onset pressure, and flow rate. Tension was applied to the thread of the EPI model in the same manner as in the full larynx tests.

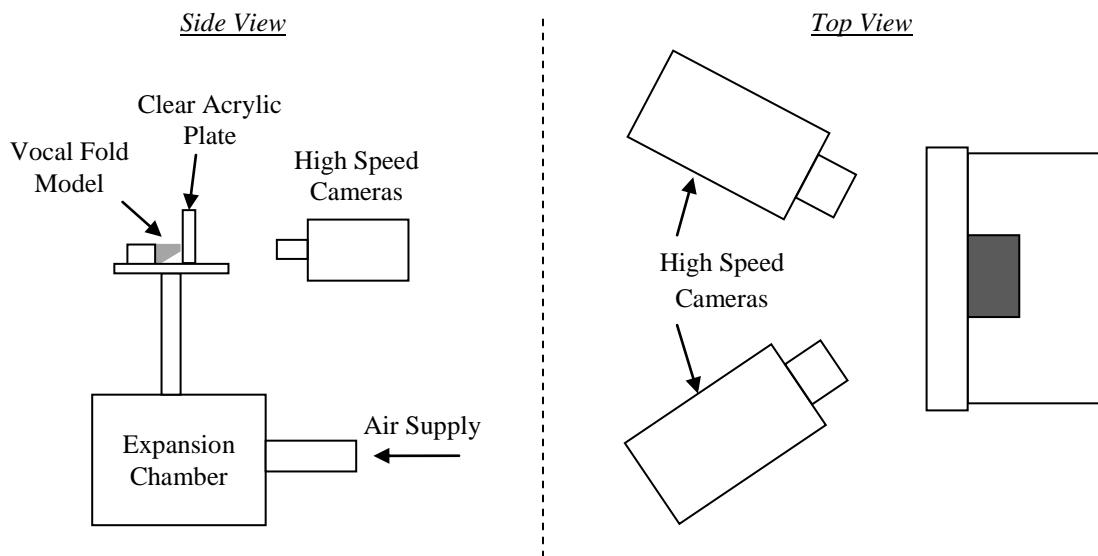


Figure 2-7: Hemilarynx experimental setup (not to scale).

Calibration of the image space was done using a Direct Linear Transform (DLT) (Abdel-Aziz and Kakara, 1971). This method converts point locations from the stereo two-dimensional images to a three-dimensional location. Because the DLT method extrapolates poorly (Chen et al., 1994), a calibration target was constructed to be large enough to encompass the entire

investigation area. One hundred black dots were placed on a calibration target. The target was imaged at several locations in the measurement volume, beginning at the surface of the clear acrylic plate and moving away from the camera in 1 mm increments (0 – 4 mm) with a linear stage (Edmund Optics, NT37-980). This provided 500 data points for calibration. Further details regarding this process are found in Appendix B.

Six dots of black paint (Rust-Oleum, V2178 Flat Black) were applied to the medial and inferior surface of the vocal fold models (Figure 2-8). The dots are labeled A-F beginning with the most superior dot and proceeding in the inferior direction. Matching points were selected manually in each image and used by a semi-automated, custom, cross-correlation tracking program in MATLAB to extract the medial surface trajectories (described in detail below). The lowest dots on the M5-UNI, M5-CONV, and EPI models were not tracked because of minimal movement.

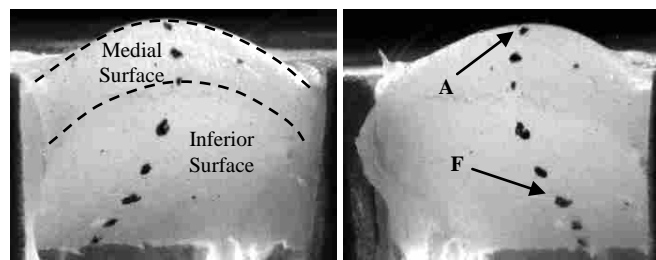


Figure 2-8: Stereo image pair of the M5-CONV model used for medial surface tracking. Direction of air flow is from bottom to top of the images.

2.3.1 Cross Correlation

The points applied to the medial and inferior surfaces of the vocal fold models were tracked by means of a cross correlation algorithm. In essence, the algorithm took two images which were subwindows of two larger images from two steps in time, compared how well they matched, and reconstructed a two-dimensional vector that described where the dot moved (Tropea et al., 2007). This process is described below.

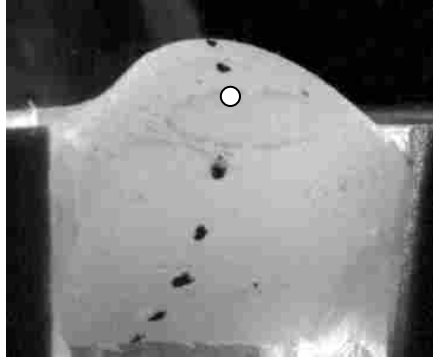


Figure 2-9: Dot selected for input into the cross correlation algorithm. Air flow is from low to high.

Figure 2-9 shows the medial and inferior surfaces of the vocal fold models from a single high-speed camera. The white dot shows the location to be evaluated in the cross correlation algorithm. Figure 2-10 shows 16 x 16 pixel subwindow centered at the pixel location of the dot from the above figure at time i and time $i+1$ (the next image in the time sequence). When comparing the two images, it can be seen that dot at time $i+1$ is slightly up and to the left of the dot at time i .



Figure 2-10: Subwindow of the point at time i and time $i + 1$.

In the cross correlation, the subwindow at time $i+1$ essentially slides around subwindow at time i until the correlation surface reaches a peak (see Figure 2-11, left). The displacement necessary to get the maximum peak is the distance the dot moved between images i and $i+1$.

The described method is only accurate to pixel integer values. Because the true peak is not normally at the exact pixel location, the sub-pixel location of the peak was found by means of a three-point Gaussian curve fit from the surface values of the surrounding pixels. The green

dot is the pixel location of the peak, the red dot is the location of the peak when sub-pixel displacement is applied. As can be seen in Figure 2-11, there is an obvious difference between the integer pixel peak and the sub-pixel displacement peak.

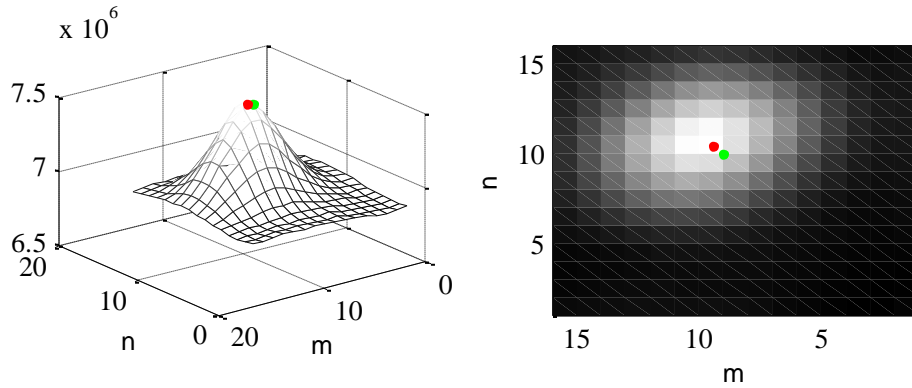


Figure 2-11: Correlation peak (left) and surface map (right) of the cross correlation.

The resulting displacement vector from the correlation surface and sub-pixel displacement is the difference between the dot location in the first and second images. This distance is used to determine the new image pixel location of the dot in time $i+1$.

2.3.2 Cross Correlation Algorithm

With the cross correlation process described, the algorithm used in this thesis to track points from stereo images can now be discussed. In order to extract three dimensional coordinates from the pixel location of the dot, two calibrated images are required. See Appendix B for details on image calibration. As shown in Figure 2-12, synchronized stereo images of the medial and inferior surface were obtained and the dot to track was selected.

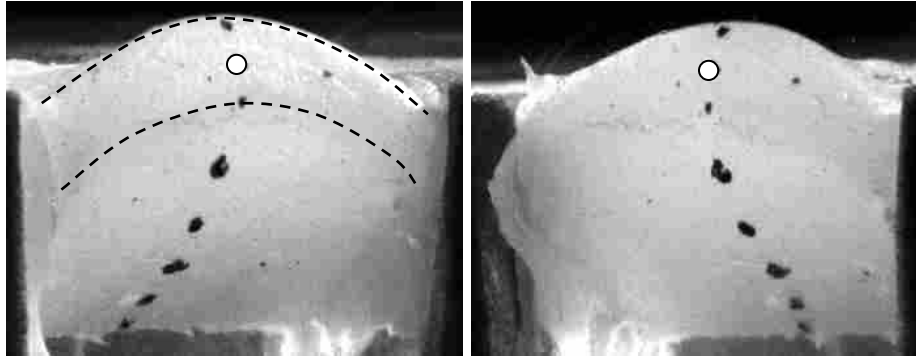


Figure 2-12: Stereo images of the selected dot on the medial surface of the synthetic vocal fold model.

The steps below detail the process of selecting, tracking, and converting the dot pixel locations of each image to obtain three dimensional coordinates.

1. The user manually selects corresponding dots in each image (see Figure 2-12)
2. Because of the difficulty of selecting the center of each dot manually, cross correlation is used to adjust the pixel location in the right image based on the dot location in the left image.
3. Cross correlation is used to track the movement of the point from image i to $i+1$ in each dot's respective image sequence.
4. The dot location in the right image is adjusted using cross correlation to match the location of the dot in the left image.
5. The location of the dots at time $i+1$ are converted to three dimensional coordinates with the calibrated DLT.
6. The process repeats with step 3 until the desired number of image sequences are analyzed.

The algorithm used in this thesis was written in MATLAB and is found in Appendix D.

2.3.3 Phase Delay and Wave Velocity

Two quantitative measures of medial surface motion were calculated using velocity data of the tracked points: phase difference and mucosal wave velocity. The mucosal wave is the vertically propagating wave that is manifest along the vocal fold medial surface. Assuming the wave propagates vertically with a velocity c , the time delay, τ , between points separated by a distance z is

$$\tau = \frac{z}{c}, \quad 2-1$$

and the corresponding phase delay, normalized by the fundamental period T , is:

$$\phi = \frac{2 \pi \tau}{T} = 2 \pi \tau F_0 = \frac{2 \pi z F_0}{c}, \quad 2-2$$

where F_0 is the fundamental frequency of vibration. This quantity can be expressed as degrees instead of radians and divided by z to obtain phase delay in units of degrees per mm:

$$\frac{\phi}{z} = \frac{360^\circ F_0}{c}. \quad 2-3$$

The velocity, c , was determined by first finding the peaks of the trajectories of points A and C in the lateral direction as they moved toward the clear acrylic plate. This distance between the two points at their max was then divided by the difference in time for each of the points to reach their peaks to obtain the velocity.

2.3.4 Experimental Procedure

For comparison purposes, each model was vibrated at 110%, 120%, and 130% of its onset pressure, and measures of frequency, maximum glottal width, and flow rate were acquired. Additionally, each model was placed in a hemilarynx setup and wave velocity and phase delay

were extracted from stereo images. Uncertainty estimates for each measured variable were calculated as seen in Table 2-3. Details are given in Appendix C.

Table 2-3: Uncertainty estimate in each measurement.

Metric	Uncertainty	Units
Subglottal Pressure	±34.5	Pa
Onset Pressure	±63.9	Pa
Glottal Flow Rate	±42.5	ml/s
Acoustic Frequency	±0.2	Hz
Glottal Gap	±0.05	mm
Trajectories	±0.28	mm

2.4 Results and Discussion

2.4.1 Onset Pressure

For each model, the onset pressure (P_{on}) was determined by increasing the subglottal pressure until vibration began. This process was repeated five times and the average and standard deviation were determined (see Table 2-4). Typical values for human vocal folds are presented for comparison purposes (Baken and Orlikoff, 2000).

Table 2-4: Mean and standard deviation (in parentheses) of onset pressures for the various models in the symmetric and hemilarynx experimental setups.

Model	Onset Pressure (kPa)	
	Symmetric Setup	Hemilarynx Setup
M5-UNI	0.84 (0.008)	1.36 (0.011)
M5-CONV	0.87 (0.007)	1.11 (0.011)
MRI	1.68 (0.005)	1.89 (0.013)
EPI, no tension	0.37 (0.009)	0.50 (0.005)
EPI, with tension	0.27 (0.022)	0.43 (0.013)
Human	0.29-0.49	N/A

2.4.2 Vibration Frequency

The MRI model had the highest frequency of all models (see Figure 2-13). The EPI model with no tension had the lowest frequency due to the soft cover and little support from the thread. Adding tension to the thread increased the frequency of the EPI model by approximately 10 Hz.

Pickup and Thomson (2011) predicted that a convergent pre-phonatory intraglottal convergence angle would decrease the vibration frequency. The results from the M5-UNI, and M5-CONV tests were in agreement with this hypothesis. The vibration frequency for all models at all subglottal pressures fell within the range of the human voice (98 – 246 Hz) (Titze, 2000).

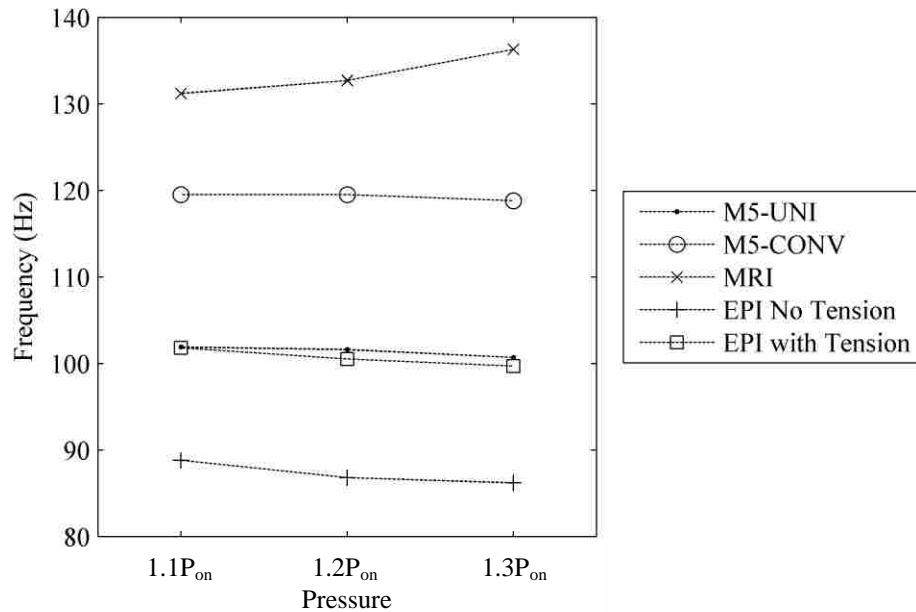


Figure 2-13: Frequency response for the various models at 110%, 120% and 130% of their respective onset pressures. M5-UNI (•), M5-CONV (○), MRI (×), EPI without tension (+), and EPI with tension (□).

2.4.3 Maximum Glottal Gap

As can be seen from Figure 2-14, the model with the largest maximum glottal width was the M5-UNI model. The M5-CONV and MRI models had comparable maximum glottal widths. The resulting maximum glottal gap of the M5-CONV model versus the M5-UNI was the opposite of what was predicted by Pickup and Thomson (2011). The maximum glottal width of the EPI model decreased by approximately 1 mm when tension was applied to the fiber. It also had the smallest glottal gap of all models tested. For excised human vocal folds, the range of

maximum glottal width is approximately 0.5 to 4 mm (Doellinger and Berry, 2006b). The vibratory response of all models was similar to these values.

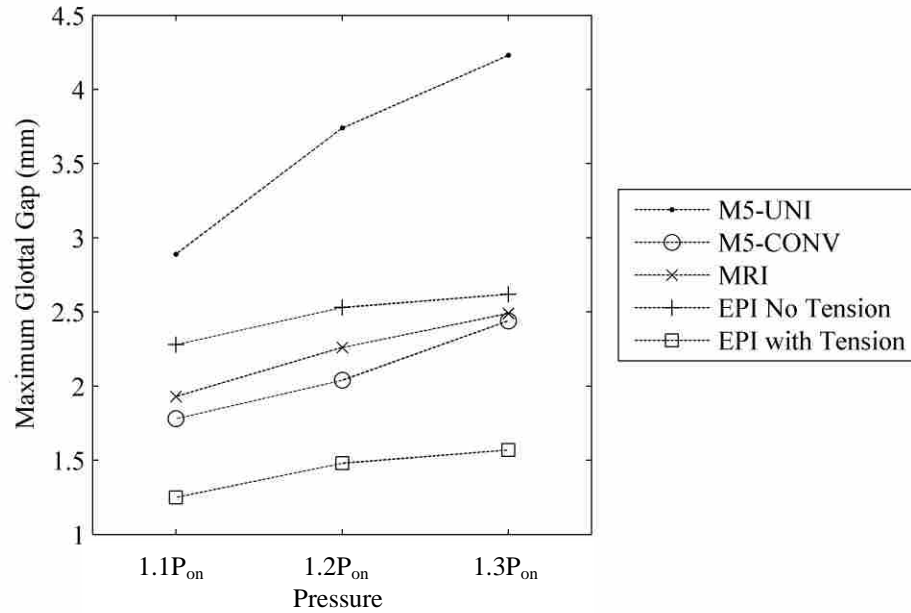


Figure 2-14: Maximum glottal width of the models at 110%, 120% and 130% of their respective onset pressures. Symbols are the same as listed in Figure 2-13.

2.4.4 Glottal Flow Rate

The MRI model had the highest flow rate which was likely due to the higher subglottal pressure required to induce vibration (see Figure 2-15). The M5-CONV model had a lower flow rate than the M5-UNI model (again, which was opposite of that which was predicted by Pickup and Thomson (2011)). The EPI model without tension had almost twice the flow rate as the EPI model with tension. The large difference in the flow rate of the EPI model was due primarily to the smaller glottal gap during the oscillation cycle. Only the EPI with tension model was similar to the mean airflow during sustained phonation for humans of 70 to 220 ml/s (Baken and Orlikoff, 2000).

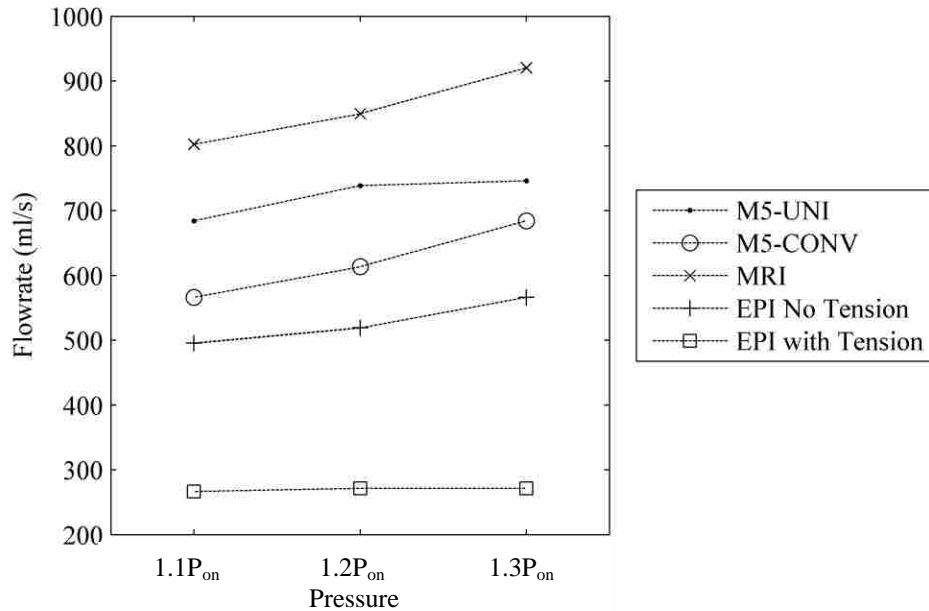
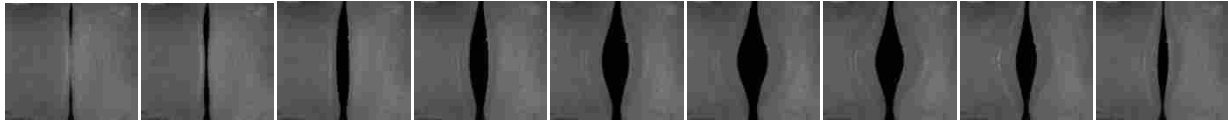


Figure 2-15: Flow rate of the models at 110%, 120% and 130% of their respective onset pressures. Symbols are the same as listed in Figure 2-13.

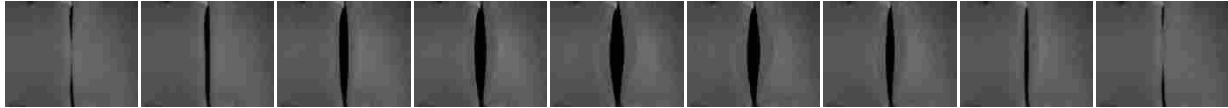
2.4.5 Superior Surface Imaging

Superior views of one period of oscillation for each model at 120% of onset pressure are shown in Figure 2-16. The large glottal width of the M5-UNI model is evident, and it can be seen that the M5-UNI and M5-CONV models exhibited primarily divergent medial surface profiles over the oscillation period (discussed further below). The MRI model exhibited an anterior-posterior wave believed to be due to the asymmetric nature of the vocal fold model. The EPI model with and without tension had similar vibration cycles, with the magnitude being reduced with applied tension. These results show that the EPI and MRI models showed the most realistic vibratory response.

M5-UNI



M5-CONV



MRI



EPI no tension



EPI with tension



Figure 2-16: Superior view showing high-speed images from the five models. All images were obtained with the models vibrating at 120% of their respective onset pressures.

Videokymography is defined as monitoring one line of pixels perpendicular to the glottal opening during the oscillation cycle (Svec and Schutte, 1996). As shown in Figure 2-17, the high-speed image sequences are rotated 90 degrees and a column of pixels is selected. The column of pixels is then tracked over time.

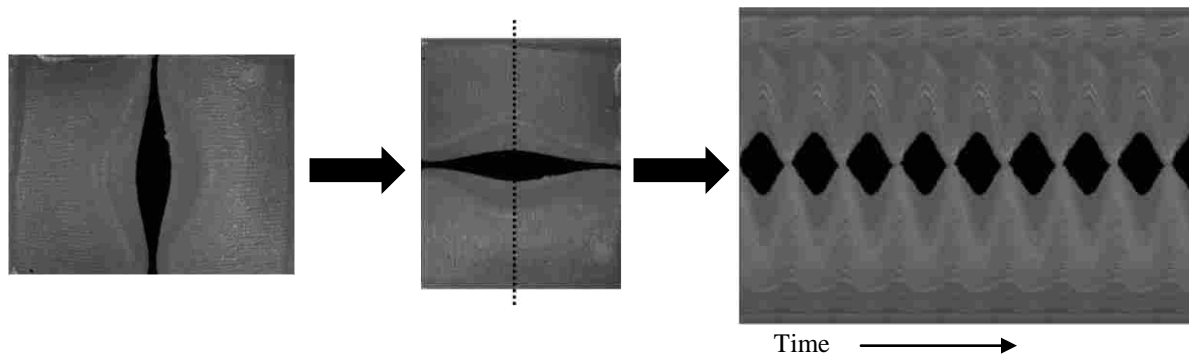


Figure 2-17: Process of extracting kymograms from high-speed images of the superior surface.

Applying this method to one cycle of oscillation for the four different models gave insight into the movement of the medial surfaces of the synthetic models. During human phonation, the superior margin hides the inferior margin of the medial surface because of a convergent profile during the opening phase (Titze et al., 1993). As can be seen in Figure 2-18, the vibration pattern for the M5-UNI and M5-CONV were similar in that the inferior margin of the medial surface was hidden for only a small part of the opening cycle showing the models do not exhibit a defined convergent profile during the opening phase. The MRI model and EPI models with and without tension showed the superior margin of the medial surface hiding the inferior margin for a large portion of the opening phase and a divergent profile for the remainder of the cycle similar to the kymograms of human larynges (Svec et al., 2007). Although these models exhibit improved convergent/divergent motion, the superior margin of healthy human vocal folds hide the inferior margin for a longer duration due to a more pronounced mucosal wave motion (Svec et al., 2007).

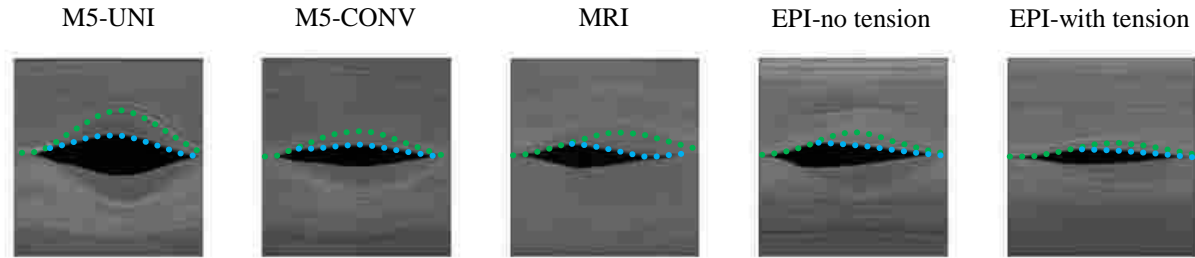


Figure 2-18: High-speed kymograms of one period for the four models. Estimated locations of the superior (green) and inferior (blue) margins shown by dotted lines.

2.4.6 Medial Surface Tracking

Using the hemilarynx configuration, the location of the applied points were converted from stereo image pixel location to three-dimensional space and the anterior-posterior and medial-lateral positions plotted at several phases of a cycle (see Figure 2-19). The first image of each row shows a closed glottis. All models were vibrated at 120% of the respective hemilarynx onset pressure (see Table 2-3). In the images, the flow was in the bottom-to-top direction, and the gray dashed line represents the glottis midline (or the position of the acrylic plate).

In all cases except for the MRI model, the upper three points were on the medial surface. The data showed that the M5-UNI and M5-CONV models had a primarily divergent medial surface profile throughout the oscillation period. The MRI model had distinct medial surface movement because of its unique geometry and exhibited a mucosal wave from the inferior to superior portion of the model. The EPI model with and without tension showed reduced vertical displacement (compared with the M5 models), a mucosal wave in the medial surface, and an alternating convergent/divergent profile (convergent during opening, divergent during closing).

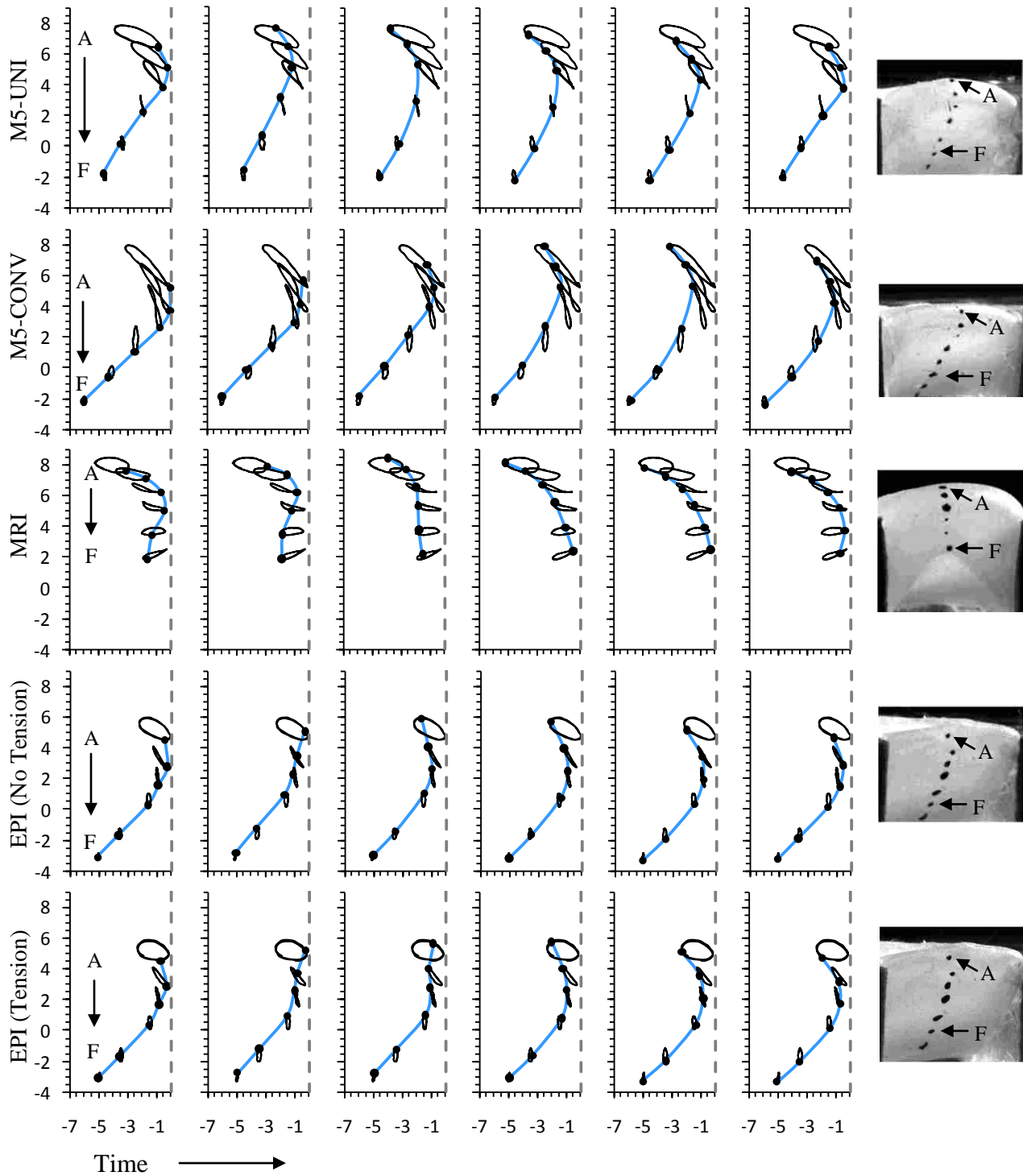


Figure 2-19: Vocal fold model motion at six phases of oscillation. Axes denote position in mm. Flow is in the inferior (bottom) to superior (top) direction. The dashed line denotes the glottis midline (position of the clear acrylic plate). The elliptical lines show the position of the dots through one period of oscillation. The solid blue line is a spline interpolation between dots, illustrating the position of the medial surface at the given phase.

The maximum absolute velocities of each extracted point were found by determining the distance traveled between each point and dividing by the time step (see Figure 2-20). The M5-UNI and EPI models had comparable values. The MRI model showed the entire surface having approximately the same maximum absolute velocity. The M5-CONV model showed the highest maximum velocity of approximately 1.8 m/s. There was also little difference in maximum absolute velocity for the EPI model with and without tension due to the similarity of their point trajectories.

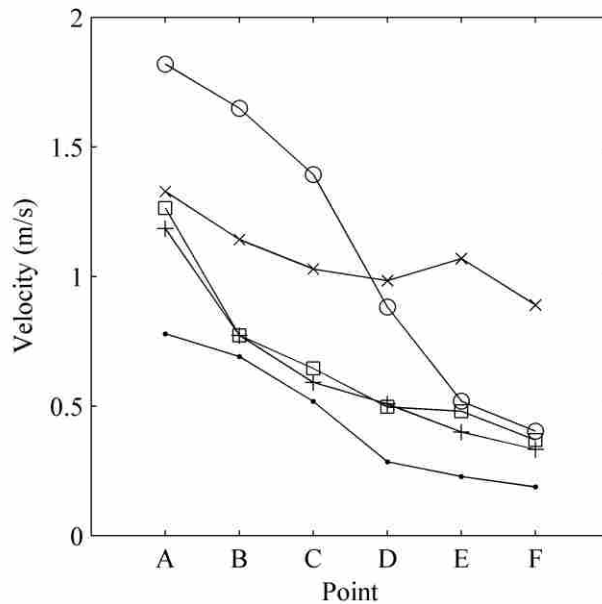


Figure 2-20: Velocity of each applied dot for all models. M5-UNI (●), M5-CONV (○), MRI (×), EPI without tension (+), and EPI with tension (□).

Table 2-5 shows the maximum values of quantities of interest from the hemilarynx experiment for each model. A comparison of these results with sample data from the literature on excised human vocal fold hemilarynx experiments showed that all models have a greater lateral displacement (greater than 0.3 mm) than what was reported. With the exception of the MRI model, all the models also had a larger maximum vertical displacement than human vocal folds. However, the EPI model with and without tension had similar values for maximum lateral and

vertical displacements. Conversely, the maximum absolute velocity for all models fell within the range of results. In general, the MRI and EPI models all are comparable to the values reported in the literature.

Table 2-5: The computed maximum values of point displacement and velocity.

Parameter	M5-UNI	M5-CONV	MRI	EPI-No Tension	EPI-Tension	Representative Value in Literature
Max lateral displacement	3.10	3.15	2.46	2.20	2.27	1.90 (Boessenecker et al., 2007)
Max vertical displacement	1.82	3.12	0.98	1.47	1.42	1.36 (Doellinger et al., 2005)
Max absolute velocity	0.78	1.82	1.32	1.18	1.26	1.62 (Doellinger et al., 2005)

Wave velocity and phase delay values calculated using points A and C are listed in Table 2-6. The values for wave velocity were similar to those reported from experiments on excised larynges (Titze et al., 1993). However, only the phase angle for the EPI model with and without tension fell within data from the same study. The models with the highest and lowest wave velocities were the MRI and EPI with tension models, respectively. There was a trend of decreasing phase angle with higher velocity.

Table 2-6: Mucosal wave velocities for all models. All models were vibrated at 120% of P_{on} .

Model	Wave Velocity (m/s)	Phase Angle per mm ($^{\circ}$/mm)	Frequency (Hz)	Subglottal Pressure (kPa)
M5-UNI	2.76	13.4	102.6	1.50
M5-CONV	2.82	15.9	118.8	1.23
MRI	3.33	15.1	128.5	2.08
EPI-No Tension	1.27	24.7	87.0	0.55
EPI-Tension	1.18	30.1	98.4	0.47
Human	0.5-2.2 ¹	24-60 ¹	95-180 ¹	0.3-0.6 ²

¹ Titze et al. (1993)

² Baken and Orlikoff (2000)

2.5 Conclusion

Four synthetic vocal fold models were evaluated by measuring onset pressure, frequency, maximum glottal width, flow rate, and medial surface motion, and comparing the results to experiments on excised human larynges. The EPI model had the lowest onset pressure, smallest maximum glottal width, and lowest flow rate. Both the MRI and EPI models showed a convergent/divergent motion and a mucosal wave while the M5-UNI and M5-CONV were primarily divergent through the oscillation cycle. The motion of the medial surface of the EPI model (displacement and velocity) best matched published data from hemilarynx experiments. This was likely due to the effects of an extremely soft cover, additional layers, and introduction of a fiber in the ligament layer.

Although there are advantages to the EPI model, it has limitations. It is more difficult to fabricate because of the added layers and incorporation of a soft cover layer. Additionally, due to the delicate nature of the cover layer, it is not able to withstand extremely large deformations (although it could withstand the deformations encountered in the present study). Finally, the geometry is still somewhat idealized and, with the exception of the fiber in the ligament layer, is isotropic.

It is anticipated that the development of more realistic materials would aid in creating even more accurate vocal fold models. In this study, tension was either absent or present, and it would be illuminating to study the effect of adding various degrees of tension on the vibratory response. Furthermore, the location of the fiber was located approximately in the center of the ligament layer of the vocal fold model. A study of the effect of placement location would enable a better understanding of the roles of the fibrous ligament and muscle layers.

3 EFFECT OF AUGMENTATION INJECTION ON BOWED SELF-OSCILLATING SYNTHETIC VOCAL FOLD MODELS³

A life-sized, synthetic, multi-layer, self-oscillating vocal fold model was created that simulated bowing. Model bowing was accomplished by a decrease in volume of the body layer relative to that of a normal, unbowed model. Material properties of the several layers were unchanged. Two models with varying degrees of bowing were created and tested while paired with normal models. Following initial acquisition of data (onset pressure, vibration frequency, glottal flow rate, and high-speed image sequences), bowed models were then injected with silicone that had material properties similar to those used in augmentation procedures. Three different silicone injection quantities were tested: sufficient to close the glottal gap, insufficient to close the glottal gap, and excess silicone to create convex bowing of the bowed model. The above-mentioned metrics were again taken and compared. Pre- and post-injection high-speed imaging data were also acquired using a hemilarynx setup, from which medial surface dynamics were quantified.

3.1 Introduction

Vocal fold bowing can be caused by various pathologies such as scarring of the vocal folds (Paniello and Titze, 2008), structural changes to the vocal folds from aging (presbylarynx)

³ This work was presented at the 40th Annual Symposium: Care of the Professional Voice in Philadelphia, Pennsylvania June 2nd, 2011

(Kendall, 2007), and atrophy of the thyroarytenoid (TA) muscle from partial or complete paralysis (Isshiki, 1989). The consequence is one or both of the vocal folds not closing properly (glottal incompetence), generally causing a breathy voice and reduced sound intensity. Because extra effort is required to overcome glottal incompetence, prolonged or loud speech is limited (Baker et al., 2001).

Even though procedures such as medialization laryngoscopy or augmentation injections of collagen or Botox have had some success in correcting disorders of the cover layer, obtaining consistency in alleviating glottal incompetence remains a challenge. Several factors contribute to inconsistent results in terms of correcting the glottal gap and restoring desired vibration, one of which is that there are no methods of simulating the pre- and post-surgical vibratory responses apart from clinical and canine experiments (Paniello and Titze, 2008). The purpose of this chapter is to describe a synthetic vocal fold model with a designed pathology that allowed for pre- and post-vibratory responses to be simulated, thereby allowing for a focused study on changes to flow-induced vibratory response due to geometric and material-related effects following injection.

Synthetic models have been used in numerous studies in recent years to explore the physics of vocal fold vibration. Ideally, the models self-oscillate in a manner similar to the true vocal folds in order to be representative of laryngeal coupled fluid-structure-acoustic interactions (Kniesburges et al., In press). To this end, several types of self-oscillating synthetic models have been used. Membranous models which approximated the epithelium and superficial layer of the lamina propria have been developed and used to study the effects of viscosity, epithelium thickness, and intraglottal angle on vocal fold vibration (Titze et al., 1995; Chan et al., 1997; Chan and Titze, 2006). In these models only the epithelium and superficial layer of the lamina

propria were modeled. One- and two-layer self-oscillating models based on the geometry of Scherer et al. (2001) (see Figure 3-1) have been developed (Thomson et al., 2005; Riede et al., 2008). These models have been used to study subglottal flow (Misun et al., 2011), flow-structure interactions (Becker, et al., 2009), glottal airflow (Neubauer et al., 2007; Drechsel and Thomson, 2008), material asymmetries (Pickup and Thomson, 2009), and contact stress (Spencer et al., 2008). These models have demonstrated similarities with human vocal fold vibration with respect to frequency, amplitude, and vibratory pressures. Advantages to these models include reproducibility, low cost, and ease of parameterization. Primary disadvantages include unnaturally large inferior-superior displacement, lack of a clear mucosal wave, higher-than-desired onset pressure (usually 1 to 2 kPa, compared with 0.2 to 0.4 kPa for human phonation), and a generally divergent profile during vibration (Pickup and Thomson, 2010).

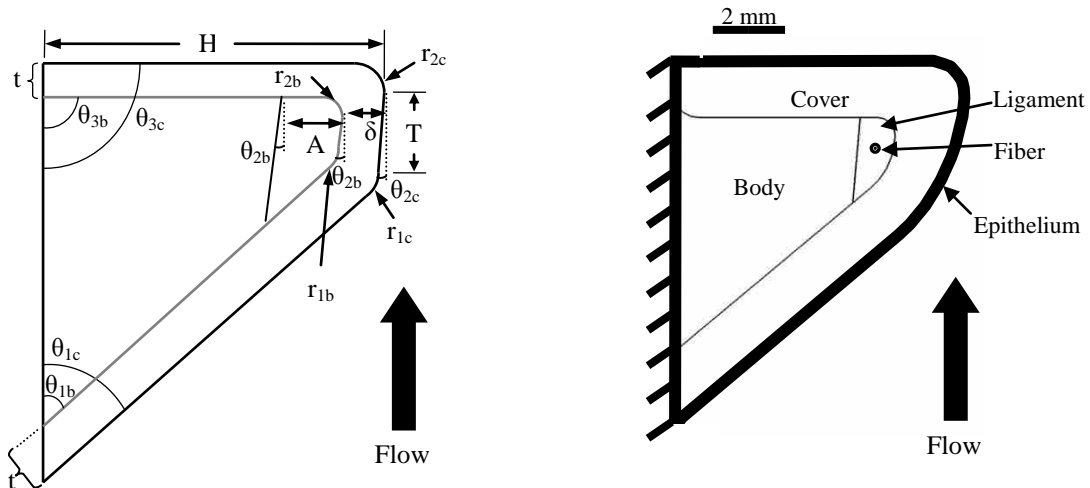


Figure 3-1: Parameters defining vocal fold geometry (left) and cross section of normal model developed in Chapter 2 (right).

The model from Chapter 2 included body, ligament, superficial lamina propria, and epithelium layers with material properties and layer geometries that are reasonably representative of the human vocal folds (see Figure 3-1). An acrylic fiber was placed in the center of the ligament layer in the anterior-posterior direction; this introduced anisotropy and reduced inferior-superior motion. This multi-layer model was shown to vibrate similar to human vocal fold vibration in terms of onset pressure (around 300 to 400 Pa), frequency (around 100 to 120 Hz), and flow rate (250 to 550 ml/s). Importantly, it also exhibited mucosal wave-like motion, or a vertically propagating wave important to phonation (Bless et al., 1987), and alternating convergent-divergent motion during vibration.

In the present study, this multi-layer model was used to quantify the pre- and post-injection vibratory responses. This was done by (1) generating a synthetic model with geometric changes that resulted in a bowed geometry, and (2) comparing the flow-induced responses of bowed synthetic models before and after injecting materials to correct for bowing.

3.2 Methods

3.2.1 Synthetic Model

The multi-layer, synthetic, self-oscillating vocal fold model developed in Chapter 2 was altered to simulate vocal fold bowing (see Figure 3-2). The normal, baseline geometry was defined using parameters as shown in Figure 3-1, with parameter values as listed in Table 3-1. A dimension was defined in the medial-lateral direction in the center of the model as shown in Figure 3-3. For bowing, this dimension was decreased by 10% or 20% of its original value and the body layer volume reduced. No change was made to the material properties or to the relative geometries of the ligament, superficial lamina propria, or epithelium layers.

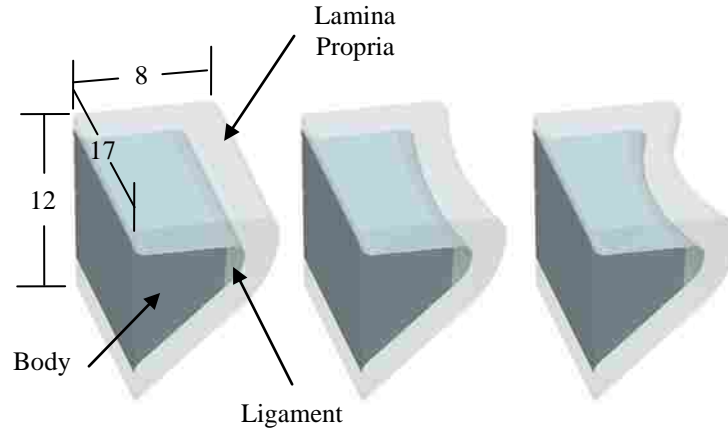


Figure 3-2: Normal model compared with the 10% (middle) and 20% (right) bowed models, respectively. Flow is from bottom to top. (Epithelium and fiber not shown)

Table 3-1: Geometric parameters and description used to define model.

Parameter	Value	Description
$\theta_{1b,c}$	50°	Inferior glottal angle
$\theta_{2b,c}$	5°	Intraglottal angle
$\theta_{3b,c}$	90°	Superior glottal angle
r_{1c}	6.0 mm	Cover entrance radius
r_{2c}	0.987 mm	Cover exit radius
r_{1b}	2.0 mm	Ligament entrance radius
r_{2b}	0.513 mm	Ligament exit radius
T	0.1 mm	Vertical glottal thickness
t	1.6 mm	Inferior and superior cover layer thickness
δ	2.0 mm	Maximum medial cover layer thickness
D	8.4 mm	Lateral depth
A	1 mm	Ligament layer thickness

Model fabrication details can be found in Appendix A, so only summary information is provided here. Three-dimensional computer models were used to generate rapid prototypes from which molds for the different layers were created. The models were made by casting the layers using three-part addition-cure silicone. Varying the mixing ratio used in making the silicone materials allowed for cured layers of different stiffness to be fabricated. Each life-sized vocal fold model measured approximately according to the dimensions shown in Figure 3-2. The anterior, posterior, and lateral surfaces of the models were adhered to acrylic mounting plates in

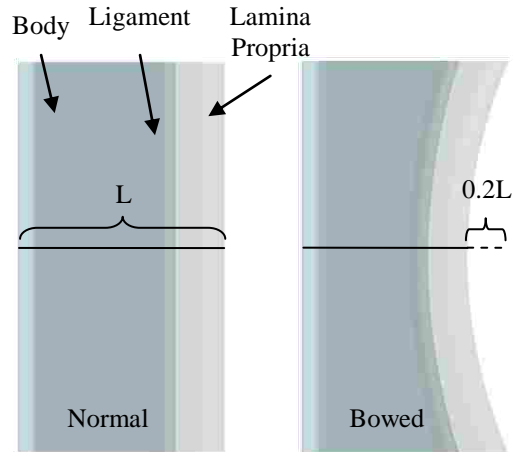


Figure 3-3: Superior view of normal (left) and bowed (right) vocal fold models showing bowing definition. Flow direction is out of the page. Epithelium and fiber are not shown.

a manner similar to that which has been used in previous models (e.g., Thomson et al., 2005).

The model-mounting plate assemblies were attached to the end of a flow supply tube (described below) for testing.

For each model a stiff thread, oriented in the anterior-posterior direction, was imbedded in the ligament layer. This was done to reduce inferior-superior motion during model vibration. Tension was applied to the thread by suspending weights (31 g each) to the anterior and posterior ends of the thread (the thread extended beyond the model anterior and posterior surfaces). The thread and weights were directed such that the thread was only pulled in the anterior-posterior direction.

3.2.1.1 Material Properties

To quantify material properties, test specimens were made concurrently with fabrication of each layer. Body, ligament, and epithelium layer Young's modulus values were determined by testing cylindrical (50 mm long, 8 mm in diameter) specimens in an Instron 3342 tensile-testing apparatus. Each specimen was elongated to 40% strain during both a 10 iteration pre-cycling

phase at a rate of 1,000 mm/min and a one iteration testing phase at 10 mm/min. The Young's modulus was determined by fitting a linear curve through the data at 20% strain.

Rheological properties (elastic and viscous shear moduli) of the superficial lamina propria were determined by testing disks (2 mm thick, 40 mm in diameter) in a TA Instruments AR 2000EX rheometer. Each specimen was subject to an oscillatory sweep from 0.1 to 100 rad/sec and 4% strain. Results of these material property tests are discussed below.

Tensile test results for the body, ligament, epithelium, and injection materials are listed in Table 3-2. Since all models were not made simultaneously, multiple material samples were made (one sample for each layer for each model), the average Young's modulus value for each layer is shown along with the corresponding standard deviation. The material properties are comparable to previously-measured small-strain regime properties of human vocal fold tissues (Titze, 2006; Chan et al., 2007).

Table 3-2: Young's modulus for each layer of the synthetic model. Standard deviation is shown in parentheses.

Model Section	Modulus (kPa)
Body	11.82 (1.05)
Ligament	1.63 (0.90)
Epithelium	49.78 (4.15)
Injection	12.62 (6.86)

The rheological test results are shown in Figure 3-4. Again, not all models could be made simultaneously so the mean and standard deviation of each layer are shown. Both the elastic and viscous shear moduli (G' and G'' respectively) increased with increasing frequency showing the materials are viscoelastic. These followed a similar trend of increasing shear and viscous shear moduli with increasing angular frequency compared to human vocal fold tissue (Titze, 2006; Chan et al., 2007; Chan and Rodriguez, 2008).

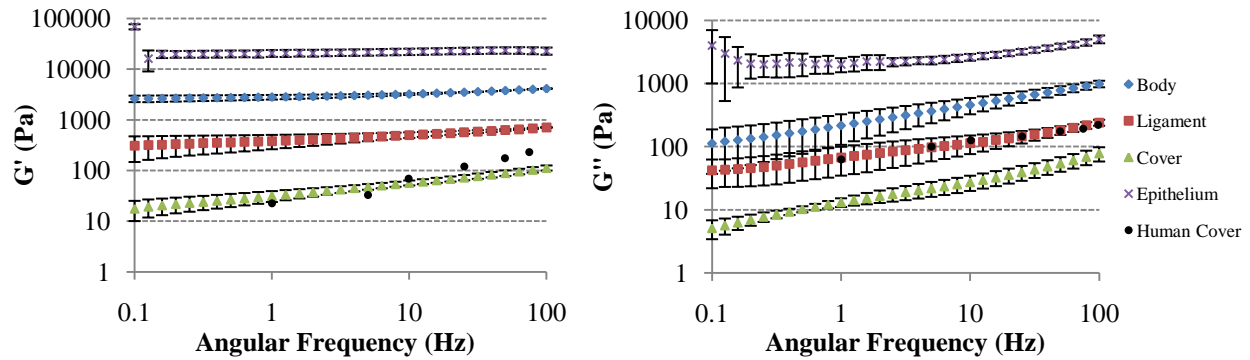


Figure 3-4: Elastic shear modulus (G' , left) and viscous shear modulus (G'' , right) for the four layers used in the models. Error bars show one standard deviation.

3.2.1.2 Injections

As shown in Figure 3-5, the bowed model mounting plates were modified to allow for injection of material after pre-injection vibratory data was acquired. The injections were placed at the lateral margin of the body using a syringe (500 μ l, SY133500, Hamilton Company) and hypodermic needle (22 gage, 1.5 inch long, 305156, Becton Dickinson & Co). The injection experimental protocol is discussed in more detail below in section 3.3.1.1.

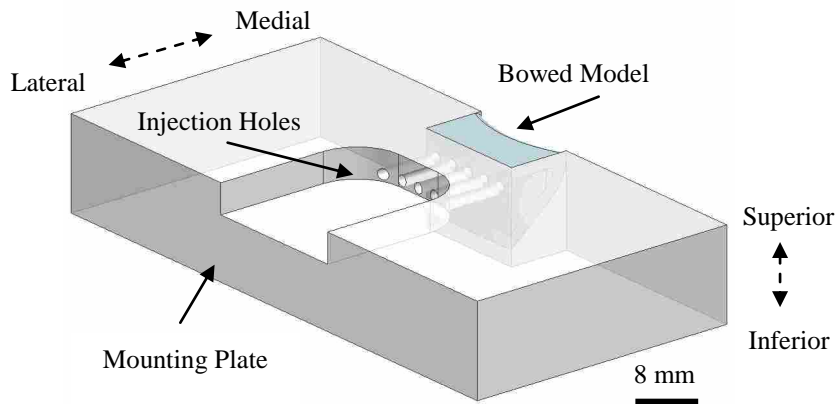


Figure 3-5: Mounting plate with holes for injecting material laterally in the bowed models. Flow direction is from inferior to superior.

An addition-cure silicone injection material was chosen that has material properties comparable to two materials that are currently used in vocal fold augmentation surgery: Radiesse[®] and Cymetra[®] (Caton et al., 2007). The material consisted of one part A of Ecoflex[®] 0030, one part B of Ecoflex[®] 0030 and two parts Silicone Thinner (all products manufactured by Smooth-On, Inc.; parts were measured by weight). An additional 10% of a cure accelerant (Plat-Cat, Smooth-On, Inc.) by weight of part A was added. Figure 3-6 shows a comparison of the rheological properties of the injected material with Radiesse[®] and Cymetra[®] (Caton et al., 2007).

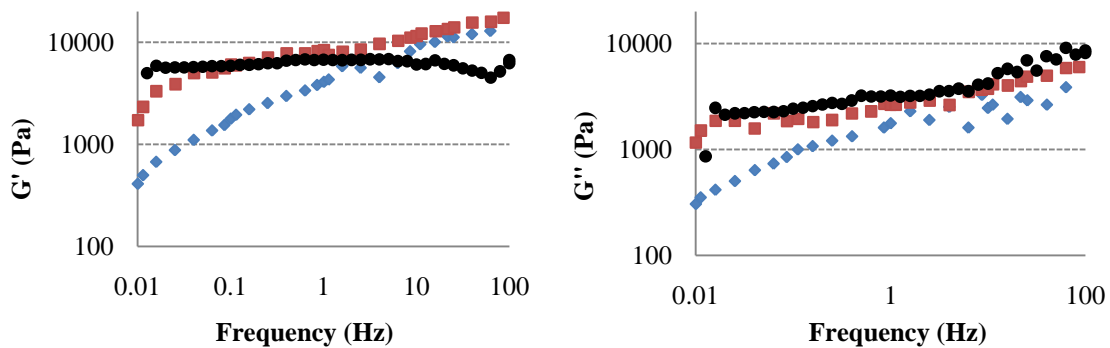


Figure 3-6: Rheological comparison of the elastic (left) and viscous (right) shear moduli of the injected material with two common bio injections. ●, ■, and ◆ are the injected material, Cymetra, and Radiesse materials (the latter from Caton et al., 2007).

3.2.2 Experimental Setup

Two configurations were used in this experiment: a full larynx configuration in which a normal model was paired with a bowed model, and a hemilarynx configuration that consisted of a single bowed model. The full larynx setup was used to acquire pre- and post-injection onset pressure, frequency, flow rate, open quotient, and glottal gap high-speed imaging data. The hemilarynx setup was used to track pre- and post-injection medial surface motion.

3.2.2.1 Full Larynx Configuration

The full larynx setup is shown in Figure 3-7. Pressurized air entered an expansion chamber which provided approximately uniform pressure to a 0.95 cm, 50 cm long flexible PVC

tube that was rigidly secured to a fixed post. Airflow was regulated by means of a manual valve and measured with a rotameter-type flow meter (Key Instruments, FR4A37BVBN). Prior to injection each bowed model and mounting plate assembly was paired with a normal model and mounting plate assembly. The pairing was accomplished by screwing the mounting plates together such that the medial surfaces nearly touched. The mounting plates were mounted at the end of the PVC tube.

Mean subglottal pressure was acquired approximately 3 cm upstream of the vocal fold models with a differential pressure transducer (Omega PX 138-001D5V) and collected with a National Instruments system (PXI-1042Q) using LabVIEW programming.

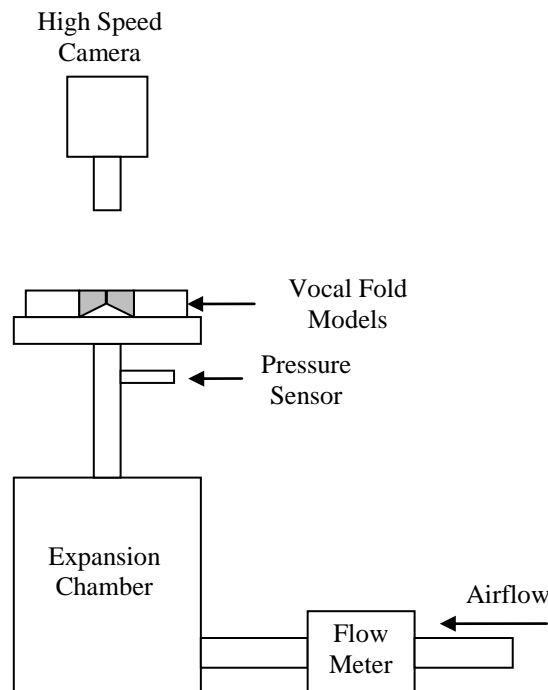


Figure 3-7: Full larynx experimental configuration (not to scale).

A digital high-speed camera (Photron SA3) was positioned approximately 13 cm above the model and acquired images at 3,000 frames per second with a 1/6000 shutter speed and 512×512 pixel resolution. The camera used a 50 mm lens (AF Nikkor) and a 20 mm extension tube (AF Zeikos Macro). Four high-intensity LED lights and controller (Visual Instrumentation

Corporation #900415, #200900) illuminated the image area. High-speed images were acquired at 110% and 120% of each model's respective onset pressure. The open quotient was estimated by dividing, over one period, the number of images showing glottal closure at the approximate anterior-posterior midplane by the total number of images spanning one period.

3.2.2.2 Hemilarynx Configuration

A hemilarynx configuration, consisting of a single model vibrating against a clear acrylic plate (see Figure 3-8), was used to track bowed model medial and inferior surface motion in a manner similar to that which has been done previously (Berry et al., 2001; Boessenecker et al., 2007) and described in detail in Chapter 2. Two synchronized high-speed cameras (Photron SA3), each using the same lens hardware and image acquisition settings as in the full larynx experiments, were used to acquire stereo images of the model during vibration.

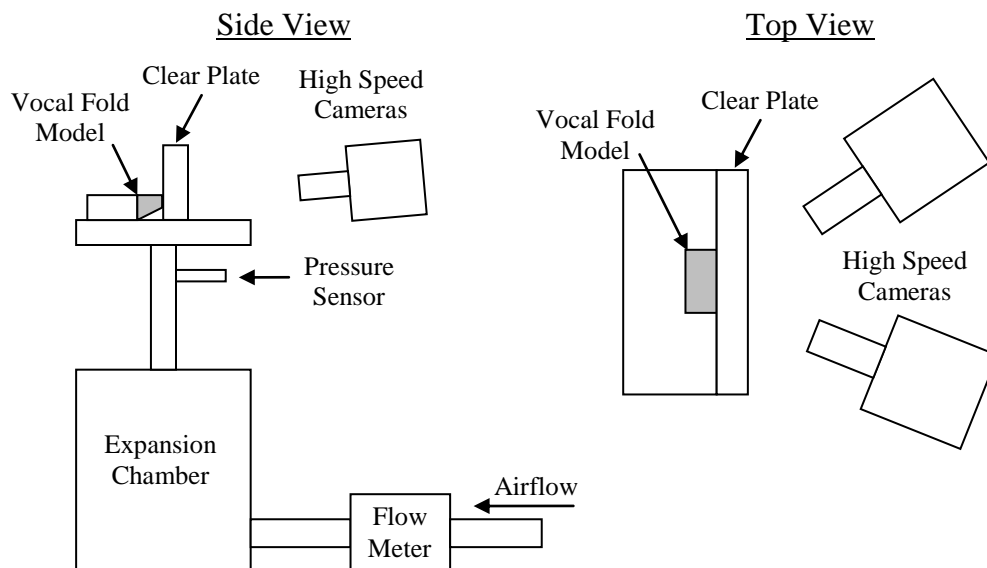


Figure 3-8: Hemilarynx experimental configuration (not to scale).

As in Chapter 2, the point locations were identified using the direct linear transformation (DLT) (Abdel-Aziz and Kakara, 1971; Berry et al., 2001; Doellinger et al., 2005). Prior to model mounting a planar calibration target was traversed laterally through the measurement volume in

1 mm increments by means of a translation stage (Edmund Optics, NT37-980). The calibration target had a rectangular grid of 5 by 5 dots with an inter-dot spacing of approximately 2 mm. The calibration began at the face of the clear acrylic plate and ended 4 mm away (0-4 mm), thereby providing known locations of 500 points. Details are found in Appendix B.

Before mounting the bowed models in the hemilarynx configuration, a grid of 25 black dots were applied to the medial and inferior surfaces of the model using a Sharpie® ultra fine point marker, as shown in Figure 3-9. The rows and columns are labeled as R1-R5 and C1-C5 respectively.

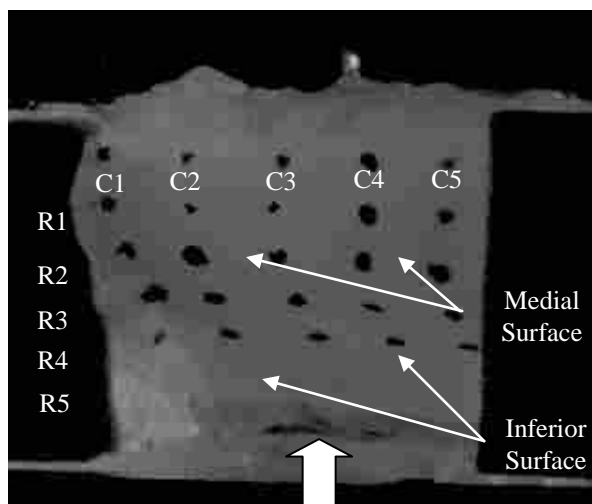


Figure 3-9: Right view of the medial and inferior surfaces of the synthetic vocal fold model. Applied dots were for point tracking purposes. Columns are labeled from left to right as C1-C5; rows are labeled from top to bottom as R1-R5.

3.2.3 Experimental Procedure

For the full larynx experiments, three models with 10% bowing and three models with 20% bowing were each paired with a separate normal model. Each model pair was brought to its onset pressure five times and the mean determined. Each model was then vibrated at 110% and 120% of its mean onset pressure, and frequency, flow rate, and high speed image data were

taken. Uncertainty estimates for each measurement are listed in Table 3-3 and details given in Appendix C.

Table 3-3: Uncertainty estimate in each measurement.

Metric	Uncertainty	Units
Open Quotient	±0.047	Unitless
Subglottal Pressure	±34.5	Pa
Onset Pressure	±63.9	Pa
Glottal Flow Rate	±42.5	ml/s
Acoustic Frequency	±0.2	Hz
Trajectories	±0.28	mm

After the above pre-injection data had been acquired, the bowed models were injected with various amounts of silicone to achieve various amounts of glottal closure: “sufficient” (just enough to close the glottal gap), “insufficient” (not enough to close the glottal gap), and “excess” (more than enough to close the glottal gap). For the sufficient injections, material was injected until the entire glottal gap appeared, when viewed from above, to be closed. For the insufficient injections, material was injected until the gap between the normal and bowed medial surfaces began to close. For the excess injections, material was first injected until the glottal gap was closed, immediately followed by injection of additional material until the medial surface of the bowed model was convex and compressed against the normal model (see Figure 3-10). The average and standard deviation of the injected material quantities for each injection location are listed in Table 3-4.

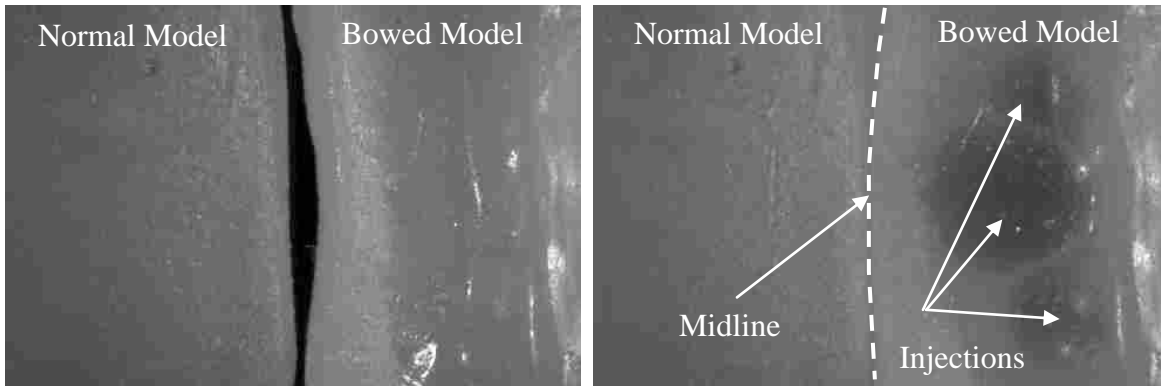


Figure 3-10: Superior view of normal (left) and bowed (right) paired models pre-injection (left image) and post-injection (right image). Dark circles are injections.

Table 3-4: Average injection amounts for both symmetric and hemilarynx experiments. Standard deviation is shown in parentheses.

Bowing Case	Injection Case	Far Left	Left	Center	Right	Far Right
10%	Sufficient	0	63.6 (15.28)	96.7 (5.77)	50 (10.2)	0
	Insufficient	0	0	60 (17.32)	0	0
	Excess	0	150 (11.2)	140 (14.14)	95 (77.8)	0
20%	Sufficient	0	100 (42.4)	230 (141)	100 (14.1)	0
	Insufficient	0	50 (10.3)	110 (36.1)	0	0
	Excess	0	115 (21.2)	316 (28.9)	120 (30.0)	0

After injection, the mounting plate assembly was removed from the test setup so that tests using other models could be performed while the injected silicone cured. Curing time was approximately 1.5 hours. After curing and remounting on the test setup, the same measurements that had been performed pre-injection were repeated.

The process described above was repeated three times to have three specimens of both 10% and 20% bowing for each injection case. A similar process was used for the hemilarynx case, with the exceptions that the bowed models were paired with a clear plate and only one experiment was performed (sample size of 1 for each injection case).

3.3 Results and Discussion

Onset Pressure (see Figure 3-11) shows the mean and standard deviation (error bars) of the onset pressures for all symmetric experiments. For the 10% excess and 20% sufficient injection cases there were only two data sets because the augmentation injection migrated to the lamina propria layer destroying the models. 12 of the 16 injection cases showed a decrease in the pre- and post-injection onset pressure. In all cases where the onset pressure increased post-injection, the injection location was in a more superior location in the model. The effect of the augmentation injections was more pronounced in the 20% bowing case than the 10% bowing case because more injection material was required in order to mitigate the effect of bowing.

It has been shown that synthetic vocal fold models are sensitive to both changes in model geometry and material properties of the individual layers (Pickup and Thomson, 2011; Zhang et al., 2009). As the injections were placed in the model, both geometry and material properties were changed having the potential to induce large changes in the flow-induced response. Qualitative observations were made of the model pre- and post-injection to determine which factors influenced the flow-induced response. The flow-induced response of the model can be attributed to various changes in the model based on the location and quantity of the injected amount (in estimated order of magnitude): pre-vibratory intraglottal angle, changes in the inferior entrance angle, thickness of the lamina propria, and induced stresses in the lamina propria.

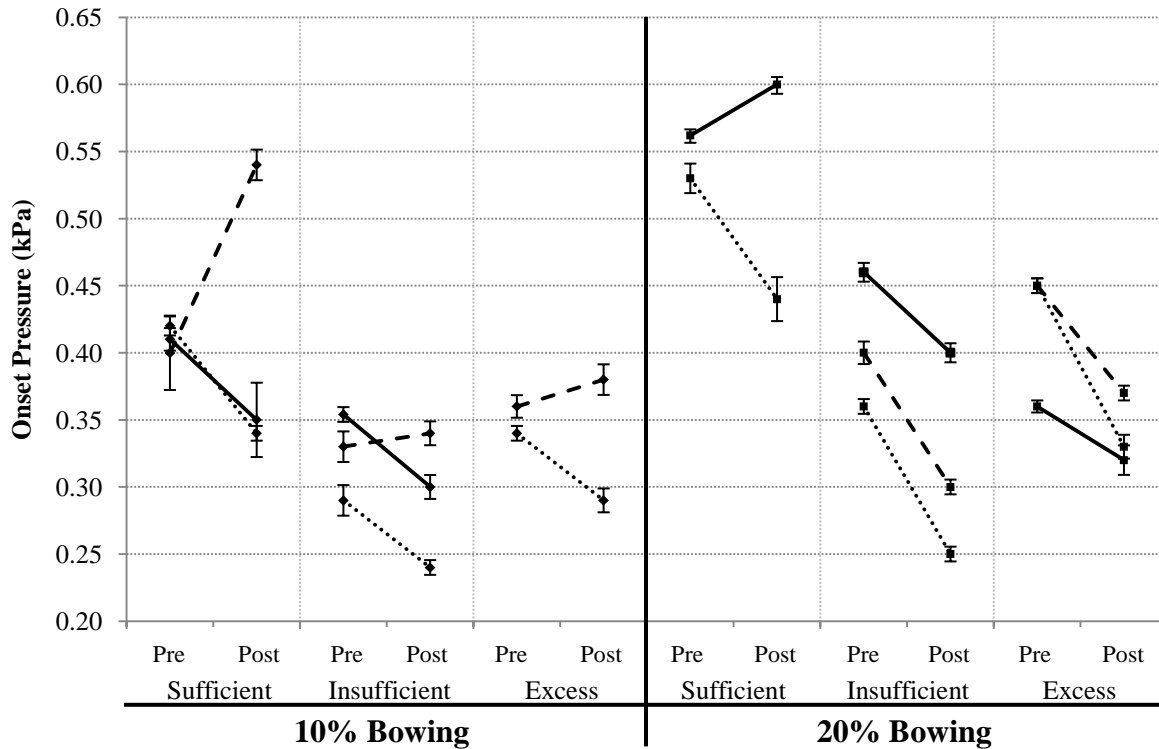


Figure 3-11: Pre- and post-injection onset pressures for the 10% (left section, ♦ markers) and 20% (right section, ■ markers) bowing cases. Solid, dashed, and dotted lines are experiments one, two, and three respectively. Left and right markers in each column are pre- and post-injection data, respectively. Error bars designate one standard deviation.

3.3.1 Vibration Frequency

The injections increased the average frequency of the models in 14 of the 16 cases, as can be seen in Figure 3-12. There was a general increase in frequency which could be attributed to the additional injected material effectively increasing the body and cover stiffness which in turn increased the natural frequency of the model. The two cases which exhibited a decrease in vibration frequency with injected material had the injections located in the most inferior location.

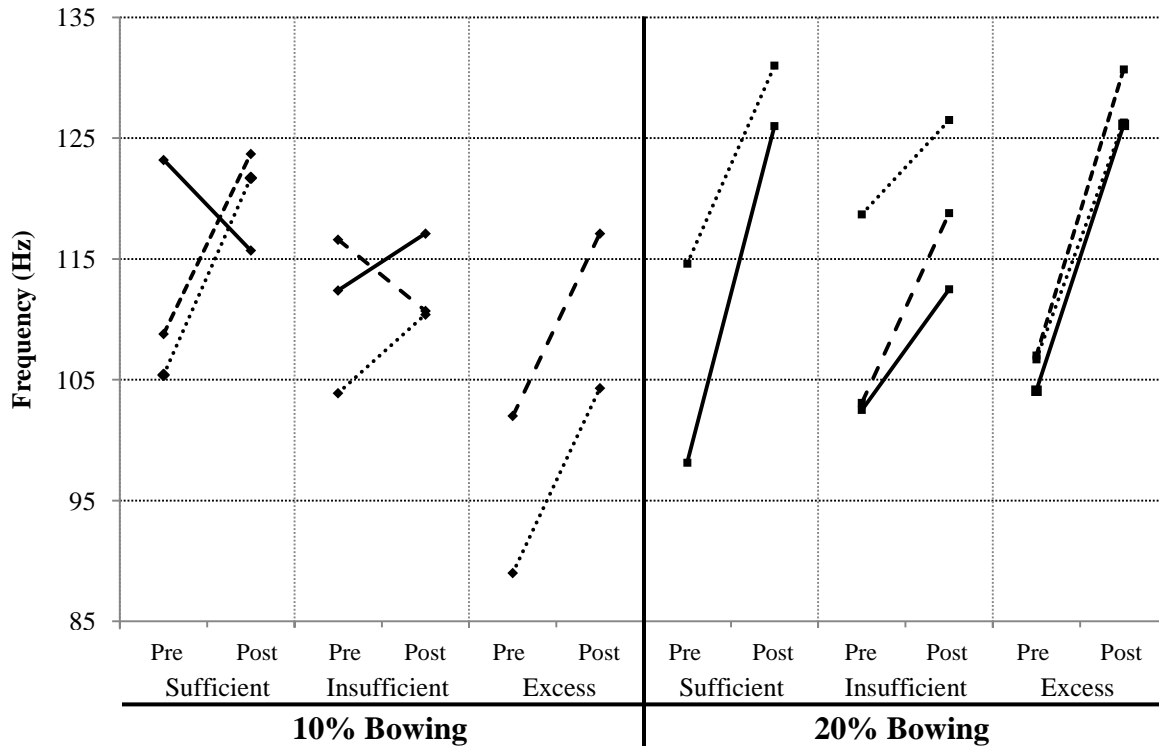


Figure 3-12: Pre- and post-injection vibration frequencies for the 10% (left section, ◆ markers) and 20% (right section, ■ markers) bowing cases. Solid, dashed, and dotted lines are experiments one, two, and three respectively. Left and right markers in each column are pre- and post-injection data, respectively.

3.3.2 Glottal Flow Rate

The flow rate generally decreased between pre- and post-injection as shown in Figure 3-13. This change was due to the reduction of glottal area and vibration amplitude caused by the injections. The most significant reduction in flow rate was seen in the 20% bowed model. The injection case that did not show a decrease in glottal flow rate was due to an insufficient amount of injected material to close the glottal gap.

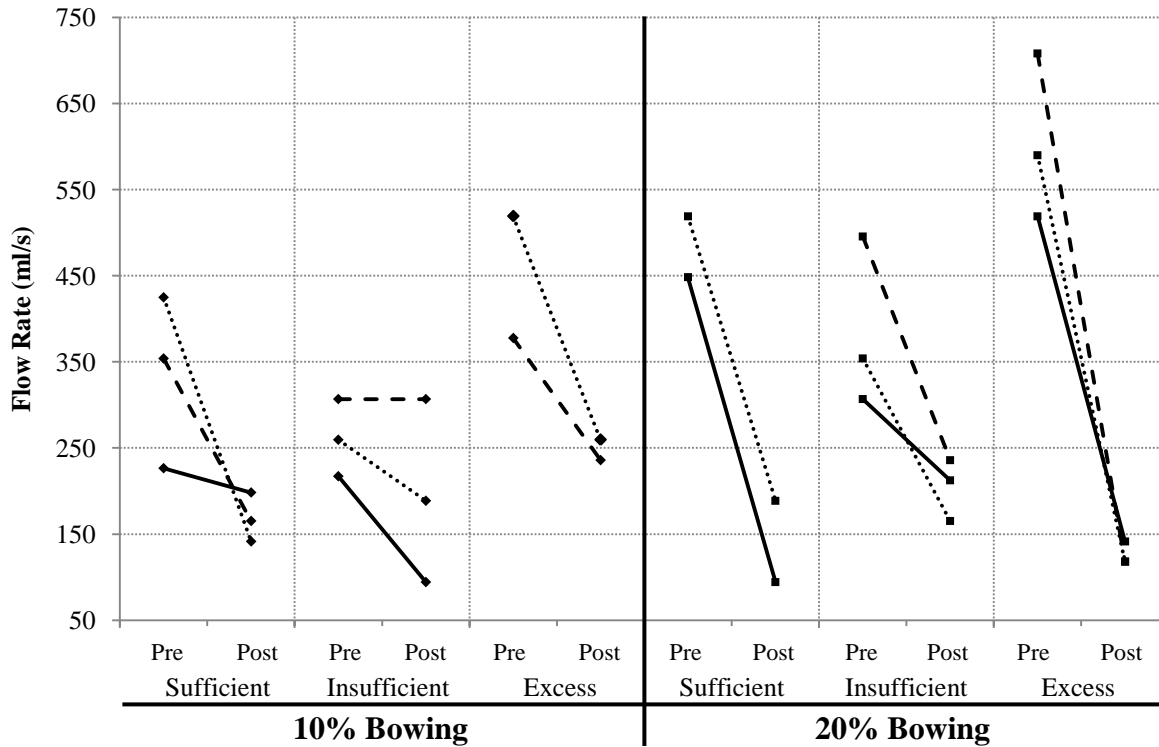


Figure 3-13: Pre- and post-injection flow rates for the 10% (left section, ◆ markers) and 20% (right section, ■ markers) bowing cases. Solid, dashed, and dotted lines are experiments one, two, and three respectively. Left and right markers in each column are pre- and post-injection data, respectively.

3.3.3 Open Quotient

The average open quotient for all models was approximately one before injections were placed (see Figure 3-14) showing there was little to no glottal closure. However, after the injections were placed, the amount of glottal closure was similar to values found during phonation of true vocal folds (Baken and Orlikoff, 2000). Three of the insufficient injection cases did not show any improvement in open quotient because the injections never closed the glottal gap. The greatest difference pre- and post-injection was found in the 20% bowing case with excess injections.

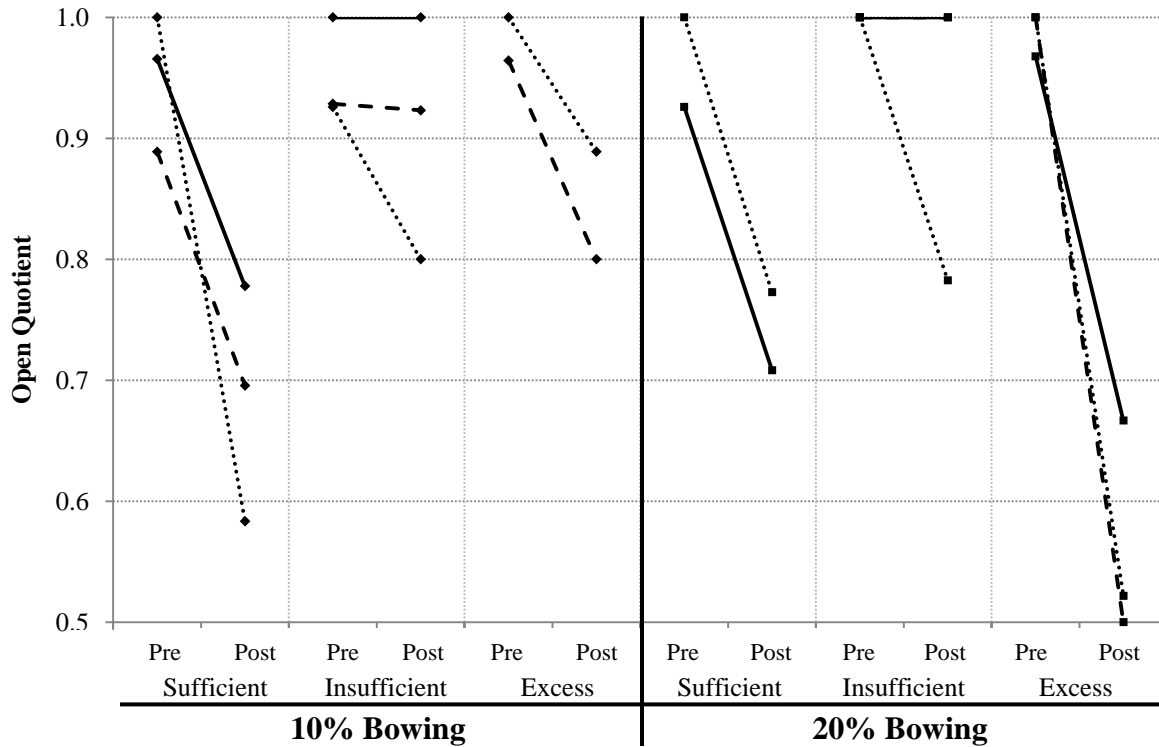
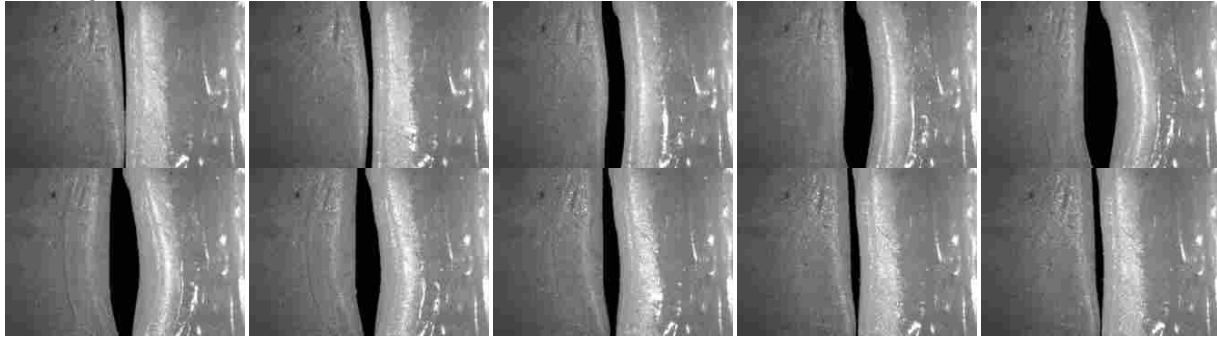


Figure 3-14: Pre- and post-injection open quotients for the 10% (left section, \blacklozenge markers) and 20% (right section, \blacksquare markers) bowing cases. Solid, dashed, and dotted lines are experiments one, two, and three respectively. Left and right markers in each column are pre- and post-injection data, respectively.

3.3.4 Superior Surface Imaging

Figure 3-15 shows superior surface images for one period of oscillation, pre- and post-injection, for the 20% bowed, excess injection case vibrating at 120% onset pressure. In each figure the left and right vocal fold models are normal and bowed, respectively. Before injection there was incomplete glottal closure and asymmetry in the vibration pattern. After injection glottal closure was achieved. However, the vibration pattern remained asymmetric, with the normal model having the greater amplitude. This was possibly caused by the injection increasing the model stiffness in the cover region – even though the injection was confined to the body layer – perhaps due to the injection-induced displacement increasing tension in the cover layer.

Pre-Injection ($P_{\text{sub}} = 0.43$ kPa)



Post-Injection ($P_{\text{sub}} = 0.38$ kPa)

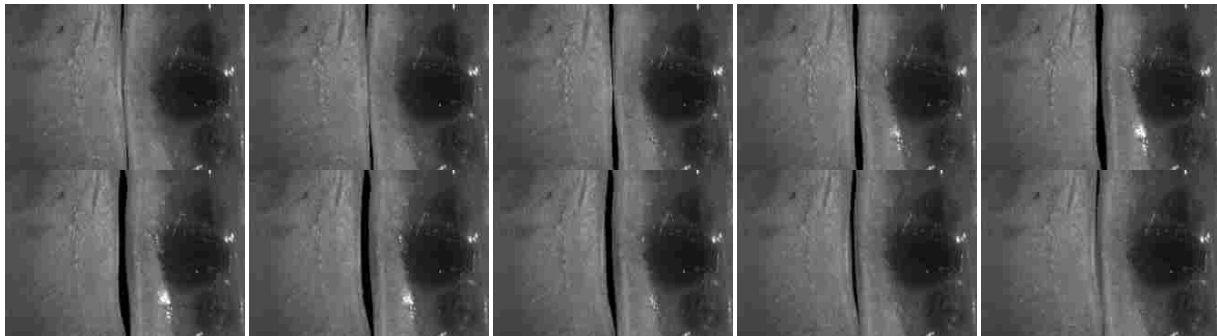
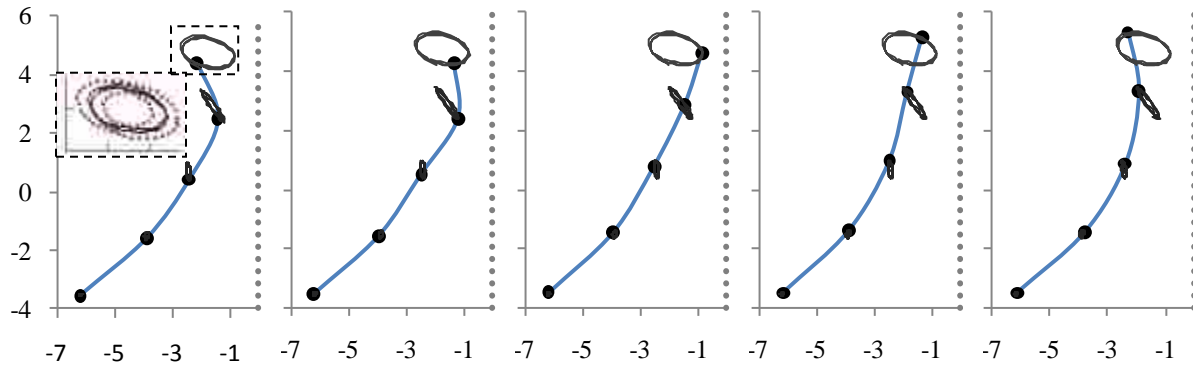


Figure 3-15: Timeline of one cycle of oscillation pre- and post-injection. Model is the 20% bowed, excess injection case.

3.3.5 Medial Surface Tracking

The hemilarynx setup was used to investigate the effect of injections on the medial surface motion, including marker trajectories, vertically-propagating wave speed, and intraglottal profile phase angle. Figure 3-16 shows the trajectory of the points on column C3 (refer to Figure 3-9) through one period of oscillation, pre- and post-injection, for the 20% bowed, excess injection case vibrating at 110% of onset pressure. For reference, the subplots in the first frame of each case show the associated uncertainty envelope for one marker (see Appendix C). It can be seen that even though the model was bowed, there was still a convergent/divergent profile of the medial surface during vibration. However, the trajectories showed the glottis was open

Pre-Injection ($P_{\text{sub}} = 0.66 \text{ kPa}$)



Post-Injection ($P_{\text{sub}} = 0.63 \text{ kPa}$)

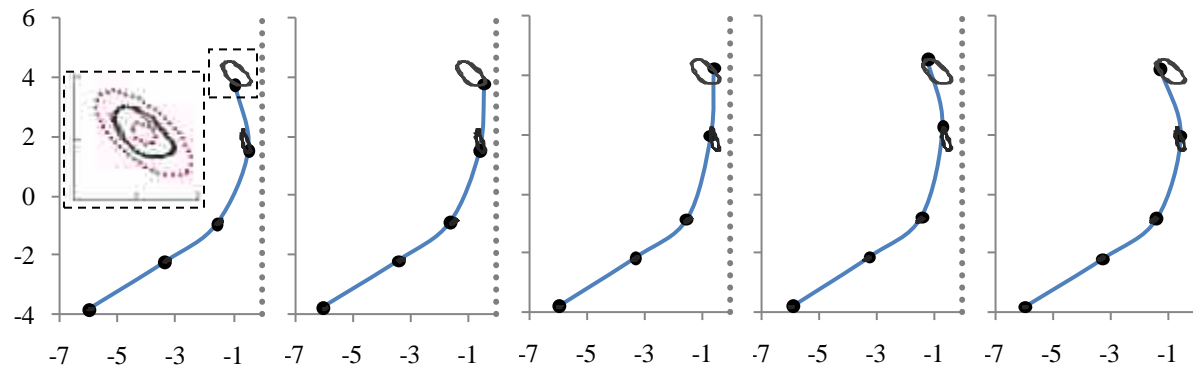


Figure 3-16: Pre- (top) and post- (bottom) injection trajectories of the points in column C3 through one period of vibration. The dotted line represents the location of the clear acrylic plate. Flow is from bottom to top. The sub-figure shows the uncertainty associated with point selection determination. Units are mm.

during the entire oscillation cycle. The post-injection trajectories showed bulging of the inferior surface due to the location of the injection. A convergent/divergent profile of the medial surface was also present but lessened.

Column C3 was used to monitor changes caused by the injections on wave velocity and phase difference. Figure 3-17 shows that the injections decreased the wave velocity and increased the phase angle by an average of 0.5 mm/s and 12 °/mm, respectively. The experimental results for both pre- and post-injection wave velocity and phase delay were comparable to the wave velocity (0.5 m/s – 2.2 m/s) and phase delay (27 °/mm – 61 °/mm) values reported by Titze et al., (1993).

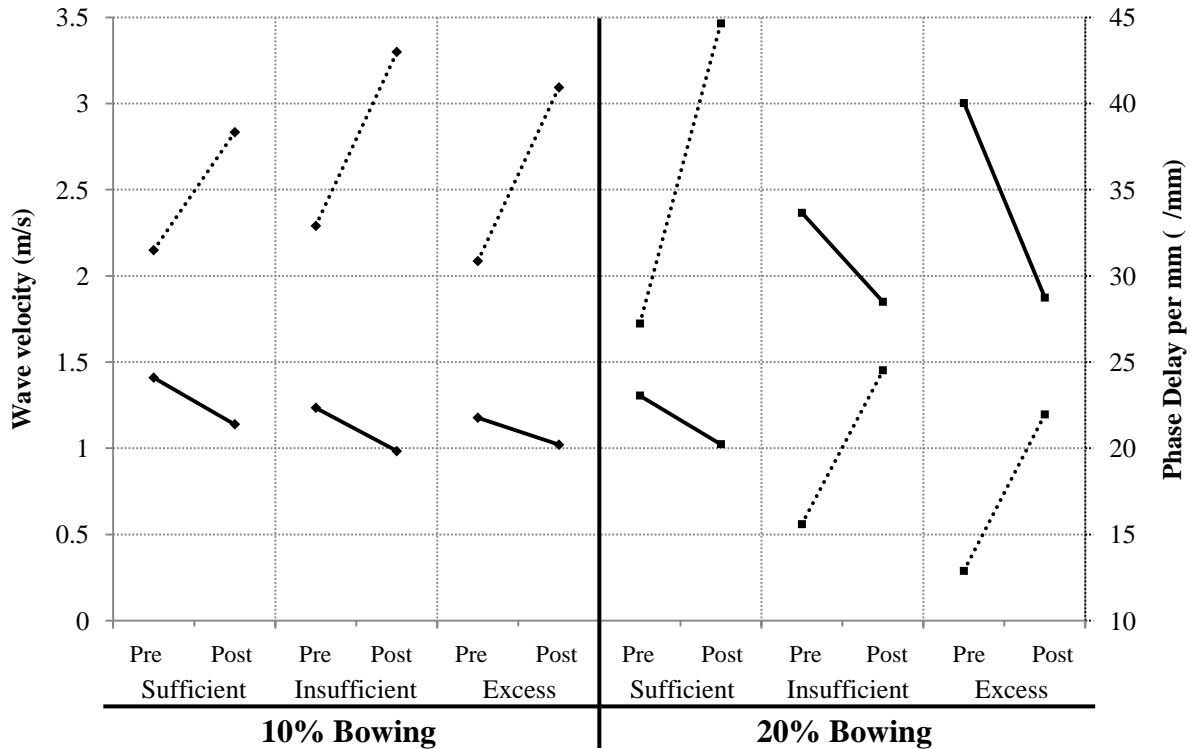


Figure 3-17: Pre- and post-injection wave velocities (solid lines) and phase delay per mm (dashed lines) of column three (C3) for the 10% (left section, \blacklozenge markers) and 20% (right right, \blacksquare markers) bowing cases. Left and right markers in each column are pre- and post-injection data, respectively.

3.4 Conclusions

A synthetic, self-oscillating vocal fold model was created which simulated vocal fold bowing by reducing the volume of the body layer from that of a normal model. Changes made to the ligament, superficial lamina propria, and epithelium layers followed the changes made to the body portion to reflect the volume reduction of the body layer (i.e., their relative dimensions were the same for the bowed and unbowed models). To explore the influence of injections on bowed model response, three different amounts of injections were placed in models with 10% and 20% bowing: sufficient to close the glottal gap, insufficient to close the glottal gap, and excess injection to cause convexity of the bowed model. The model showed a general pre- to

post-injection decrease in onset pressure, glottal flow rate, and open quotient, while a corresponding increase in vibration frequency was observed.

The hemilarynx experiments showed a general decrease in wave velocity and increase in phase delay. It has been shown that a decrease in mucosal wave velocity relates to a decrease in phonation effort in human vocal folds (Verdolini-Marston and Titze, 1990; Titze, 1991). From these results, it can be deduced that the injections decreased the “effort” required to vibrate the models, thus correcting for the adverse consequences of the pre-injection bowing.

The model was successfully altered to exhibit various degrees of bowing which were then mitigated by injecting material. This showed that procedures used to alleviate pathologies of the human vocal fold can be roughly approximated using synthetic models. However, the model and procedures were idealizations only. Because of this, the results are preliminary and further excised larynx and/or clinical studies should be performed in order to obtain a complete understanding of the effects of augmentation injections on human vocal fold vibration. Nevertheless, the present methodology may be used in future studies aimed at exploring isolated physical phenomena associated with augmentation, and perhaps other phonosurgical, procedures.

The newly developed model can be extended in order to evaluate research areas outside of the scope of this work including quantifying the effect of other simulated pathologies such as sulcus vocalis, cysts, changes in material properties due to aging, and the effect of medialization laryngoscopy compared to augmentation injections. Additionally, physical phenomena that were not evaluated in this research that the model could be used to study are the effect of the bowing and augmentation injections on subglottal and supraglottal flow, flow resistance, and vocal efficiency.

4 CONCLUSION

A complete understanding of the vibratory characteristics of the human vocal folds is vital in assessing and alleviating voice disorders. To this end, the work in this thesis was completed which investigated the medial surface dynamics of four unique synthetic self-oscillating models. Additionally, a newly developed four-layer synthetic model was altered to quantify the effects of augmentation injections on synthetic vocal folds.

4.1 Medial Surface Tracking and Dynamic Characteristic of Synthetic, Self-Oscillating Vocal Fold Models (Chapter 2)

4.1.1 Conclusions

Four models were evaluated by measuring onset pressure, frequency, maximum glottal width, flow rate, and medial surface motion and comparing the results to previously published experiments on excised human larynges. For each metric, the results were as follows:

1. The EPI model had the lowest onset pressure, smallest maximum glottal width, and lowest flow rate.
2. The motion of the medial surface of the EPI model (displacement and velocity) best matched published data from hemilarynx experiments.

The ability of the EPI model to approximate the vibratory characteristics was believed to be due to the incorporation of a convergent profile and a rounded entrance angle, as well as an extremely soft cover, additional layers, and introduction of a fiber in the ligament layer.

Although there are advantages to the EPI model, it has limitations. It is more difficult to fabricate because of the added layers and incorporation of a soft cover layer. The cover layer is somewhat delicate. Finally, the model still incorporates idealized geometry and is isotropic in the individual layers of silicone.

4.1.2 Future Work

In this study tension was either absent or present, it would be illuminating to study the effect of adding various degrees of tension on the vibratory response. Also, other than the fiber in the ligament of the EPI model, all material properties were isotropic. A development of more realistic materials would aid in creating more accurate vocal fold models.

4.2 Effect of Augmentation Injection on Bowed Self-Oscillating Synthetic Vocal Fold Models (Chapter 3)

4.2.1 Conclusions

A synthetic self-oscillating model was created which simulated vocal fold bowing by reducing the volume of the body layer. Changes made to the ligament, superficial lamina propria, or epithelium layers followed the changes made to the body portion to reflect the volume reduction of the body layer. To explore the influence of injections on bowed model response, three different amounts of injections were placed in models with 10% and 20% bowing: sufficient to close the glottal gap, insufficient to close the glottal gap, and excess injection to

cause convexity of the bowed model. The model showed a general decrease in onset pressure, glottal flow rate, and open quotient while an increase in vibration frequency was observed.

The hemilarynx experiment showed a general decrease in wave velocity and increase in phase angle. It has been shown that a decrease in mucosal wave velocity relates to a decrease in phonation effort in human vocal folds (Verdolini-Marston and Titze, 1990; Titze, 1991). From these results, it can be deduced that the injections decreased the “effort” required to vibrate and thus mitigated the effect of the bowing on the model’s response.

4.2.2 Future Work

It should be stressed that this study attempted to investigate the physics of implanting material into a synthetic bowed vocal fold model. The results of this study are applicable only to the synthetic model which was a simplified representation of the human vocal fold. Because of this, correlations between the model and human vocal folds cannot be made. Further studies with excised larynges or clinical studies should be performed in order to obtain a complete understanding of the effects of augmentation injections on vocal fold vibration.

REFERENCES

- Abdel-Aziz, Y. I., & Karara, H. M. (1971). Direct linear transformation from comparator coordinates into object space coordinates in close-range photogrammetry. *Proceedings of the Symposium on Close-range Photogrammetry*, (pp. 1-18). Falls Church, Va.
- Baken, R. J., & Orlikoff, R. F. (2000). *Clinical Measurement of Speech and Voice* (2 ed.). San Diego, CA: Singular Publishing Group.
- Baker, K. K., Ramig, L. O., Sapir, S., Luschei, E. S., & Smith, M. E. (2001). Control of vocal loudness in young and old adults. *Journal of Speech, Language & Hearing Research* , 44, 297-305.
- Becker, S., Kniesburges, S., Muller, S., Delgado, A., Link, G., Kaltenbacher, M., et al. (2009). Flow-structure-acoustic interactions in a human voice model. *Journal of the Acoustical Society of America* , 125 (3), 1351-1361.
- Berry, D. A., Montequin, D. W., & Tayama, N. (2001). High-speed digital imaging of the medial surface of the vocal folds. *Journal of the Acoustical Society of America* , 110 (5), 2539-2547.
- Berry, D. A., Zhang, Z., & Neubauer, J. (2006). Mechanisms of irregular vibration in a physical model of the vocal folds. *Journal of the Acoustical Society of America* , 120 (3).
- Bless, D., Hirano, M., & R, F. (1987). Videostroboscopic evaluation of the larynx. *Ear Nose and Throat Journal* , 66, 289-296.
- Boessenecker, A., Berry, D. A., Lohscheller, J., & Eysholdt, U. D. (2007). Mucosal wave properties of a human vocal fold. *Acta Acustica with Acustica* , 93, 815-823.
- Caton, T., Thibeault, S. L., Klemuk, S., & Smith, M. E. (2007). Viscosity of hyaluronan and nonhyaluronan based vocal fold injectables: Implications for mucosal versus muscle use. *Laryngoscope* , 117, 516-521.
- Chan, R. W., & Rodriguez, M. L. (2008). A simple-shear rheometer for linear viscoelastic characterization of vocal fold tissues at phonatory frequencies. *Journal of the Acoustical Society of America* , 124, 1207-1219.
- Chan, R. W., & Titze, I. R. (2006). Dependence of phonation threshold pressure on vocal tract acoustics. *Journal of the Acoustical Society of America* , 119 (4), 2351-2362.
- Chan, R. W., & Titze, I. R. (1999). Viscoelastic shear properties of human vocal fold mucosa: Measurement methodology and empirical results. *Journal of the Acoustical Society of America*, 106 (4), 2008-2021.
- Chan, R. W., Fu, M., Young, L., & Tirunagari, N. (2007). Relative contributions of collagen and elastin to elasticity of the vocal fold under tension. *Annals of biomedical engineering* , 35 (8), 1471-1483.

- Chan, R. W., Titze, I. R., & Titze, M. R. (1997). Further studies of phonation threshold pressure in a physical model of the vocal fold mucosa. *Journal of the Acoustical Society of America* , 101 (6), 3722-3727.
- Chisari, N. E., Artana, G., & Sciamarella, D. (2010). Vortex dipolar structures in a rigid model of the larynx at flow onset. *Experiments in Fluids* , In Press.
- Decker, G. Z., & Thomson, S. L. (2005). Computational simulations of vocal fold vibration: Bernoulli versus navier-stokes. *Journal of Voice* , 21 (3), 273-284.
- Deverge, M., Pelorson, X., Vilain, C., & Lagree, P. Y. (2003). Influence of collision on the flow through in-vitro rigid models of the vocal folds. *Journal of the Acoustical Society of America* , 114 (6), 3354-3362.
- Doellinger, M., & Berry, D. A. (2006). Computation of the three-dimensional medial surface dynamics of the vocal folds. *Journal of Biomechanics* , 39, 369-374.
- Doellinger, M., & Berry, D. A. (2006). Visualization and quantification of the medial surface dynamics of an excised human vocal fold during phonation. *Journal of Voice* , 20 (3), 401-413.
- Doellinger, M., Berry, D. A., & Berke, G. S. (2005). Medial surface dynamics of an in vivo canine vocal fold during phonation. *Journal of the Acoustical Society of America* , 117 (5), 3174-3183.
- Drechsel, J. S., & Thomson, S. L. (2008). Influence of supraglottal structures on the glottal jet exiting a two-layer synthetic, self-oscillating vocal fold model. *Journal of the Acoustical Society of America* , 123 (6), 4434-4445.
- Erath, B. D., & Plesniak, M. W. (2006). An investigation of bimodal jet trajectory in flow through scaled models of the human vocal tract. *Experiments in Fluids* , 40, 683-696.
- Erath, B. D., & Plesniak, M. W. (2006). An investigation of jet trajectory in flow through scaled vocal fold models with asymmetric glottal passages. *Experiments in Fluids* , 41, 735-748.
- Fulcher, L. P., Scherer, R. C., Witt, K. J., Thapa, P., Bo, Y., & Kucinski, B. R. (2010). Pressure distributions in a static physical model of the hemilarynx: Measurements and Computations. *Journal of Voice* , 24 (1), 5-20.
- Fulcher, L. P., Scherer, R. C., Zhai, G., & Zhu, Z. (2006). Analytic representation of volume flow as a function of geometry and pressure in a static physical model of the glottis. *Journal of Voice* , 20 (4), 489-512.
- George, R. B. (2011). Design and analysis of a flapping wing mechanism for optimization. Master's thesis, Brigham Young University, Provo, UT.
- Gray, S. D., Bielamowicz, S. A., Titze, I. R., Dove, H., & Ludlow, C. (1999). Experimental approaches to vocal fold alteration: Introduction to the minithyrotomy. *Annals of Otolaryngology, Rhinology and Laryngology* , 108 (1), 1-9.
- Hanson, D. G., Gerratt, B. R., & Ward, P. H. (1983). Glottographic measurement of vocal dysfunction. A preliminary report. *Ann Otol Rhinol Laryngol* (92), 413-420.
- Hirano, M., & Kakita, Y. (1985). Cover body theory of vocal fold vibration. In R. G. Daniloff (Ed.), *Speech Science* (pp. 1-46). San Diego, CA: College-Hill Press.

- Isshiki. (1989). *Phonosurgery: theory and practice*. Tokyo Berlin Heidelberg New York: Springer.
- Kendall, K. (2007). Presbyphonia: a review. *Current Opinion on Otolaryngology and Head and Neck Surgery* , 15, 137-140.
- Kniesburges, D., Thomson, S. L., Barney, A., Triep, M., Sidlof, P., Horacek, J., et al. (In press). In vitro experimental investigation of voice production. *Current Bioinformatics* .
- Krane, M. H., Barry, M., & Wei, T. (2010). Dynamics of temporal variations in phonatory flow. *Journal of the Acoustical Society of America* , 128 (1), 372-383.
- Krane, M., Barry, M., & Wei, T. (2007). Unsteady behavior of flow in a scaled-up vocal folds model. *Journal of the Acoustical Society of America* , 122 (6), 3659-3670.
- Misun, V., Svancara, P., & Vasek, M. (2011). Experimental analysis of the characteristics of artificial vocal folds. *Journal of Voice* , 25 (3), 308-318.
- Mongeau, L., Francheck, N., Coker, C. H., & Kubi, R. A. (1997). Characteristics of a pulsating jet through a small modulated orifice, with application to voice production. *Journal of the Acoustical Society of America* , 102 (2), 1121-1133.
- Munson, B. R., Young, D. F., & Okiishi, T. H. (2006). *Fundamentals of fluid mechanics* (5 ed.). Jefferson City: John Wiley & Sons.
- Murray, P. R., & Thomson, S. L. (In Press). Synthetic, multi-layer, self-oscillating vocal fold model fabrication. *Journal of Visualized Experiments* .
- Neubauer, J., Zhang, Z., Miraghaio, R., & Berry, D. A. (2007). Coherent structures of the near field flow in a self-oscillating physical model of the vocal folds. *Journal of the Acoustical Society of America* , 121 (2), 1102-1118.
- NIDCD. (2010, June). *National Institute on Deafness and Other Communication Disorders*. Retrieved June 10, 2011, from <http://www.nidcd.nih.gov/>.
- Paniello, R. C., Sulica, L., Khosla, S. M., & Smith, M. E. (2008). Clinical experience with Gray's minithyrotomy procedure. *Annals of Otolaryngology, Rhinology, and Laryngology* , 117 (6), 437-442.
- Pickup, B. A., & Thomson, S. L. (2010). Flow-induced vibratory response of idealized versus magnetic resonance imaging-based synthetic vocal fold models. *Journal of the Acoustical Society of America* , 128 (3).
- Pickup, B. A., & Thomson, S. L. (2009). Influence of asymmetric stiffness on the structural and aerodynamic response of synthetic vocal fold models. *Journal of Biomechanics* , 42, 2219-2225.
- Popolo, P. S., & Titze, I. R. (2008). Qualification of a quantitative laryngeal imaging system using videostroboscopy and videokymography. *Annals of Otolaryngology, Rhinology & Laryngology* , 117 (6), 4014-412.
- Riede, T., Tokuda, I. T., Munger, J. B., & Thomson, S. L. (2008). Mammalian laryngeal air sacs add variability to the vocal tract impedance: Physical and computational modeling. *Journal of the Acoustical Society of America* , 124 (1), 634-647.
- Scherer, R., Shinwari, D., De Witt, K., Zhang, C., Kucinschi, B., & Afjeh, A. (2001). Intraglottal pressure profiles for a symmetric and oblique glottis with a divergence angle of 10 degrees. *Journal of the Acoustical Society of America* , 109, 1616-1630.

- Spencer, M., Siegmund, T., & Mongeau, L. (2008). Determination of superior surface strains and stresses, and vocal fold contact pressure in a synthetic larynx model using digital image correlation. *Journal of the Acoustical Society of America* , 123 (2), 1089-1103.
- Svec, J. G., & Schutte, H. (1996). Videokymography: High-speed line scanning of vocal fold vibration. *Journal of Voice* , 10 (2), 201-205.
- Svecm J. G., Sram, J., & Schutte, H. (2007). Videokymography: What to look for?. *Annals of Otolaryngology, Rhinology & Laryngology*, 116(3), 172-180.
- Thomson, S. (2004). Fluid-structure interactions within the human larynx, Ph.D. dissertation. West Lafayette, Indiana.
- Thomson, S. L., Mongeau, L., & Frankel, S. H. (2005). Aerodynamic transfer of energy to the vocal folds. *Journal of the Acoustical Society of America* , 118, 1689-1700.
- Titze, I. R. (1991). Phonation threshold pressure: a missing link in glottal aerodynamics. *Journal of the Acoustical Society of America* , 91, 2926-2935.
- Titze, I. R. (2000). *Principles of voice production* (2 ed.). National Center for Voice and Speech.
- Titze, I. R. (2006). *The myoelastic aerodynamic theory of phonation* (1 ed.). National Center for Voice and Speech.
- Titze, I. R. (1988). The physics of small-amplitude oscillation of the vocal folds. *Journal of the Acoustical Society of America* , 83, 1536-1552.
- Titze, I. R., Jiang, J. J., & Hsiao, T.-Y. (1993). Measurement of mucosal wave propagation and vertical phase difference in vocal fold vibration. *Annals of Otolaryngology and Laryngology* , 102, 58-63.
- Titze, I. R., Schmidt, S. S., & Titze, M. R. (1995). Phonation threshold pressure in a physical model of the vocal fold mucosa. *Journal of the Acoustical Society of America* , 97 (5), 3080-3084.
- Triep, M., Brucker, C., & Schroder, W. (2005). High-speed PIV measurements of the flow downstream of a dynamic mechanical model of the human vocal folds. *Experiments in Fluids* , 39 (2), 232-245.
- Tropea, C., Yarin, A. L., & Foss, J. F. (Eds.). (2007). *Springer handbook of experimental fluid mechanics*. Wurzburg, Germany: Sturtz GmbH.
- Verdolini-Marston, K., & Titze, I. R. (1990). Changes in phonation threshold pressure with injected conditions of hydration. *Journal of Voice* , 4, 142-151.
- Zhang, Z., Neubauer, J., & Berry, D. A. (2009). Influence of vocal fold stiffness and acoustic loading on flow-induced vibration of a single-layer vocal fold model. *Journal of Sound and Vibrations*. 322, 299-313.

APPENDIX A. MODEL FABRICATION

The fabrication sequence (see Figure A-1) consists of making molds for vocal fold model layers, sequentially casting silicone layers, and mounting the models for testing. The model has four distinct layers: body, ligament, superficial lamina propria, and epithelium, in addition to a single fiber. A backing layer is added to facilitate the accurate placement of individual layers to the vocal fold model. The model geometric parameter definitions are shown in Figure A-2, with parameter values for the current model given in Table A-1. In the following sections, different silicone mixing ratios are specified for the different layers; these produce material properties that are similar to those reported for human vocal fold tissue in the small strain regime¹³ (see Table A-2).

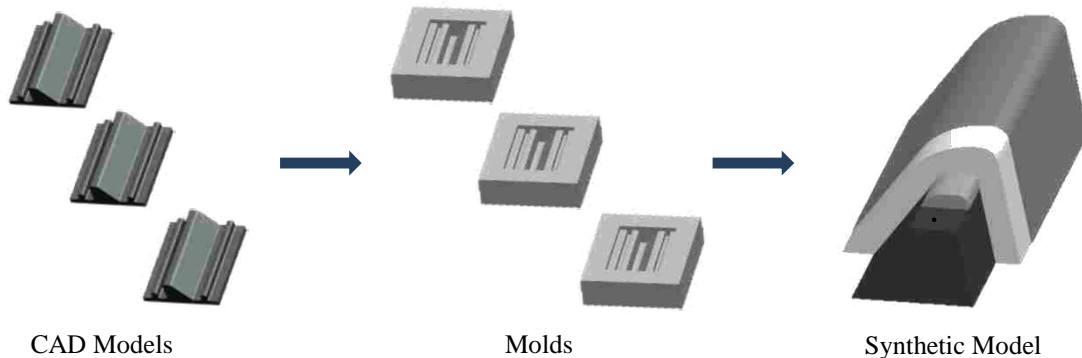


Figure A-1: Synthetic vocal fold model fabrication process. CAD-derived solid models (left panel) are used to create molds (center panel) for each layer. Each layer is then cast, beginning with the body layer and ending with the epithelium layer (right panel, with each layer “peeled back” for visibility). After fabrication, models are mounted to acrylic plates for testing.

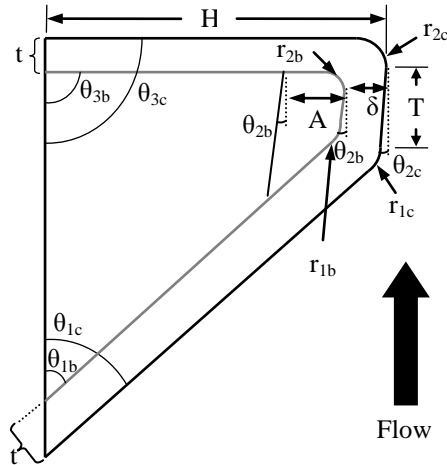


Figure A-2: Synthetic vocal fold model cross section. Distinct body, superficial lamina propria, ligament, and epithelium layers are shown. Parameters define vocal fold model geometry. This figure is scaled for clear representation of geometric definitions. Application of the parameter values given in Table A-1 will result in a slightly different shape than what is shown here.

Table A-1: Geometric parameters and description used to define model.

Parameter	Value	Description
$\theta_{1b,c}$	50°	Inferior glottal angle
$\theta_{2b,c}$	5°	Intraglottal angle
$\theta_{3b,c}$	90°	Superior glottal angle
r_{1c}	6.0 mm	Cover entrance radius
r_{2c}	0.987 mm	Cover exit radius
r_{1b}	2.0 mm	Ligament entrance radius
r_{2b}	0.513 mm	Ligament exit radius
T	0.1 mm	Vertical glottal thickness
t	1.6 mm	Inferior and superior cover layer thickness
δ	2.0 mm	Maximum medial cover layer thickness
D	8.4 mm	Lateral depth
A	1 mm	Ligament layer thickness

Table A-2: Mixture ratios by weight and resulting Young's modulus of the individual sections of the vocal fold model. EF and DS designate silicone made from Ecoflex® and Dragon Skin®, respectively¹⁴.

Model Section	Mixing Ratio	Young's Modulus (kPa)
Body	EF 1:1:1	11.8
Ligament	EF 1:1:4	1.6
SLP	EF 1:1:8	0.2
Epithelium	DS 1:1:1	49.8

A.1) Mold Fabrication and Preparation

1.1) Create solid models of three vocal fold layers: superficial lamina propria, ligament, and body layers. This is typically done by creating 3D computer-aided design (CAD) models with the desired geometries, exporting the CAD models as stereolithography (STL) files, and sending the STL files to a custom machine shop for rapid prototyping.

1.2) Create a box-shaped mold form using thin pieces of acrylic material. Approximate dimensions (not critical) are 2.54 cm high \times 5.72 cm wide \times 6.35 cm deep. Make the bottom of the form by adhering it to a flat acrylic plate. Seal all interior edges with vacuum grease.

1.3) Place a small amount of vacuum grease on the lateral side of the solid model of desired geometry (i.e., the body, the ligament, or the superficial lamina propria). Press model into bottom of mold form cavity, vacuum grease side down, so that the vacuum grease holds the part in place. Liberally coat mold form and solid model with release agent. Using a paint brush, ensure release agent reaches into all corners of the mold form cavity.

1.4) Mix 10 parts A and one part B of Smooth-Sil 950 platinum silicone rubber (parts measured by weight) and pour into mold form cavity. To remove air bubbles place mold form with uncured silicone rubber in a vacuum chamber and reduce pressure (e.g., to around 23 inHg below atmospheric pressure) for approximately three minutes (or more or less as necessary). Remove from vacuum chamber and place on level surface. Allow to cure for 24 hours and remove mold from mold form.

1.5) Repeat steps 1.1 through 1.4 to create molds for each of the superficial lamina propria, ligament, and body layers.

1.6) Cut ligament layer mold at the center of the medial surface in the anterior-posterior direction with a straight razor to allow for fiber insertion.

A.2) Casting of Each Layer

1.7) *Body Layer:* Apply thin layer of release agent to body mold cavity with paint brush. Mix one part B and one part A of Ecoflex® 00-30 Supersoft Platinum Silicone (by weight). Add one part Silicone Thinner (by weight) to reduce the eventual cured stiffness of the material. Mix together for 30 seconds and place in vacuum chamber for one minute to remove entrapped air. Remove mixture from vacuum and pour into the body mold cavity, but do not fill to the top of the entire mold cavity. Place in oven at 250 °F for 30 minutes. Remove from oven and cool.

1.8) *Backing:* Mix one part B and one part A of Dragon Skin® and add one part Silicone Thinner (by weight). Mix vigorously for 30 seconds, place in vacuum for 1 minute, and pour into the body mold cavity until full. Place in oven at 250 °F for 30 minutes. Remove mold from oven and cool. Remove model from mold, allow to cool to room temperature, and remove any release agent on the surface of the body layer with paper towel.

1.9) *Ligament Layer:* Apply thin layer of release agent on ligament mold cavity surface with paint brush. Place a 30 cm thread in the mold by pushing it into the cut from the straight razor. Thoroughly mix one part B and one part A of Ecoflex® 00-30 and four parts of Silicone Thinner (by weight). Place in vacuum chamber to remove air bubbles and pour mixture into ligament mold cavity.

1.10) *Ligament Layer (continued):* Press body-backing model (from Steps 2.1.1 and 2.1.2) into the ligament mold cavity. Begin insertion at one side and gently move to the other so

that the model pushes the excess uncured silicone and air bubbles out of the mold cavity. If air bubbles are present, remove the model from the mold cavity, refill with uncured silicone, and repeat pressing model into the mold. Place mold in oven for 30 minutes, remove, and cool to room temperature. Remove model from mold. Remove excess release agent with paper towel.

1.11) *Superficial Lamina Propria Layer:* Apply thin layer of release agent on superficial lamina propria (SLP) mold cavity surface with paint brush. Mix one part B, one part A of Ecoflex® 00-30, and 8 parts Silicone Thinner by weight. Vacuum as done previously and pour into SLP mold cavity. Use the same process described in Step 2.1.4 to insert the ligament-body-backing model into the superficial lamina propria mold cavity. Place in an oven at 250 °F and cure for one hour. Remove from oven and allow to cool. Remove model slowly and with extreme care so that the superficial lamina propria remains intact.

1.12) *Epithelium Layer:* Place vocal fold model on a flat surface with the backing down. Remove support material with a straight razor. Suspend threads in air by attaching them to an object of greater height than the model. Mix one part B and one part A of Dragon Skin® with one part of Silicone Thinner, mix, vacuum, then pour over the model and allow to cure for one hour. Repeat the process to create a thicker layer. Remove excess material with a straight razor.

1.13) *Optional:* If each layer is desired to be a different color (for visible inspection of different layers), add dye to part B of either the Ecoflex® or Dragon Skin® during the mixing process.

1.14) *Optional:* If material property data will be collected, create tensile and rheological specimens simultaneously with fabrication of each model layer. Do this by pouring extra uncured material into release agent-treated molds of desired material property specimen shape and size.

1.15) *Optional:* If measurements of layer thickness are desired, cut a cross section of the model with a straight razor and inspect with microscope.

A.3) Final Model Preparation for Testing

1.16) Mount each completed vocal fold model into an acrylic mounting plate by first applying a thin layer of silicone glue on the back (lateral) and side (anterior-posterior) model surfaces. Insert model into recessed cut of mounting plate. Align the model medial surface with the top of the acrylic plate. Wipe away excess glue. Allow glue to cure for one hour.

1.17) Apply talc powder to the model surface to reduce surface tackiness.

1.18) For medial surface tracking use a fine-point Sharpie pen to mark dots on the model. Best results occur if marking is done after application of talc powder.

1.19) Place long bolts through holes of the mounting plate with the threaded ends pointing toward the model to which the existing model will be paired. Lay threads over the bolts. Put closed cell foam over the bolts to close any air gaps.

1.20) Pair this prepared model with another vocal fold model that has been similarly mounted to an acrylic holder using Steps 3.1 and 3.2. Tighten screws to compress the foam and bring the medial surfaces together until the desired pre-vibratory gap is reached. Ensure both sets of threads are placed over the bolts and extend outward from the acrylic plates in the anterior-posterior direction.

1.21) Mount vocal fold pair on air supply tube.

1.22) Tie the anterior threads together to form a loop. Repeat for the posterior threads.

Hang desired weight on the loops simultaneously.

1.23) Models are now ready for testing and data collection.

A.4) Representative Results

Vibratory response data from one model created using this fabrication process are as follows; these results are typical. With tension of approximately 31 g applied to the fibers, the onset pressure was 400 Pa. At a subglottal pressure of 10% above onset pressure (440 Pa), the model vibrated at 115 Hz with a glottal flow rate of 210 ml/s. These values are in good agreement with values reported for those of humans (Table A-3). Using high-speed videokymography to analyze model motion showed evidence of a phase difference between the superior and inferior margins, i.e., the superior margin concealed the inferior margin during the open phase of the vibration period (Figure A-3). Trajectories extracted from stereo images of the dots applied to the medial and inferior surfaces of the vocal fold model showed that the model exhibited an alternating convergent-divergent profile that is typical of human phonation, a mucosal wave-like motion, and a lower inferior-superior motion than in previous models (Figure A-4).

Table A-3: Comparison between human and synthetic vocal fold vibratory responses.

	Onset Pressure (kPa)	Frequency (Hz)	Flow Rate (ml/s)
Synthetic Model	0.40	115	210
Adult Human	0.29–0.49 ¹⁵	98–247 ¹⁶	70–200 ¹⁵

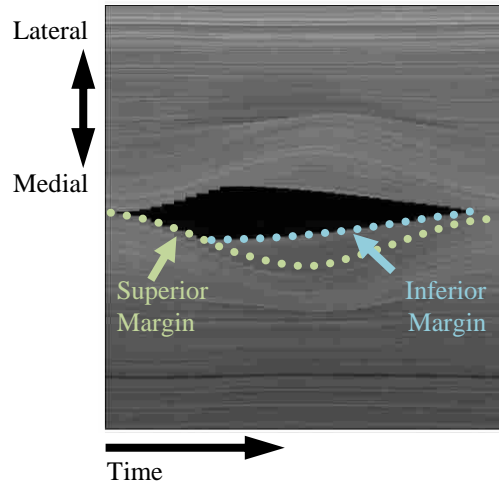


Figure A-3: High-speed kymogram of model vibration. Estimates for the location of the superior and inferior margins are shown in colored dotted lines. Phase differences between the inferior and superior margins are evident.

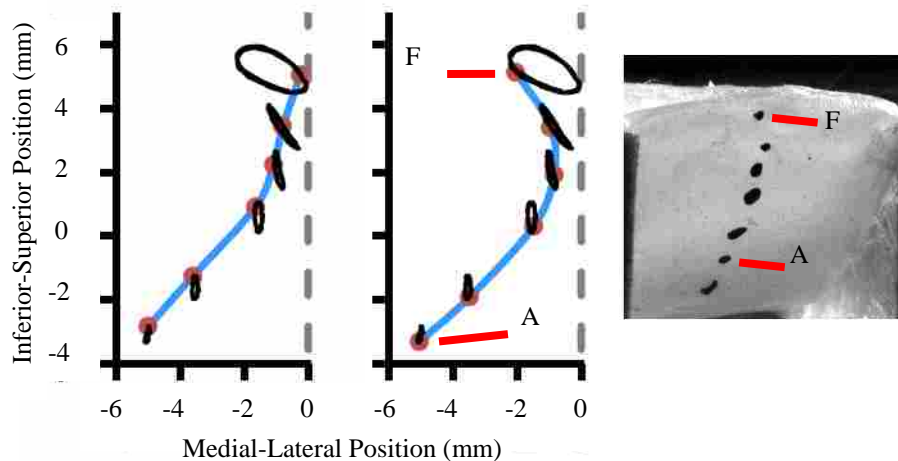


Figure A-4: Medial surface profile of synthetic vocal fold model in a hemilarynx arrangement, captured at two different instances of time while vibrating. Ink markers were placed on the medial surface (as shown in the right image), imaged using two synchronized high-speed cameras, and tracked over the vibratory cycle. The left plot shows a convergent glottis during the opening phase and the right plot shows a divergent glottis during the closing phase.

A.5) Discussion

This method of fabricating synthetic vocal fold models yields models that exhibit vibratory behavior similar to that of human vocal folds. The multi-layer concept results in significant advantages over previous one- and two-layer model designs^{3,6,8,15}, in terms of reduced onset and improved model motion (convergent-divergent profile during oscillation, mucosal wave-like motion, and reduced inferior superior displacement). The method presented here is demonstrated on a somewhat idealized model in terms of geometry, but it can be applied to models with different geometries. For example, a model based on human imaging geometric data (e.g., MRI¹⁷, CT) could be fabricated using this method. Additionally, this fabrication process concept may find application in other research areas in which flow-induced vibrations and/or multiple layers of soft materials are central elements, e.g., investigations of flow through blood vessels, sleep apnea, and animal locomotion (particularly swimming and flying).

The model described here has some limitations that could be subjects for future research and development. The materials have linear stress-strain response characteristics, and an anticipated future improvement includes the incorporation of nonlinear stress-strain materials. Use of biological rather than synthetic materials in this fabrication process is also possible. Because of the extreme flexibility of the lamina propria layer, the model is less robust under vibration than previous one- and two-layer models. However, keeping the subglottal pressure beneath approximately 1 kPa and occasionally applying talc powder to minimize surface adhesion should allow for the model to be used for durations on the order of days with minimal changes in model behavior, typically far exceeding those possible using excised larynges.

Table A-4: Specific reagents and equipment

Name of the reagent	Company	Catalogue number	Comments
High Vacuum Grease	Dow Corning	01018817	
Pol-Ease 2300	Polytek	Pol-Ease2300-1	Release agent
Smooth-Sil 950	Smooth-On	Smooth-Sil 950	Mold making material
Vacuum Pump	Edwards	E2M2	
Vacuum Chamber	Kartell	230	
Pressure Gage	Marsh Bellofram	11308252A	
Straight Razor	Husky	008-045-HKY	
Ecoflex 00-30	Smooth-On	Ecoflex 00-30	
Silicone Thinner	Smooth-On	Silicone Thinner	
Dragon Skin	Smooth-On	Dragon Skin 10 FAST	
Thread	Omega	OmegaCrys	Use only clear fibers
Silicone Dye	Smooth-On	Silc Pig Black	
Silicone Glue	Smooth-On	Sil-Poxy	
Talc Powder	Western Family		

A.6) References

- ¹ Hirano, M., & Kakita, Y. Cover-body theory of vocal fold vibration. In *Speech Science: Recent Advances* 1-46 (1985)
- ² National Institute on Deafness and Other Communication Disorders <http://www.nidcd.nih.gov/health/statistics/vsl.asp> (2010)
- ³ Pickup, B.A., & Thomson, S.L. Influence of asymmetric stiffness on the structural and aerodynamic response of synthetic vocal fold models. *Journal of Biomechanics* **42** (14), 2219-2225 (2009)
- ⁴ Zhang, Z. Vibration in a self-oscillating vocal fold model with left-right asymmetry in body-layer stiffness. *Journal of the Acoustical Society of America* **128** (5), EL279-EL285 (2010)
- ⁵ Popolo, P. S., & Titze, I. R. Qualification of a Quantitative Laryngeal Imaging System Using Videostroboscopy and Videokymography. *Annals of Otology, Rhinology & Laryngology* **117** (6), 4014-412 (2008)
- ⁶ Thomson, S.L., Mongeau, L., & Frankel, S.H. Aerodynamic transfer of energy to the vocal folds. *Journal of the Acoustical Society of America* **118** (3), 1689-1700 (2005)
- ⁷ Neubauer, J., Zhang, Z., Miraghaio, R., & Berry, D.A. Coherent structures of the near field flow in a self-oscillating physical model of the vocal folds. *Journal of the Acoustical Society of America* **121** (2), 1102-1118 (2007)

- ⁸ Drechsel, J.S., & Thomson, S.L. Influence of supraglottal structures on the glottal jet exiting a two-layer synthetic, self-oscillating vocal fold model. *Journal of the Acoustical Society of America* **123** (6), 4434-4445 (2008)
- ⁹ Becker, S., *et al.* Flow-structure-acoustic interaction in a human voice model. *Journal of the Acoustical Society of America* **125** (3), 1351-1361 (2009)
- ¹⁰ Spencer, M., Siegmund, T., & Mongeau, L. Experimental study of the self-oscillation of a model larynx by digital image correlation. *Journal of the Acoustical Society of America* **123** (2), 1089-1103 (2007)
- ¹¹ Zhang, Z., Neubauer, J., & Berry, D. The influence of subglottal acoustics on laboratory models of phonation. *Journal of the Acoustical Society of America* **120** (3), 1558-1569 (2006)
- ¹² Kniesburges, S., *et al.* In vitro experimental investigation of voice production. *Current Bioinformatics* (In Press)
- ¹³ Titze, I.R. *The Myoelastic Aerodynamic Theory of Phonation*. 82-101 (National Center for Voice and Speech, 2006)
- ¹⁴ Murray, P.R. *Flow-Induced Responses of Normal, Bowed, and Augmented Synthetic Vocal Fold Models*. Master's Thesis, Brigham Young University. (2011)
- ¹⁵ Baken, R.J., & Orlikoff, R.F. *Clinical Measurement of Speech and Voice*, 2nd edn. (Singular Publishing, 2000)
- ¹⁶ Titze, I.R. *Principles of Voice Production*, 2nd printing. (National Center for Voice and Speech, 2000)
- ¹⁷ Pickup, B.A., & Thomson, S.L. Flow-induced vibratory response of idealized vs. magnetic resonance imaging-based synthetic vocal fold models. *Journal of the Acoustical Society of America* **128** (3), EL124-EL129 (2010)

APPENDIX B. IMAGE CALIBRATION

For this thesis, points on the medial and inferior portion of the synthetic model (see Figure B-1) were tracked to extract trajectory information as well as the vertically propagating wave velocity and phase shift. This was done by placing a planar calibration plate in both stereo images and moving it away from the cameras in 1 mm increments by means of a linear stage actuated by a micrometer (Edmund Optics, NT37-980). In all cases the planar calibration plate was begun at the surface of the transparent acrylic plate as shown in Figure B-2.

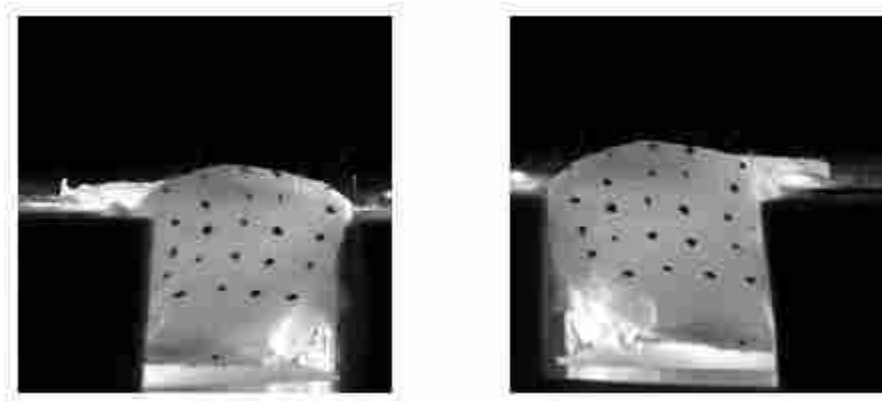


Figure B-1: Pair of typical stereo images of the medial and inferior surfaces of a synthetic vocal fold model.

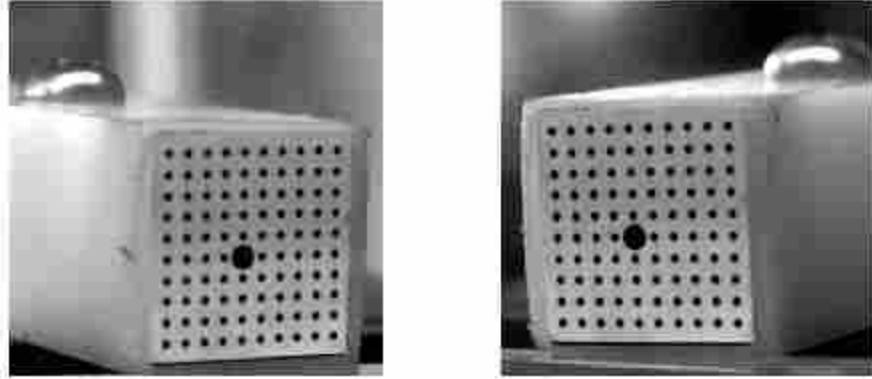


Figure B-2: Planar calibration plates placed at the surface of the clear acrylic plate for calibrating the images.

Since there was unnecessary information in the image affecting the thresholding process, the unneeded pixels were set to zero as shown in Figure B-3.

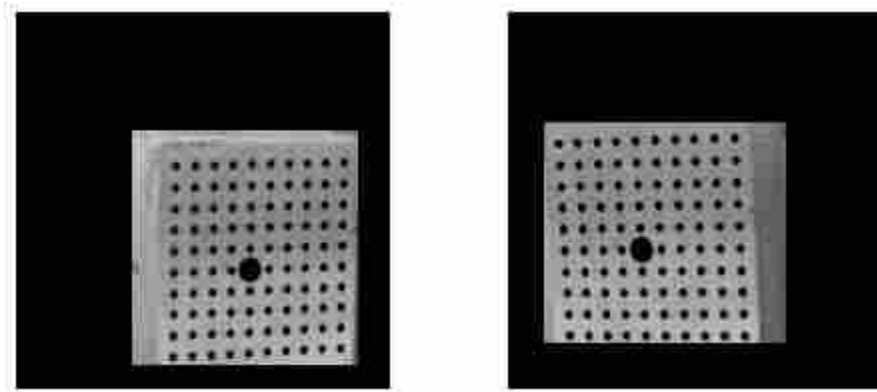


Figure B-3: Planar calibration plates with unnecessary pixels set to zero.

Now that the only image information was in the area of the calibration plates, the image was thresholded using ‘graythresh’, a function in MATLAB that finds a threshold value which minimizes the intraclass variance of the black and white pixels. The image was then converted to a binary image by setting all the pixels above the threshold value to one and below to zero. Since there was still noise in the image, a morphological filter was applied to remove any small areas of white pixels. The resulting binary image is shown in Figure B-4.

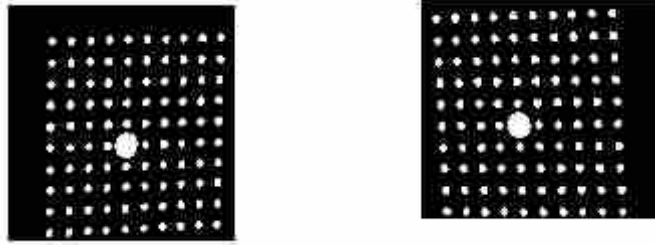


Figure B-4: Thresholded images after they were converted to binary.

Now that the dot locations were clearly visible, MATLAB was used to find the connected components (areas that were similar in shape) and determined the pixel location of their centroids. There were 100 dots in each image. Figure B-5 shows the results from this process. The blue circles were the centroids found from the above technique plotted on the original image.

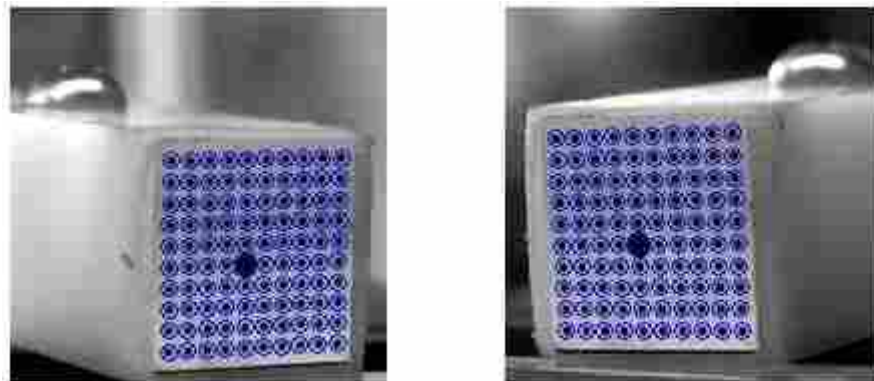


Figure B-5: Final image showing the found dot locations plotted over the original image.

With the pixel locations of each dot found in both images, the calibration plate was then moved back (laterally in the anatomical sense) and the dot finding process was repeated. Once all the desired points were found, they were used to create a calibration matrix which transfers pixel location to three dimensional space. For details on the DLT see George (2011).

APPENDIX C UNCERTAINTY ANALYSIS

C.1 Open Quotient

The open quotient (O_q) is defined as:

$$O_q = \frac{T_{Open}}{T} \quad (\text{C-1})$$

where T_{Open} is the amount of time the glottis is open during a specified period T . Taking the partial derivative with respect to both T_{Open} and T gives:

$$\frac{\partial O_q}{\partial T_{Open}} = \frac{1}{T} \quad (\text{C-2})$$

and

$$\frac{\partial O_q}{\partial T} = -\frac{T_{Open}}{T^2}. \quad (\text{C-3})$$

The uncertainty in O_q is then

$$\begin{aligned} u_{O_q} &= \sqrt{\left(\frac{\partial O_q}{\partial T_{Open}} \Delta T_{Open}\right)^2 + \left(\frac{\partial O_q}{\partial T} \Delta T\right)^2} \\ &= \sqrt{\left(\frac{1}{T} \Delta T_{Open}\right)^2 + \left(\frac{T_{Open}}{T^2} \Delta T\right)^2} \end{aligned} \quad (\text{C-4})$$

where ΔT_{Open} and ΔT are the error in the measurement of T_{Open} and T respectively. T was determined by evaluating the number of frames of the high speed images necessary to complete one vibratory cycle. The error was estimated as half of the sampling rate. Therefore,

$$\Delta T = \frac{1}{2 \cdot 3000} = \frac{1}{6000} . \quad (\text{C-5})$$

T_{Open} was determined by investigating a line of pixels at the middle of the synthetic vocal fold in the anterior-posterior direction of high speed images and summing the number of images the pixel line showed the glottis was open. The uncertainty in determining the moment the oscillating vocal folds opened or closed was estimated at 1 frame. Therefore,

$$\Delta T_{Open} = \frac{1}{3000} \quad (\text{C-6})$$

Using the smallest period reported of 25 frames, and the greatest number of frames the glottis was open of 30 frames and substituting these values into Equation 4 yields the total uncertainty in O_q as ± 0.047 .

C.2 Subglottal Pressure

The subglottal pressure was determined using a silicone differential pressure transducer vented to atmosphere. The uncertainty specified by the manufacturer was $\pm 0.1\%$ of full scale due to linearity and 0.5% of the max pressure from hysteresis. The full-scale of the pressure sensor

was 13.79 psi giving an uncertainty of 13.79 Pa. The max of the pressure sensor is 6.9 kPa which gives an uncertainty of 34.5 Pa. The total uncertainty of the pressure transducer was found by

$$u_P = \sqrt{u_{lin}^2 + u_{Hyst}^2} \quad (\text{C-7})$$

resulting in a total uncertainty of 37.13 Pa.

C.3 Onset Pressure

The onset pressure was found in all cases by increasing the subglottal pressure until vibration began 5 times. The mean and standard deviation were recorded. The uncertainty of these measurements was determined by taking into account the sample size and spread of the measurements. Since the sample size (n) was five, the degrees of freedom (ν) was $n-1$ giving a value for the t estimator of 2.770 with 95% confidence. The standard deviation of the means was defined as:

$$S_{\bar{x}} = \frac{S_x}{\sqrt{n}} \quad (\text{C-8})$$

With a sample size of five and the worst case standard deviation of 42 Pa, the standard deviation of the means was found to be 18.78 Pa. The uncertainty in these measurements with 95% confidence is found by

$$u_O = t_{\nu,95\%} S_{\bar{x}}. \quad (\text{C-9})$$

The resulting uncertainty is 52.03 Pa. Combining this value with the uncertainty from the pressure transducer found in the preceding section

$$u_{OP} = \sqrt{u_p^2 + u_o^2} \quad (\text{C-10})$$

gives a total uncertainty in the onset pressure of 63.92 Pa.

C.4 Glottal Flow Rate

The flow was measured with a rotometer type flow meter. The max flow was 1416 ml/s with a resolution of 47.2 ml/s. Since this is the smallest measured value that can be discerned, the uncertainty is half the resolution or 23.6 ml/s. The manufacturer specified an accuracy uncertainty of $\pm 3\%$ of the full-scale or 42.5 ml/s. Combining these two parameters using

$$u_{Flow} = \sqrt{u_{Resolution}^2 + u_{Accuracy}^2} \quad (\text{C-11})$$

gives a total uncertainty of 48.6 ml/s.

C.5 Acoustic Frequency

The frequency was found from the power spectral density function with a Hanning window in LabVIEW on a 5 second long signal sampled at 40 kHz. The resulting frequency discrimination was 0.2 Hz.

C.6 Glottal Area

The uncertainty of glottal gap was estimated from zero order (u_0), threshold (u_{th}), and calibration (u_c) uncertainties by

$$u_{area} = \sqrt{u_0^2 + u_{th}^2 + u_c^2}. \quad (\text{C-12})$$

Uncertainty from the resolution of the high-speed camera was calculated by taking half the smallest area the camera could measure by:

$$u_0 = \pm \left[\left(\frac{1 \text{ pixel}}{\text{pixels/mm}} \right)^2 \right] \quad (\text{C-13})$$

The smallest calibration from the camera was 35.25 pixels/mm giving a resolution uncertainty of 1.65×10^{-3} mm.

Threshold uncertainty was determined from changes in glottal gap based on the threshold value used to change the grayscale image to binary. The uncertainty is defined as

$$u_{th}^2 = \left(\frac{dG}{dT_h} c_{th} \right)^2, \quad (\text{C-14})$$

where G is the glottal area, T_h represents the threshold value (from 30 to 50 where numbers were based on an 8-bit grayscale image with a maximum and minimum of 255 and 0 respectively), and c_{T_h} is the difference of threshold values. The slope of change in area over change in threshold was calculated by measuring the change in area from change in threshold value. The resulting uncertainty (worst case) was found to be 0.041 mm.

Each high-speed image was calibrated by having the user click specified points on a ruler. The uncertainty due to differences in click location were determined using

$$u_c^2 = \left(\frac{dG}{dx} x_p \right)^2, \quad (\text{C-15})$$

where $\frac{dG}{dx}$ is the sensitivity of the glottal gap from mis-selected points selected by the user and x_p is the uncertainty in pixel location of the clicks. The slope $\left(\frac{dG}{dx} \right)$ was found by measuring the change in glottal gap by change in selected pixel location by 4 pixels either way in the x

direction. x_p was estimated as ± 4 pixels. The resulting uncertainty due to calibration was 0.0331 mm.

Using Equation (C-12) the resulting total uncertainty in calculated area was 0.0527 mm.

C.7 Trajectories

For tracking points in the hemilarynx setup during vibration, corresponding pixel locations of the applied dots were selected and converted to a three dimensional space through a direct linear transform. The inherent uncertainty in choosing the true pixel location was estimated at ± 3 pixels (the approximate radius of an average sized dot). In order to assess the effect of mis-selecting the correct dot location by three pixels, an uncertainty analysis was performed where the center of an applied dot was selected in corresponding images and the three dimensional coordinates were found. The left image pixel location was then moved three pixels up, down, left, and right and the three dimensional locations were evaluated against the original three dimensional location and maximum error was recorded. This evaluation process was repeated for six locations in the image: upper and lower right, middle, and left locations in the image pairs (see Figure C-1). The maximum average error in the x, y, and z directions are found in Table C-1.

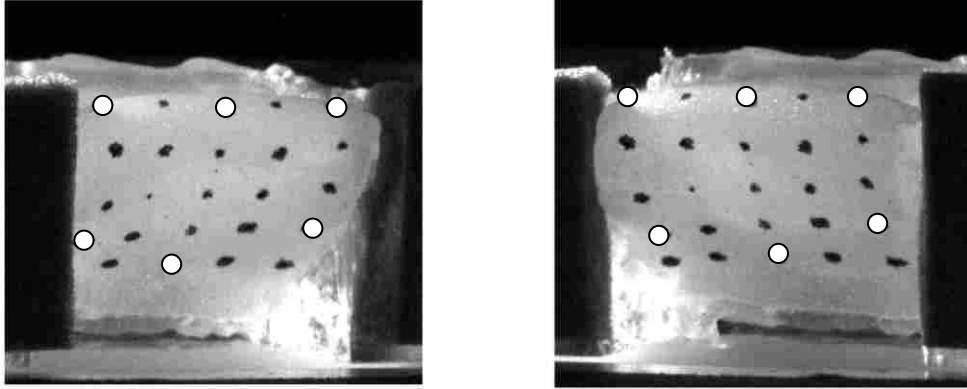


Figure C-1: Uncertainty analysis locations in the left and right hemilarynx images. The upper and lower left, middle, and right locations of the analysis are shown as white dots.

Table C-1: Maximum average error from mis-selecting pixels locations in hemilarynx images

Direction	Error (mm)
X	0.11
Y	0.10
Z	0.26

APPENDIX D. MATLAB

MATLAB was used to solve for factors including phase shift, frequency, glottal width, and frequency. Additionally, MATLAB was used to extract the medial surface trajectories of the hemilarynx setup. The following appendices provide the code used to compile this data.

D.1 Position Tracking of Points in 3D Space Over Time

```
% File to track position of point in 3D space over time. Uses
% correlation-based tracking algorithm combined with DLT.

% Altered by Preston Murray to incorporate multiple points

% opengl software
clc
close all
clear all

%% User Defined inputs
% Define window size (must be even number) for t and t+dt as well as the
% left to right correlation
MT = 32;
NT = 24;
MLR = 32;
NLR = 32;

% If manual points are desired, please enter how many points.
numpoints = 1;

% Enter the number of frames
frames = ceil(3000/125)*3;

%% Image load and Calibration
% Load image. Note that A is in spatial coordinates, with i=1,j=1 at the
% top left of the image. A(y,x) is the appropriate way to reference x,y
% position since A data is stored as A(row,column), where row = x and
% column = y data.
pathR = 'E:\ActualData2\NewTension130_C001H001S0001\';
pathL = 'E:\ActualData2\NewTension130_C002H001S0001\';

fileR = 'NewTension130_C001H001S0001000001.bmp';
fileL = 'NewTension130_C002H001S0001000001.bmp';

% Load the images
imageR = imadjust(imread([pathR fileR]));
imageL = imadjust(imread([pathL fileL]));

% % Use the following if L & R and calibration points have already been
% found & stored
% calframes = 5;
% [L,R,aveerror] = GridFinder(calframes, 'F:\ActualData2\');
% %
% close all
% save LR2.mat L R -double
load LR2.mat

% Choose point to track. Click on same point (approximately) in both left
% and right views. The FFT method will be used to fine-tune the right view
% point.
thing1 = 'Manual Mode';
```

```

thing2 = ['Please choose ', num2str(numpoints), ' sets of points'];
title(thing1);
xlabel(thing2);
imshow(imageL)
set(gcf, 'position', [0 150 560 420])
for i = 1:numpoints
    [uL0(i),vL0(i)]=ginput(1);
    hold on
    plot(uL0(i),vL0(i), 'g.')
end
hold off
% close(figure(1))
figure
imshow(imageR)
set(gcf, 'position', [460 150 560 420])
for i = 1:numpoints
    [uR0(i),vR0(i)]=ginput(1);
    hold on
    plot(uR0(i),vR0(i), 'g.')
end
hold off

%% Adjust the points from left to right
% Call function to interrogate window using FFT method. This is where the
% right view point will be fine-tuned (that is, the window in the right
% view that matches the window in the left view will be found).
for i=1:numpoints
    [xd,yd] = LRInterrogate(MLR,NLR,uL0(i),vL0(i),uR0(i),...
        vR0(i),imageL,imageR);
    xdtemp(i) = xd;
    ydtemp(i) = yd;
end

% Adjust points based on interrogation results
uL = uL0;
vL = vL0;
uR = uR0 + xdtemp;
vR = vR0 + ydtemp;

% Display adjusted point location
figure(1)
imshow(imageL)
set(gcf, 'position', [0 150 560 420])
hold on
plot(uL,vL, '.g')

figure(2)
imshow(imageR)
set(gcf, 'position', [460 150 560 420])
hold on
plot(uR,vR, '.r.')
% hold off

% Start storage of uL, vL, uR, vR point locations
UL = uL;
VL = vL;

```

```

UR = uR;
VR = vR;

%% Loop through images to track point(s) over time
for i = 1:frames-1
    % Load images at time=t and time=t+dt
    imageL1 = [pathL 'NewTension130_C002H001S0001' ...
        num2str(i, '%0.6i') '.bmp'];
    imageL2 = [pathL 'NewTension130_C002H001S0001' ...
        num2str(i+1, '%0.6i') '.bmp'];
    imageR1 = [pathR 'NewTension130_C001H001S0001' ...
        num2str(i, '%0.6i') '.bmp'];
    imageR2 = [pathR 'NewTension130_C001H001S0001' ...
        num2str(i+1, '%0.6i') '.bmp'];

    ALa = imadjust(imread(imageL1));
    ALb = imadjust(imread(imageL2));
    ARa = imadjust(imread(imageR1));
    ARb = imadjust(imread(imageR2));

    % Initialize point locations. Here, instead of comparing left & right
    % views, we're looking at the left view at time=t and comparing it to
    % the same left view at time=t+dt.
    uL0 = UL;
    vL0 = VL;
    uLdt = UL;
    vLdt = VL;

    % Track region in left view from time=t to time=t+dt
    for j = 1:numpoints
        [xd,yd] = TInterrogate(MT,NT,uL0(:,j,i),vL0(:,j,i),...
            uLdt(:,j,i),vLdt(:,j,i),ALa,ALb);
        xdltemp(:,j,i) = xd;
        ydltemp(:,j,i) = yd;
    end

    % Adjust points based on interrogation results
    uL(:, :, i) = uL0(:, :, i);
    vL(:, :, i) = vL0(:, :, i);
    uLdt(:, :, i) = uLdt(:, :, i) + xdltemp(:, :, i);
    vLdt(:, :, i) = vLdt(:, :, i) + ydltemp(:, :, i);

    % Compare right view point at time=t to time=t+dt.
    uR0(:, :, i) = UR(:, :, i);
    vR0(:, :, i) = VR(:, :, i);
    uRdt(:, :, i) = UR(:, :, i);
    vRdt(:, :, i) = VR(:, :, i);

    % Track region in right view from time=t to time=t+dt
    for j = 1:numpoints
        [xd,yd] = TInterrogate(MT,NT,uR0(:,j,i),vR0(:,j,i),...
            uRdt(:,j,i),vRdt(:,j,i),ARa,ARb);
        xdrtemp(:,j,i) = xd;
        ydrtemp(:,j,i) = yd;
    end
end

```

```

% Adjust points based on interrogation results
uR(:, :, i) = uR0(:, :, i);
vR(:, :, i) = vR0(:, :, i);
uRdt(:, :, i) = uRdt(:, :, i) + xdrtemp(:, :, i);
vRdt(:, :, i) = vRdt(:, :, i) + ydrtemp(:, :, i);

% Match point in right view at time=t+dt to point in left view at
% same time step.
for j = 1:numpoints
    [xd, yd] = LRInterrogate(MLR, NLR, uLdt(:, j, i), vLdt(:, j, i), ...
        uRdt(:, j, i), vRdt(:, j, i), ALb, ARb);
    xdtemp(j) = xd;
    ydtemp(j) = yd;
end

% Adjust points based on interrogation results
uLdt(:, :, i) = uLdt(:, :, i);
vLdt(:, :, i) = vLdt(:, :, i);
uRdt(:, :, i) = uRdt(:, :, i) + xdtemp;
vRdt(:, :, i) = vRdt(:, :, i) + ydtemp;

% Store point locations
UL(:, :, i+1) = uLdt(:, :, i);
VL(:, :, i+1) = vLdt(:, :, i);
UR(:, :, i+1) = uRdt(:, :, i);
VR(:, :, i+1) = vRdt(:, :, i);

% Display adjusted point location
figure(1)
imshow(ALb);
hold on
for j = 1:numpoints
    plot(UL(:, j, i), VL(:, j, i), 'g.', UL(:, j, i+1), VL(:, j, i+1), 'r.')
end
hold off
figure(2)
imshow(ARb)
for j = 1:numpoints
    plot(UR(:, j, i), VR(:, j, i), 'g.', UR(:, j, i+1), VR(:, j, i+1), 'r.')
end

% Create a movie from the plot frame
%     mov1(i) = getframe(1);
%     pause
end

%% Use DLT function to evaluate real-world position of selected points
for i = 1:frames
    for j = 1:numpoints
        X(j, :, i) = DLTApply(UL(:, j, i), VL(:, j, i), UR(:, j, i), VR(:, j, i), L, R);
    end
end

save X.mat -double

```

```

% load X.mat

%% Plots of points and surface
% Plot the trajectories of each point
for i = 1:numpoints
    plot(reshape(X(i,3,:),1,[]),reshape(X(i,2,:),1,[]))
    hold on
    plot([0 0], [-5 10], '--k')
    ylim([-5 10])
    axis equal
end
hold off
%%
% Timeline of surface through one period
len = length(uR0(1,1,:));
toverT = [1 round(.1*len) round(.2*len) round(.3*len) round(.4*len)...
    round(.5*len) round(.6*len) round(.7*len) round(.9*len)...
    round(.9*len) ];
i = 1;
q = 1;
figure('Position',[1 31 1280 920])
% pause
for j = toverT
    % plot the trajectories
    subplot(1,length(toverT),q)
    % set(gca,'position',[.01*(q-1)*9.4 0.9 .09 .09])
    plot(reshape(X(:,3,j),1,[]),reshape(X(:,2,j),1,[]),...
        '.k',...
        'LineWidth',2)
    i = i+1;
    hold on
    q = q+1;
    % plot the points on a line in time
    for p = 1:numpoints
        plot(reshape(X(p,3,:),1,[]),reshape(X(p,2,:),1,[]),'k')
    % ylabel(lab)
    xlim([-8 0])
    hold on
    plot([0 0],[-6 6], '--k',...
        'LineWidth',2)
    axis equal
    end
    if j > 5
        set(gca, 'YTick', []);
        set(get(gca, 'YLabel'), 'String', '')
    end
    % set(gca, 'XTick', [])
    set(gca, 'TickDir', 'in')
end

% %%
% x1 = reshape(X(1,3,:),1,[]);
% x2 = reshape(X(2,3,:),1,[]);
% x3 = reshape(X(3,3,:),1,[]);
% x4 = reshape(X(4,3,:),1,[]);

```

```

%% % x5 = reshape(X(5,3,:),1,[])';
%% % x6 = reshape(X(6,3,:),1,[])';
%%
%% y1 = reshape(X(1,2,:),1,[])';
%% % y2 = reshape(X(2,2,:),1,[])';
%% % y3 = reshape(X(3,2,:),1,[])';
%% % y4 = reshape(X(4,2,:),1,[])';
%% % y5 = reshape(X(5,2,:),1,[])';
%% % y6 = reshape(X(6,2,:),1,[])';
%%
%% Xout = [x1, y1];%, x2, y2, x3, y3, x4, y4, x5, y5];%, x6, y6];
%% xlswrite('Trajectories.xlsx',Xout, 'Convergent', 'A3')

```

```
function [L,R,aveerror] = GridFinder(frames, path)
```

```

for i = 1:frames
    %% Load and display the image
    %     folder1 = [num2str(i-1) ' _C1\'];
    %     folder2 = [num2str(i-1) ' _C2\'];
    imageL = [path num2str(i-1) ' _2_C002H001S0001000001.bmp'];
    imageR = [path num2str(i-1) ' _2_C001H001S0001000001.bmp'];

    imageR = imread(imageR);
    imageL = imread(imageL);

    % adjust the contrast of the images
    imageR = imadjust(imageR);
    imageL = imadjust(imageL);

    subplot(1,2,2)
    imshow(imageR)
    subplot(1,2,1)
    imshow(imageL)

    %% Theshold the image and convert to binary

    % Make parts of the right image go away
    imageR(1:end,1:50) = 0; % Crop from left to right side of grid
    imageR(1:150,1:end) = 0; % Crop from top to bottom
    imageR(1:end,380:end) = 0; % Crop from right side of grid to right
    imageR(450:512,1:end) = 0; % Crop from the bottom of grid to bottom of
image
    subplot(1,2,2)
    imshow(imageR)

    % Make parts of the left image go away
    imageL(1:160,1:end) = 0; % Crop from top to bottom
    imageL(1:end,1:160) = 0; % Crop from left to right side of grid
    imageL(1:end,470:end) = 0; % Crop from right side of grid to right
    imageL(480:512,1:end) = 0; % Crop from the bottom of grid to bottom of
image
    subplot(1,2,1)
    imshow(imageL)

    % Use graythresh to find the image threshold value

```

```

levelR = graythresh(imageR);
levelL = graythresh(imageL);

% Change the images to black and white
bwR = im2bw(imageR,levelR);
bwL = im2bw(imageL,levelL);

% Filter the image
bwR = bwareaopen(~bwR, 40);
bwL = bwareaopen(~bwL, 40);

% Show the processed image
figure
subplot(1,2,2)
imshow(bwR)
subplot(1,2,1)
imshow(bwL)

%% Call the CentroidFind mfile to find the centroids
[centroidR, zeropoint1] = CentroidFind(bwR);
[centroidL, zeropoint2] = CentroidFind(bwL);

% Sort the centroids
centroid = sortcentroid(centroidR, centroidL);

% Load the centroids and origins into their respective matrices (x,y,z)
for j = 1:numel(centroid(:,1))
    for k = 1:2
        centroidgrid(j,k,i) = centroid(j,k);
    end
end
%     origins(:,:,i) = zeropoint1(:);
%     origin2(:,:,i) = zeropoint2(:);
end

%% Calibrate the L and R Matrices
% Extract the pixel locations for the left and right images
[uR vR uL vL] = dotsort(centroidgrid);

% Load the real life coordinates of the points
load realmat.mat;

% Parse out the coordinates from each picture
x = realmat(1:500,1);
y = realmat(1:500,2);
z = realmat(1:500,3);

% Calculate the L and R matrices
[L,R] = DLTCalib(uL, vL, uR, vR, x, y, z);

%% Determine the error in the system at each point
% Use DLT function to evaluate real-world position of selected points
for i = 1:length(x)
    X(i,:) = DLTApply(uL(i),vL(i),uR(i),vR(i),L,R);
end

```

```

% Determine the error in the calibration system
for i = 1:length(x)
    error(i) = sqrt((x(i)-X(i,1))^2 + (y(i)-X(i,2))^2 + (z(i)-X(i,3))^2);
end
aveerror = mean(error);

%% Plot the results
% Plot the centroids
for j = 1:frames
    % Show image
    imageL = [path num2str(j-1) '_2_C002H001S0001000001.bmp'];
    imageR = [path num2str(j-1) '_2_C001H001S0001000001.bmp'];
    imageR = imread(imageR);
    imageL = imread(imageL);
    % adjust the contrast of the images
    imageR = imadjust(imageR);
    imageL = imadjust(imageL);

    figure(j)
    subplot(122)
    imshow(imageR);
    hold on

    % Plot the grid
    for k = 1 : 100
        plot(centroidgrid(k,1,j), centroidgrid(k,2,j), 'bo');
        % mov(k) = getframe;
        % pause
    end

    subplot(121)
    imshow(imageL);
    hold on
    % Plot the grid
    for k = 101 : numel(centroidgrid(:,1))
        plot(centroidgrid(k,1,j), centroidgrid(k,2,j), 'bo');
        % mov(k) = getframe;
        % pause
    end

end

end

end

function [centroid, zerocoor ] = CentroidFind(bw)
% This function finds the centroid of points in a pre processed image
% bw is a pre processed image
% The output 'centroid' is the centroids of the points from the image
% The output 'zerocoor' is the location of the zero point on the image

% Identify the connected components in the binary image
cc = bwconncomp(bw,8);
cc.NumObjects;

```

```

% Find the
pointdata = regionprops(cc, 'basic');

% Find the centroid and weighted centroid of the points
% s = regionprops(bw, I, {'Centroid','WeightedCentroid'});

% Find the surrounding area and remove it
point_areas = [pointdata.Area];
[~, idx] = max(point_areas);
pointdata = pointdata(idx+1:end);

% Find the location of the center point (big point)
point_areas = [pointdata.Area];
[idx] = find(point_areas > 200);
coor1 = pointdata(idx(1)).Centroid;
% coor2 = pointdata(idx(2)).Centroid;
uL = coor1(1);
vL = coor1(2);
% uR = coor2(1);
% vR = coor2(2);

zerocoor = [uL, vL];%, uR, vR];
% Plot the centroid and weighted centroid from the processed and original
% figure(5)
% imshow(bw)
% title('Weighted (red) and Unweighted (blue) Centroid Locations');
% hold on
% % numObj = numel(s);
% % for k = 1 : numObj
% %     plot(s(k).WeightedCentroid(1), s(k).WeightedCentroid(2), 'r*');
% %     plot(s(k).Centroid(1), s(k).Centroid(2), 'bo');
% % end
% % hold off
% %
% Plot the centroid calculated only from the processed image
figure(6)
imshow(bw)
hold on
numObj2 = numel(pointdata);
for k = 1 : numObj2
    plot(pointdata(k).Centroid(1), pointdata(k).Centroid(2), 'bo');
end
plot(uL, vL, 'gd') %, uR, vR, 'gd')
hold off

for i = 1:numel(pointdata)
    centroid(i,:) = [pointdata(i).Centroid];
end
lcentroid = centroid(1:100);
% Rcentroid = centroid(101:200);

end

function [centroid] = sortcentroid(centroid1, centroid2)
%SORTCENTROID receives the matrix centroid, parses the data into a matrix

```

```

%of single columns, sorts them according to the y coordinate (column 2),

centroid = [sortrows(centroid1(1:10,:),2);...
            sortrows(centroid1(11:20, :),2);...
            sortrows(centroid1(21:30, :),2);...
            sortrows(centroid1(31:40, :),2);...
            sortrows(centroid1(41:50, :),2);...
            sortrows(centroid1(51:60, :),2);...
            sortrows(centroid1(61:70, :),2);...
            sortrows(centroid1(71:80, :),2);...
            sortrows(centroid1(81:90, :),2);...
            sortrows(centroid1(91:100, :),2);...

            sortrows(centroid2(1:10,:),2);...
            sortrows(centroid2(11:20, :),2);...
            sortrows(centroid2(21:30, :),2);...
            sortrows(centroid2(31:40, :),2);...
            sortrows(centroid2(41:50, :),2);...
            sortrows(centroid2(51:60, :),2);...
            sortrows(centroid2(61:70, :),2);...
            sortrows(centroid2(71:80, :),2);...
            sortrows(centroid2(81:90, :),2);...
            sortrows(centroid2(91:100, :),2)];

end

function [ uL vL uR vR ] = dotsort(centroidgrid)
%dotsort

% Extract the left and right coordinates from the centroid matrix
xL = centroidgrid(1:100,1,:);
xR = centroidgrid(101:200,1,:);
yL = centroidgrid(1:100,2,:);
yR = centroidgrid(101:200,2,:);

% Place the above data into 2-D matrices
uL = [xL(:, :, 1); xL(:, :, 2); xL(:, :, 3); xL(:, :, 4); xL(:, :, 5)]; % xL(:, :, 6); ];
vL = [yL(:, :, 1); yL(:, :, 2); yL(:, :, 3); yL(:, :, 4); yL(:, :, 5)]; % yL(:, :, 6); ];
uR = [xR(:, :, 1); xR(:, :, 2); xR(:, :, 3); xR(:, :, 4); xR(:, :, 5)]; % xR(:, :, 6); ];
vR = [yR(:, :, 1); yR(:, :, 2); yR(:, :, 3); yR(:, :, 4); yR(:, :, 5)]; % yR(:, :, 6); ];

end

function [L,R] = DLTCalib(uL,vL,uR,vR,x,y,z)

% Construct A matrix for left and right views, u component
N=length(x);
for i=1:2:N*2
    k=(i+1)/2;
    AL(i,:)=[x(k) y(k) z(k) 1 0 0 0 0 -uL(k)*x(k) -uL(k)*y(k) -uL(k)*z(k)];
    AR(i,:)=[x(k) y(k) z(k) 1 0 0 0 0 -uR(k)*x(k) -uR(k)*y(k) -uR(k)*z(k)];
    BL(i,1)=[uL(k)];
    BR(i,1)=[uR(k)];
end

% Construct A matrix for left and right views, v component
for i=2:2:N*2

```

```

    k=i/2;
    AL(i,:)= [0 0 0 0 x(k) y(k) z(k) 1 -vL(k)*x(k) -vL(k)*y(k) -vL(k)*z(k)];
    AR(i,:)= [0 0 0 0 x(k) y(k) z(k) 1 -vR(k)*x(k) -vR(k)*y(k) -vR(k)*z(k)];
    BL(i,1)= [vL(k)];
    BR(i,1)= [vR(k)];
end

% Calculate L and R calibration matrices
L=(inv(AL'*AL))*(AL'*BL);
R=(inv(AR'*AR))*(AR'*BR);

end

function [X] = DLTApply(uL,vL,uR,vR,L,R)

% Calculate A matrix
A = [L(1)-L(9)*uL L(2)-L(10)*uL L(3)-L(11)*uL;...
     L(5)-L(9)*vL L(6)-L(10)*vL L(7)-L(11)*vL;...
     R(1)-R(9)*uR R(2)-R(10)*uR R(3)-R(11)*uR;...
     R(5)-R(9)*vR R(6)-R(10)*vR R(7)-R(11)*vR];

% Calculate B matrix
B = [uL-L(4); vL-L(8); uR-R(4); vR-R(8)];

% Calculate X = [x,y,z] positions
X = inv(A'*A)*A'*B;

end

function [xd,yd] = LRInterrogate(M,N,uA,vA,uB,vB,imageL,imageR)

uA = round(uA);
vA = round(vA);
uB = round(uB);
vB = round(vB);

% Define left & right windows (subsets of original image)
Aa = imageL(vA-(N/2-1):vA+N/2, uA-(M/2-1):uA+M/2);
Ab = imageR(vB-(N/2-1):vB+N/2, uB-(M/2-1):uB+M/2);

% Calculate FFT2 of left image window, centered about uL0,vL0
% Recall that image indices are in row,column format, which is y,x
FFTa = fft2(Aa);
% Calculate FFT2 of right image window, centered about uR0,vR0
FFTb = fft2(Ab);

% Use FFT method to compare left & right images
phi = fftshift(iff2(FFTa.*conj(FFTb)));

% Find peak of correlation. This tells us how much the right window needs
% to be adjusted (fine-tuned) based on our original pick.
[npeakint,mpeakint] = find(max(max(phi))==phi);
npeakint = npeakint(1);
mpeakint = mpeakint(1);

```

```

% This part is not used, not sure why
xdint = -(mpeakint - (M/2 + 1));
ydint = -(npeakint - (N/2 + 1));

% Conditional statements to move the point away from the
% edges of the interrogation window
if npeakint < 2
    npeakint = 2;
elseif npeakint > N-2
    npeakint = N-2;
end
if mpeakint < 2
    mpeakint = 2;
elseif mpeakint > M-2
    mpeakint = M-2;
end

% Calculate sub-pixel displacement
mstar = (log(phi(npeakint,mpeakint+1)) - log(phi(npeakint,mpeakint-1)))/...
    (4*log(phi(npeakint,mpeakint)) - 2*log(phi(npeakint,mpeakint-1)) ...
    - 2*log(phi(npeakint,mpeakint+1)));
nstar = (log(phi(npeakint+1,mpeakint)) - log(phi(npeakint-1,mpeakint)))/...
    (4*log(phi(npeakint,mpeakint)) - 2*log(phi(npeakint-1,mpeakint)) ...
    - 2*log(phi(npeakint+1,mpeakint)));
mpeak = mpeakint + mstar;
npeak = npeakint + nstar;

xd = -(mpeak - (M/2 + 1));
yd = -(npeak - (N/2 + 1));

% % Display correlation surface and peak location
% % Display windows
% figure(4)
% set(gcf,'position',[700 35 560 420])
% subplot(221)
% imshow(uint8(Aa))
% xlabel('Left')
% subplot(222)
% subplot(2,2,2)
% imshow(uint8(Ab))
% xlabel('Right')
%
% subplot(223)
% subplot(2,2,3)
% mesh(phi)
% xlabel('m')
% ylabel('n')
% shading interp
% hold on
% plot3(mpeakint,npeakint,max(max(phi)),'g.')
% plot3(mpeak,npeak,max(max(phi)),'r.')
%
% hold off
% subplot(224)

```

```

% subplot(2,2,4)
% axis square
% pcolor(phi)
% xlabel('m')
% ylabel('n')
% shading interp
% hold on
% plot(mpeakint,npeakint,'g.',mpeak,npeak,'r.')
% hold off
% % pause

end

function [xd,yd] = TInterrogate(M,N,uA,vA,uB,vB,A1,A2)

uA = round(uA);
vA = round(vA);
uB = round(uB);
vB = round(vB);

% Define left & right windows (subsets of original image)
Aa = A1(vA-(N/2-1):vA+N/2, uA-(M/2-1):uA+M/2);
Ab = A2(vB-(N/2-1):vB+N/2, uB-(M/2-1):uB+M/2);

% % Display windows
% figure(2)
% subplot(121)
% imshow(uint8(Aa))
% subplot(122)
% imshow(uint8(Ab))

% Calculate FFT2 of left image window, centered about uL0,vL0
% Recall that image indices are in row,column format, which is y,x
FFTa = fft2(Aa);
% Calculate FFT2 of right image window, centered about uR0,vR0
FFTb = fft2(Ab);

% Use FFT method to compare left & right images
phi = fftshift(iff2(FFTa.*conj(FFTb)));

% Find peak of correlation. This tells us how much the right window needs
% to be adjusted (fine-tuned) based on our original pick.
[npeakint,mpeakint] = find(max(max(phi))==phi);
mpeakint = mpeakint(1);
npeakint = npeakint(1);

% These two values are not used in the program
xdint = -(mpeakint - (M/2 + 1));
ydint = -(npeakint - (N/2 + 1));

% Calculate sub-pixel displacement
mstar = (log(phi(npeakint,mpeakint+1)) - log(phi(npeakint,mpeakint-1)))/...
        (4*log(phi(npeakint,mpeakint)) - 2*log(phi(npeakint,mpeakint-1)) ...
        - 2*log(phi(npeakint,mpeakint+1)));
nstar = (log(phi(npeakint+1,mpeakint)) - log(phi(npeakint-1,mpeakint)))/...

```

```

        (4*log(phi(npeakint,mpeakint)) - 2*log(phi(npeakint-1,mpeakint)) ...
        - 2*log(phi(npeakint+1,mpeakint)));
mpeak = mpeakint + mstar;
npeak = npeakint + nstar;
xd = -(mpeak - (M/2 + 1));
yd = -(npeak - (N/2 + 1));

% % Display correlation surface and peak location
% figure(3)
% set(gcf,'position',[100 35 560 420])
% subplot(221)
% imshow(Aa)
% xlabel('i')
%
% subplot(222)
% imshow(Ab)
% xlabel('i+1')
%
%
% subplot(223)
% mesh(phi)
% xlabel('m')
% ylabel('n')
% shading interp
% hold on
% plot3(mpeakint,npeakint,max(max(phi)),'g.')
% plot3(mpeak,npeak,max(max(phi)),'r.')
% hold off
% subplot(224)
% pcolor(phi)
% xlabel('m')
% ylabel('n')
% shading interp
% hold on
% plot(mpeakint,npeakint,'g.',mpeak,npeak,'r.')
% hold off
% pause
end

```

D.2 Code to Extract Maximum Glottal Width

```
% Program to read high-speed images and calculate glottal area vs. time and
% position of left & right vocal fold models
% Altered by Preston Murray June 2011

clear all
clf
%%
A
imread('F:\ActualData3\MRI130_C001H001S0001\MRI130_C001H001S0001000001.bmp');
imshow(A)
hold on
for i = 1:2
    [x(i),y(i)] = ginput(1);
    plot(x(i),y(i),'.r')
end
dist = sqrt((x(1)-x(2))^2+(y(1)-y(2))^2);
ppmm = dist/10;
% ppmm= 47.58; % Pixels per mm
fps= 3000;
NImages= 40; %Number of images kymographed
MinTime = 0/fps;
MaxTime = (NImages-1)/fps;
Time=0:1/fps:MaxTime;
NonDimTime=0:1/NImages:(NImages-1)/NImages;

for i=1:NImages
    % Read in file
    FileDir=['F:\ActualData3\MRI130_C001H001S0001\'];
    ImageName=[FileDir 'MRI130_C001H001S0001' num2str(i,'% .6d') '.bmp'];
    A=imread(ImageName);

    % Convert image to type double
    C=double(A);

    % Select top & bottom of orifice
    if i==1
        figure(1)
        subplot(111)
        image(C/3); axis xy; colormap(gray)
        title(['Select top of orifice'])
        [xtop,ytop]=ginput(1);
        xtop=round(xtop);
        ytop=round(ytop);
        title(['Select bottom of orifice'])
        [xbottom,ybottom]=ginput(1);
        xbottom=round(xbottom);
        ybottom=round(ybottom);
    end

    % Display original image with top as well as bottom orifice lines
    subplot(311)
    set(gca,'FontSize',10,'FontName','Times');
    image(C/3); axis xy
```

```

shading interp
colormap gray
hold on
plot([0 size(C,2)], [ytop ytop], [0 size(C,2)], [ybottom ybottom])
plot([xtop, xbottom], [ytop, ybottom], 'r--');
hold off

% Plot intensity vs. horizontal location along row y=500
subplot(312)
set(gca, 'FontSize', 10, 'FontName', 'Times');
y=500;
plot(C(y, :))
xlim([0 1024]); ylim([0 255])

% Crop C by removing top & bottom
C(ytop:size(C,1), :)=[];
C(1:ybottom, :)=[];

% Identify all pixels with intensity > Thresh by coloring them green
Thresh=30;
D=im2bw(C/255, Thresh/255); % Convert grayscale image to binary image
E(:, :, 1)=C/255; % Red channel
E(:, :, 2)=1-D; % Green channel
E(:, :, 3)=C/255; % Blue channel

% Find distance to left edge at midpoint
% Find left & right model displacements from centerline at midpoint
% between top & bottom
yMid=round(size(C,1)/2);
xMid=round(0.5*(xbottom+xtop));
if D(yMid, xMid)==0
    Edge1=1; % xMid, yMid coordinate is in glottis
elseif D(yMid, xMid)==1
    Edge1=0; % Either closed or Right VF is to left of midplane
end

Edge1=0;
Edge2=0;
for j=1:size(D,2)
    if Edge1==0
        if D(yMid, j)==0
            LeftEdge(i)=j;
            Edge1=1;
        end
    end
    if Edge1==1
        if D(yMid, j)==1
            RightEdge(i)=j;
            Edge2=1;
            Edge1=0;
        end
    end
end
if Edge2==0
    LeftEdge(i)=nan;
    RightEdge(i)=nan;
end

```

```

end

% Plot orifice, midline, and lines to left & right vocal folds
subplot(313)
set(gca, 'FontSize', 10, 'FontName', 'Times');
image(E); axis xy; % All pixels with intensity > Thresh are now green
hold on
plot([xtop, xbottom], [ytop, ybottom], 'r--');
%     plot([xMid, LeftEdge(i)], [yMid, yMid], 'r:');
plot([LeftEdge(i), RightEdge(i)], [yMid, yMid], 'b:');
hold off

% Calculate orifice area in pixels
% Note: 1 = outside orifice, 0 = inside orifice
DArea(i) = size(D, 1) * size(D, 2) - bwarea(D);

% Command to update images
drawnow

end
% Convert area from pixel to mm^2
DArea = DArea / ppmm^2;
% Convert edge locations to mm relative to midplane
LeftEdge = (LeftEdge - xMid) / ppmm;
RightEdge = (RightEdge - xMid) / ppmm;

% Plot area & edge position vs. t/T
figure(2)
subplot(211)
set(gca, 'FontSize', 10, 'FontName', 'Times');
plot(NonDimTime, DArea)
xlabel('Nondimensional time (t/T)')
ylabel('Glottal area (mm^2)')
% Convert edge locations to mm
subplot(212)
set(gca, 'FontSize', 10, 'FontName', 'Times');
plot(NonDimTime, LeftEdge, NonDimTime, RightEdge);
xlabel('Nondimensional time (t/T)')
ylabel('Edge position (mm)')
legend('LeftEdge', 'RightEdge')

% Format for plotting
figure(1)
set(gcf, 'PaperPosition', [1 1 3 3])
hold(gca, 'all');
print('-dtiff', '-r200', 'figure1.tif');
figure(2)
set(gca, 'FontSize', 10, 'FontName', 'Times');
subplot(211)
set(gcf, 'PaperPosition', [1 1 3 3])
hold(gca, 'all');
print('-dtiff', '-r200', 'figure2.tif');

MaxGlottalWidth = max(RightEdge) - min(LeftEdge);

```

APPENDIX E. DRAWINGS

The pertinent detailed drawings for the hardware used in this thesis are found in this appendix, including drawings for the hemilarynx setup used to image the medial and inferior surfaces of the vocal fold models as well as the setup that enabled the injection of material into the bowed models.

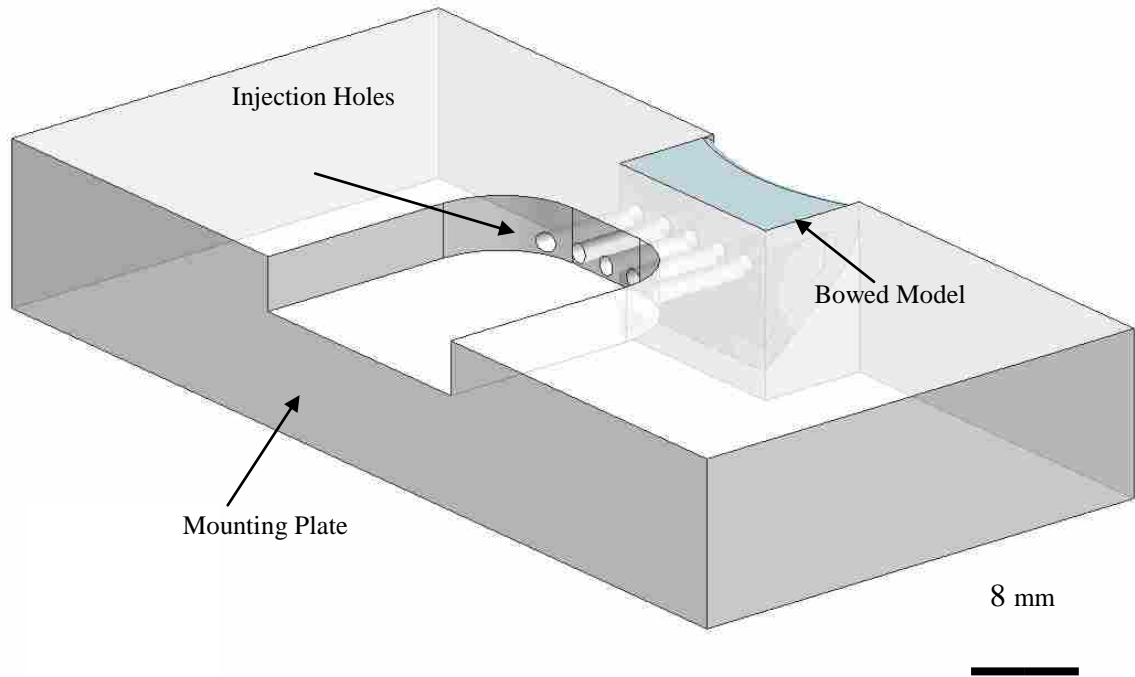


Figure E-1: Isometric view of acrylic plate with injection holes

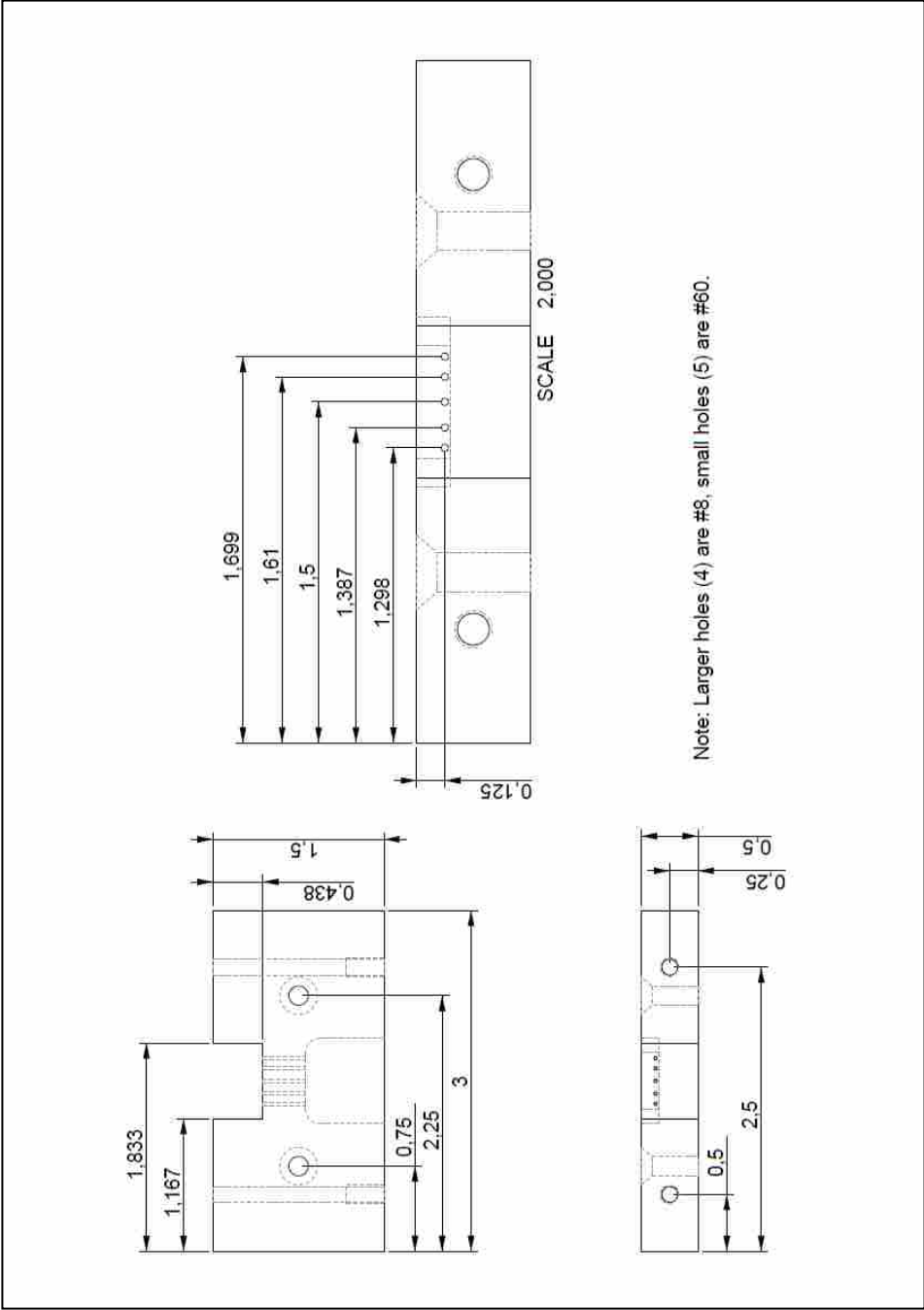


Figure E-2: Acrylic vocal fold model holder with holes for injecting bowed model

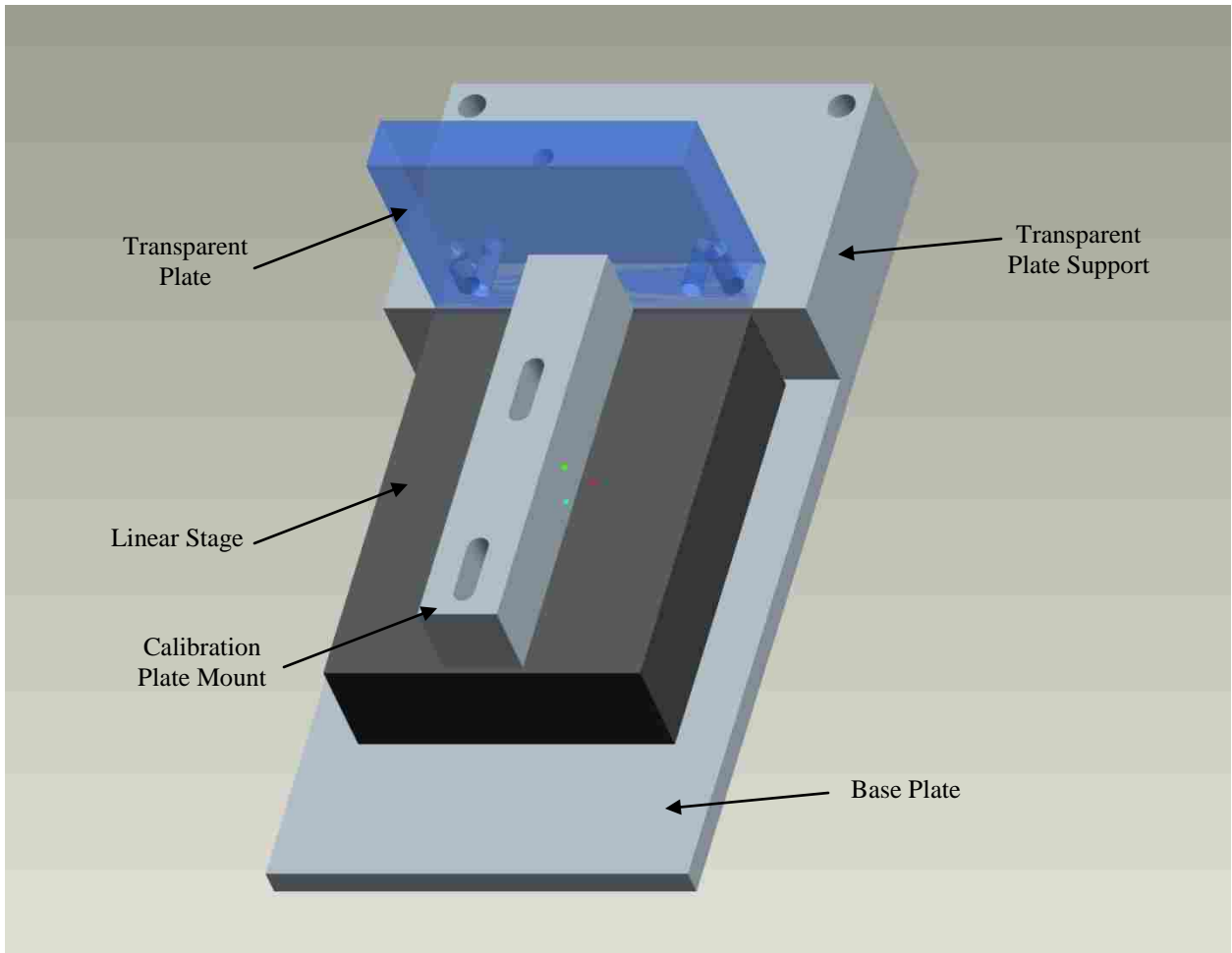


Figure E-3: Hemilarynx assembly during the calibration process

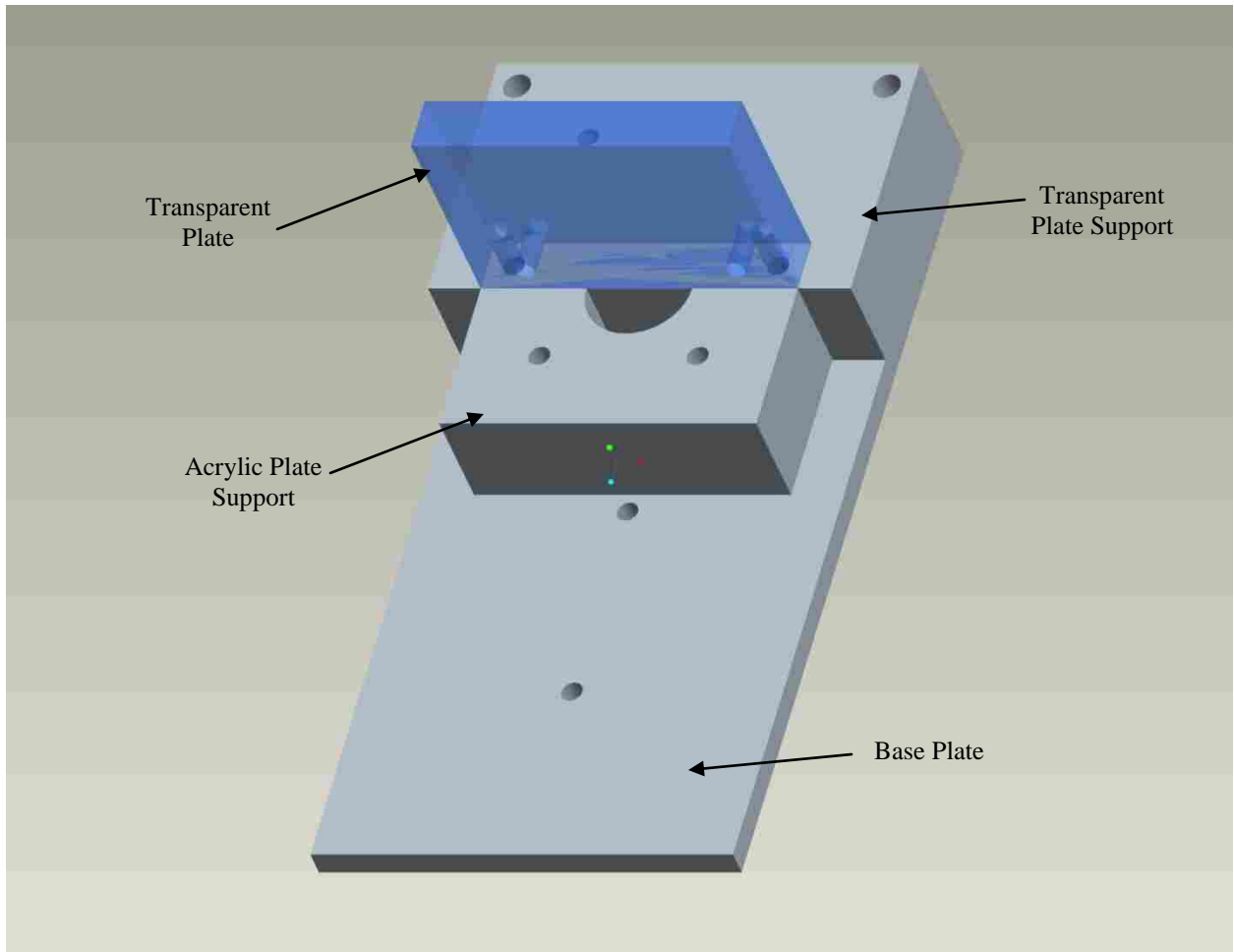


Figure E-4: Hemilarynx setup for mounting of vocal fold model acrylic holder

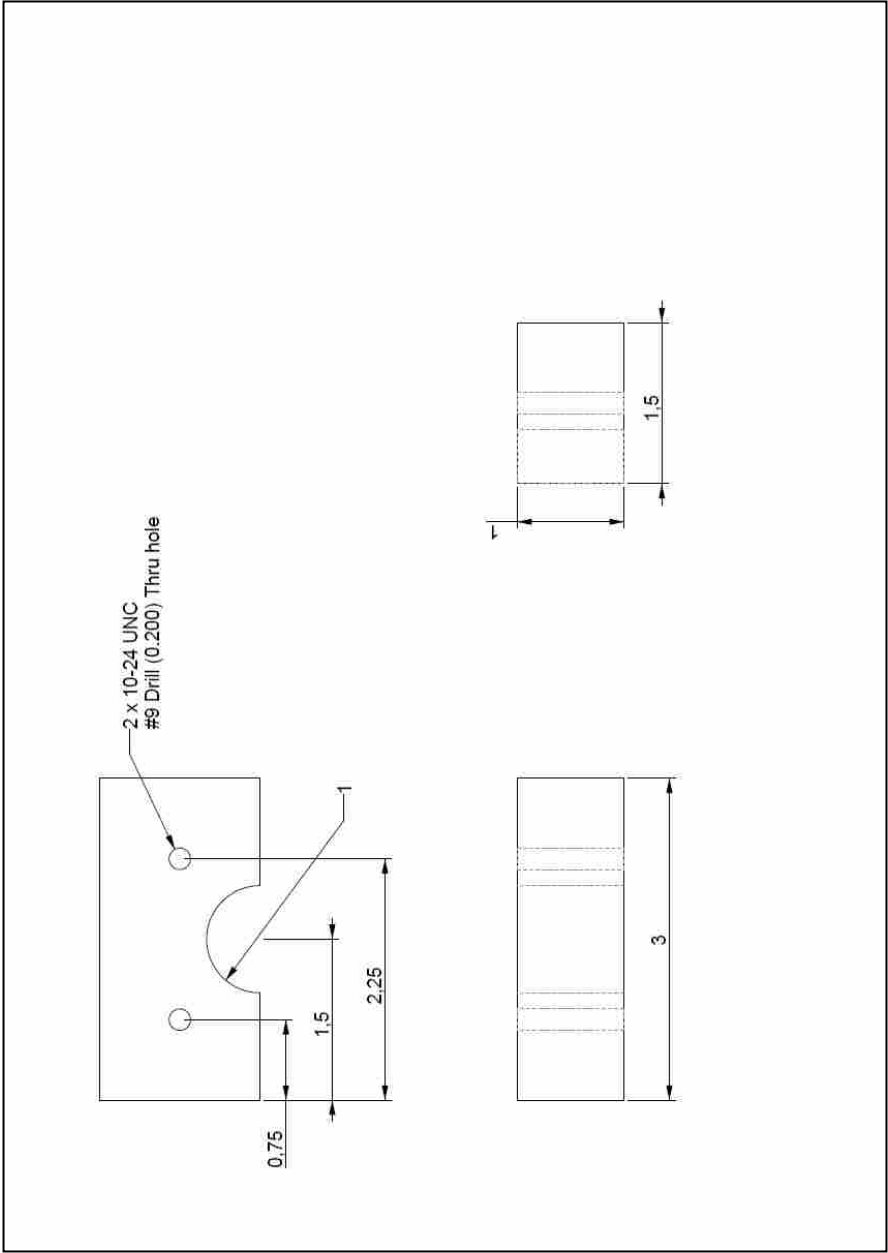


Figure E-5: Acrylic vocal fold support

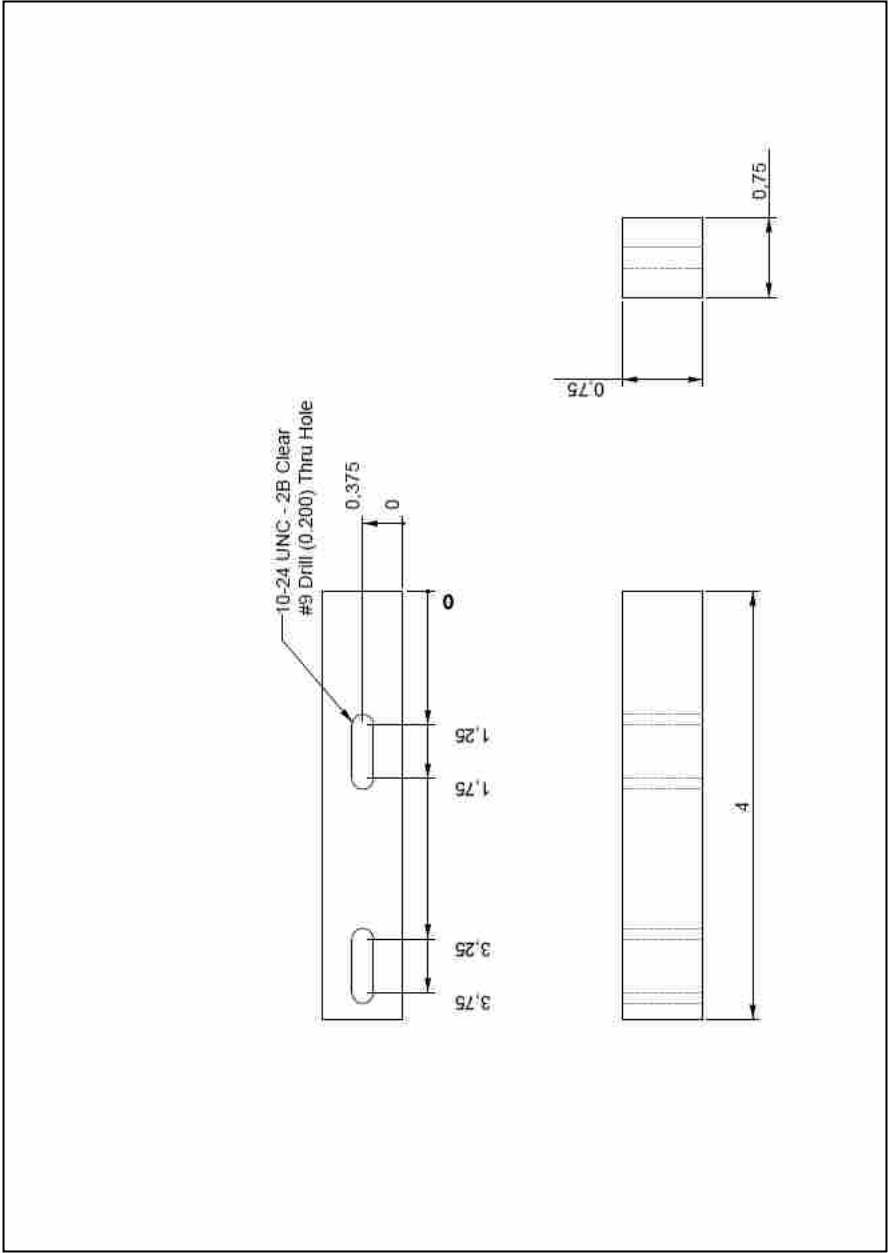


Figure E-6: Calibration plate mount.

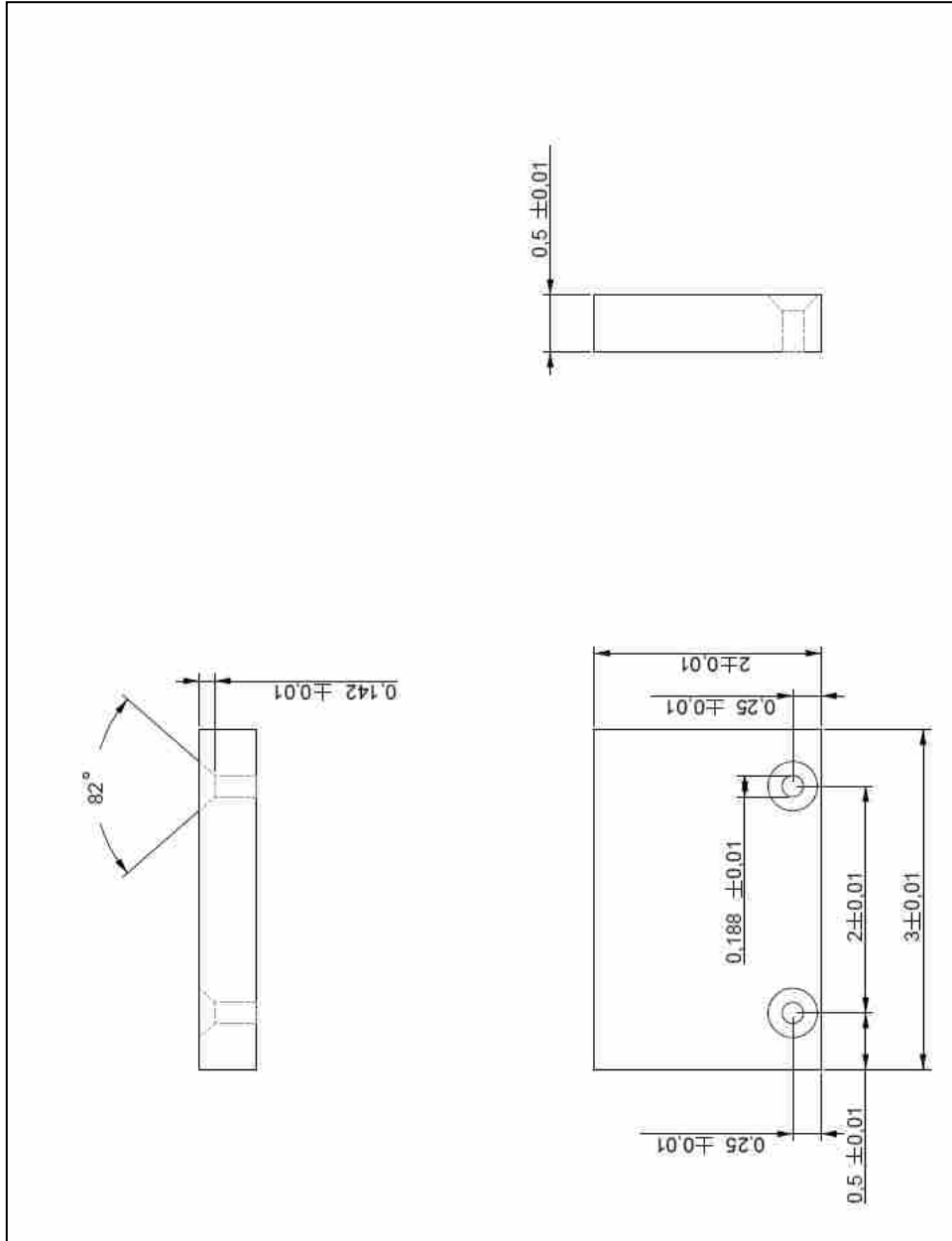


Figure E-7: Transparent plate

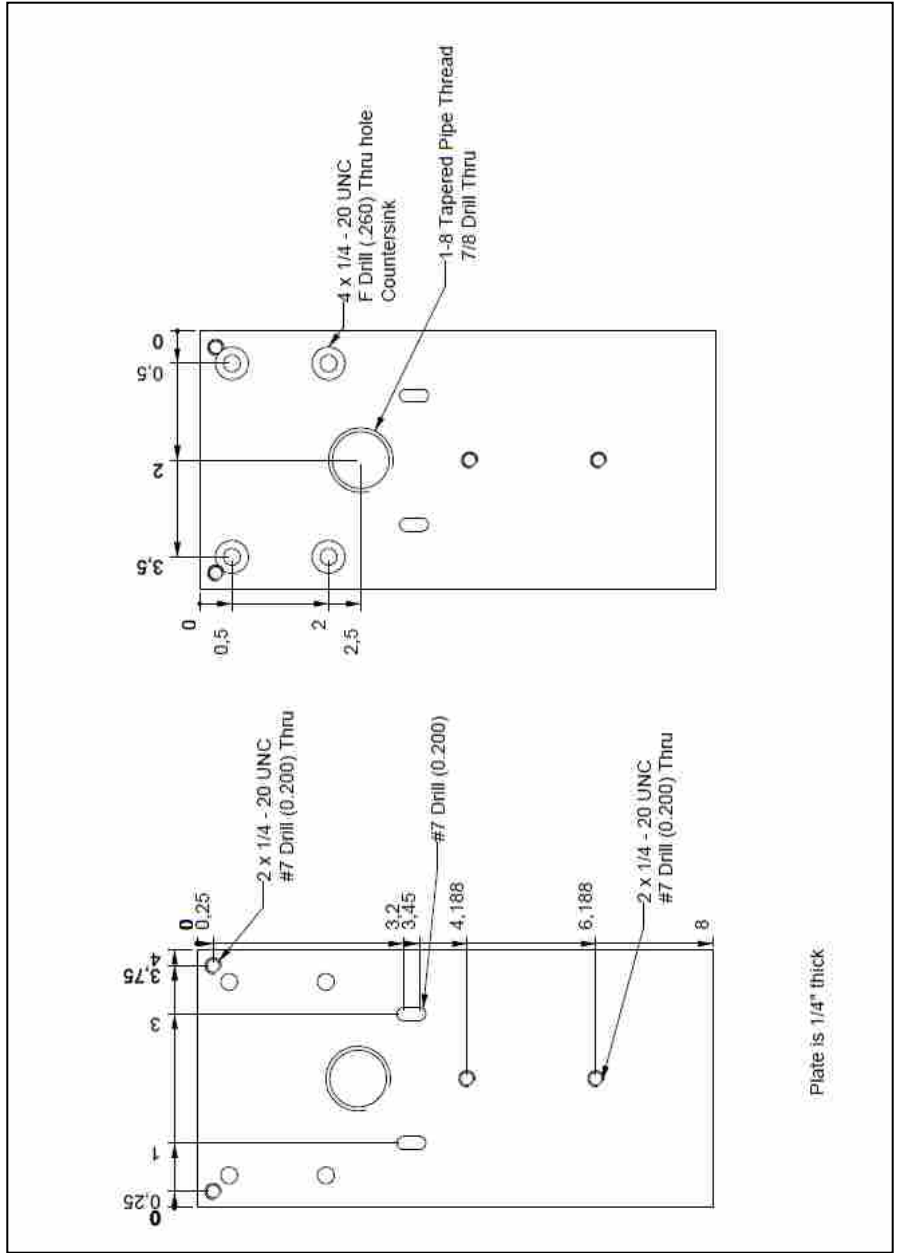


Figure E-8: Base plate for hemilarynx setup

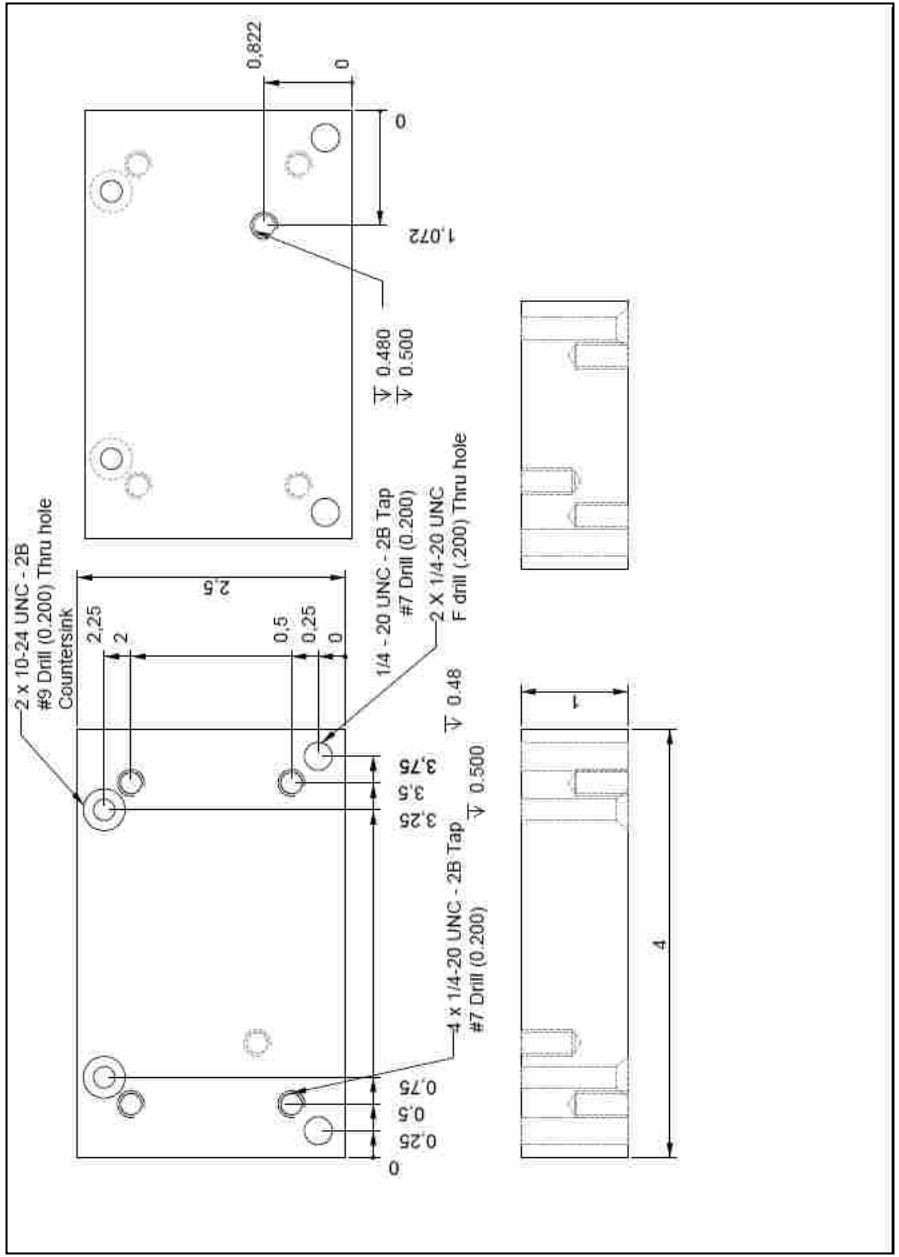


Figure E-9: Transparent plate support